

Breaking Fundamental Limits of Electrically Small Antennas

Maximilian D. S Williams

**A thesis submitted for the degree of
Bachelor of Philosophy in Science with Honours in Physics at
The Australian National University**

November 2022

Declaration

This thesis is an account of research undertaken between February 2022 and October 2022 at the Research School of Physics, The Australian National University, Canberra, Australia. Except where acknowledged in the customary manner, the material presented in this thesis is, to the best of my knowledge, original and has not been submitted in whole or part for a degree at any other university.

Maximilian D.S Williams

November 2022

Acknowledgements

First, I would like to thank Professor Ilya Shadrivov for his invaluable supervision and time throughout this Honours project - which had many twists and turns, reformulations, roadblocks and required many meetings that went a little longer than expected. I would also like to thank Fedor Kovalev for the discussions on the intersection between our research, his library of obscure books on parametric processes and showing me the secret Ethiopian restaurant just off campus. Finally, I would like to thank my peers in the Honours cohort, for making the year fun - although they have reinstated a crippling Uber Eats addiction of mine.

Abstract

The ability to transmit large amounts of information over large distances is critical to modern wireless communication and sensing. Through miniaturisation of technologies such as batteries and semiconductors, the need for high performance antennas of size smaller than the wavelength of radiation which they transmit/receive has arisen. However, since the 1940s, it has been known that these Electrically Small Antennas (ESAs) cannot simultaneously have large range and information rate. Such bounds are founded on the condition that the antenna is linear, time-invariant and passive (no additional energy is added to the system). In this thesis, I study and generalise these bounds on the simultaneous range and information rate of ESAs. By developing and implementing analytic and numerical methods, I break and optimise time-dependence and demonstrate conclusively that this offers no improvement to range and information rate. Then, by additionally breaking passivity, I show that the range and information rate of traditional ESAs can be surpassed.

Contents

Declaration	i
1 Introduction	2
1.1 Introduction	2
1.2 Previous techniques for simultaneously improving bandwidth and efficiency	3
1.3 Thesis Outline	4
2 Background	6
2.1 Antenna Properties	6
2.1.1 Efficiency	6
2.1.2 Reflection and Transmission coefficients	8
2.1.3 Bandwidth and information rate	9
2.1.4 Quality Factor	10
2.2 Limitations of electrically small antennas	10
2.2.1 Limitations on quality factor	10
2.2.2 The relation between quality factor, bandwidth and efficiency . .	12
2.3 Lumped Element Models	14
2.3.1 The Loop Antenna	15
2.3.2 The Dipole Antenna	16
2.3.3 Sources	16
2.3.4 Matching networks for electrically small loop and dipole antennas	16
2.4 Kirchoff's Laws	17
2.4.1 Current and Voltage Laws	18
2.5 Breaking assumptions of the Chu and Wheeler-Chu limits	19
2.5.1 Parametric processes	19
2.5.2 Methods for introducing parametric interactions	20
2.6 Conclusion	22

3 A Generalized Wheeler-Chu Limit	23
3.1 Introduction	23
3.2 Derivation	23
3.3 Comparison	24
3.4 Conclusion	25
4 Time-Dependent Antennas	26
4.1 Motivation	26
4.2 Loop Antenna model	27
4.2.1 Introducing time-dependence	29
4.3 Loop antenna analytic method	29
4.4 Loop antenna analysis using the analytic method	33
4.5 Dipole antenna models	34
4.6 Time-domain simulation technique	36
4.7 Comparison with the analytic method	40
4.8 Optimisation	43
4.8.1 Parameter Space	45
4.9 Optimisation Results	48
4.10 Discussion of optimised results	51
4.11 Chapter Conclusion	52
5 Parametric Amplification	54
5.1 Motivation	54
5.2 Breaking passivity using modulation	55
5.3 Antenna models and analysis methods	57
5.3.1 Modification of the numerical time-domain method	57
5.4 Parametrically amplified loop antenna	59
5.4.1 Circuit setup	59
5.4.2 Parametric Instability	60
5.4.3 Numerically-predicted stability	61
5.4.4 Comparison of analytically and numerically-predicted instabilities	62
5.5 Simultaneous maximisation of bandwidth and efficiency	64

5.5.1	Comparison to the Bode-Fano and Wheeler-Chu limits	65
5.5.2	Dependence of bandwidth and efficiency capacitor modulation phase	67
5.5.3	Relative Strength of the carrier and sidebands	70
5.6	Extension to capacitive antennas	70
5.7	Dipole with variable capacitor	72
5.7.1	Simultaneous maximisation of bandwidth and efficiency	72
5.7.2	Dependence on the capacitor's modulation phase and source phase	74
5.7.3	Relative strength of the carrier and sidebands	76
5.8	Chapter Conclusion	76
6	Thesis Conclusion	78
6.0.1	Conclusion	78
6.0.2	Future work and Limitations	80
A	Appendix	81
A.1	Source voltage used for time-domain method	81
A.2	The operator D in equation 4.13	82
A.3	Dipole Antenna model values	82
A.4	Optimisation Bounds	83
A.5	Test scoring function used for peak maximisation	83
A.6	ODEs used for time-domain simulations of loop, dipole and dipole with varactor antenna	84
A.7	Square Wave function	84
Bibliography		86

Introduction

1.1 Introduction

Modern communication and sensing relies on the transmission, reception, and interpretation of information encoded in electromagnetic radiation. To transmit and receive electromagnetic radiation, an antenna is used. An antenna converts between electromagnetic radiation and currents and voltages - which are easily recorded, interpreted and generated [1]. To transmit electromagnetic radiation, a power source accelerates charges within the antenna, which radiates electromagnetic radiation into the far field. When receiving, an incoming electromagnetic plane wave induces an electromotive force within the antenna, which can be read across its terminals [2].

Driven by the miniaturisation of key technologies in batteries and semiconductors, antenna applications in drones, mobile communication devices, sensor networks, implanted devices and the internet of things have arisen [3]. This miniaturisation has become so extreme that antenna size h is the limiting factor in design. Simultaneously, it is desirable for these antennas to transmit and receive larger wavelength λ electromagnetic radiation due to its superior propagation characteristics [1]. These requirements necessitate antennas of size h much smaller than the wavelength λ of radiation that they transmit or receive; such antennas are called Electrically Small Antennas (ESAs).

Through pioneering work in the 1940s by Wheeler [4], Chu [5], Bode [6], Fano [7] and later many others [8–16], the Wheeler-Chu limit was developed, which gives a fundamental trade-off between the efficiency and bandwidth of ESAs. In practical terms, this means that ESAs can communicate over long ranges or have a high rate of data transmission; not both. However, both of these attributes are desirable [3]. Critically, the Wheeler-Chu limit only applies to antennas that have a linear relation between current

and voltage (Linearity), have time-invariant properties (Time-Invariance) and don't introduce additional energy (Passive); we call such an antenna LTIP [3, 6, 7]. By breaking any of the LTIP conditions, the Wheeler-Chu limit, and thus the limitations on efficiency and bandwidth can be overcome.

1.2 Previous techniques for simultaneously improving bandwidth and efficiency

There have been many attempts at surpassing the efficiency and bandwidth bounds on ESAs imposed by the Wheeler-Chu limit. Early techniques in the 1960s involved Antenna Keying (AK) in which time-invariance was broken to shift the antenna's resonant frequency to the desired transmission frequency [3, 17]. In doing so, the antenna operates at its resonant frequency across a larger frequency range - increasing its bandwidth without sacrificing efficiency. However, this technique requires the signal to be known beforehand so that the antenna's resonance can be shifted accordingly [3]. For receiving, this is not feasible.

Other authors broke linearity, passivity and time-dependence using Negative Impedance Converters (NICs) to emulate negative capacitors and inductors [18]. These exotic negative capacitors and inductors cancel the capacitance and inductance in the antenna over a wide frequency range, yielding both high efficiency and bandwidth. However, such NICs introduce noise, and at radio-frequencies, cannot be used in transmitting antennas due to the large voltages involved [18].

More recently, other authors [19–22] have explored modulating the impedance of an antenna in time. These proposals fall into two categories. In the first, the time-invariance condition of the Wheeler-Chu limit is broken in the antenna by modulating the antenna's properties at below the antenna's signal frequency. Through preliminary work by Liu [23] and theoretical work by Manteghi [22], this technique has been proposed to increase efficiency and bandwidth simultaneously. The second class of techniques [19, 20] involves modulating an antenna's properties at approximately double the signal frequency. In doing so, additional energy is added to the antenna through parametric amplification,

breaking the conditions of time-invariance *and* passivity in the Wheeler-Chu limit. By additionally altering the impedance of the antenna away from its ideal values, this technique has been shown to simultaneously increase the bandwidth and efficiency of ESAs for loop antennas [19]. However, neither of these techniques have been shown to break the fundamental efficiency-bandwidth bounds imposed on traditional ESAs by the Wheeler-Chu limit.

1.3 Thesis Outline

In this thesis, we study the two proposals above to increase the bandwidth and efficiency of ESAs outside the Wheeler-Chu limit. Importantly, we study these techniques with the inductive loop *and* capacitive dipole antenna, which cover the two categories of ESAs and thereby show the techniques discussed here apply to a broad class of ESAs.

In the background chapter, we discuss the most fundamental and practically important properties of ESAs such as efficiency, quality factor and bandwidth. We review pioneering work in the field of ESAs by Chu [5], Wheeler [4], and impedance matching by Bode [6] and Fano [7], and discuss the fundamental limitations on, and relations between efficiency, quality factor and bandwidth that this work imposes on ESAs. Next, we discuss methods of analysing antennas in general, and lay the foundations for our methods discussed in later chapters. We conclude with a brief discussion on how time-invariance and passivity can be broken using physical realisable variable capacitors and parametric processes.

In chapter 3, we use the work of Bode [6] and Fano [7] to extend the Wheeler-Chu limit to ESAs connected to LTIP non-dissipative matching networks. **From this, we derive the first major result of the thesis - a general and new bound between efficiency and bandwidth for LTIP ESAs with LTIP non-dissipative matching networks.**

In chapter 4, we break time-invariance using an ideal variable capacitor. Through a built-from-scratch time-domain simulation based on Kirchoff's laws and an analytic method, we explore the effect of time-dependence. Then, using the time-domain simulation, the efficiency and bandwidth of the loop and dipole antennas are optimised with respect to time-dependence using Bayesian optimisation [24]. **From this we obtain**

the second major result of this thesis - that modulating the impedance of an ESA below its source frequency yields no improvement to efficiency and bandwidth.

In chapter 5, we extend the methods of chapter 4 and break time-dependence *and* passivity through parametric amplification. We apply a similar method to other work [19–21] to improve the efficiency and bandwidth of an electrically small loop antenna. We then extend this approach to the dipole antenna using variable capacitors, which is new. We analyse the stability and phase dependence of this technique and conclude that these antennas are practical. **We show that introducing parametric amplification directly into the matching network or antenna can overcome the efficiency-bandwidth bounds on traditional ESAs through comparison to work in chapter 3.**

Background

Readers experienced with circuit theory and the basics of antennas may only need to read sections 2.2 and 2.5.

2.1 Antenna Properties

2.1.1 Efficiency

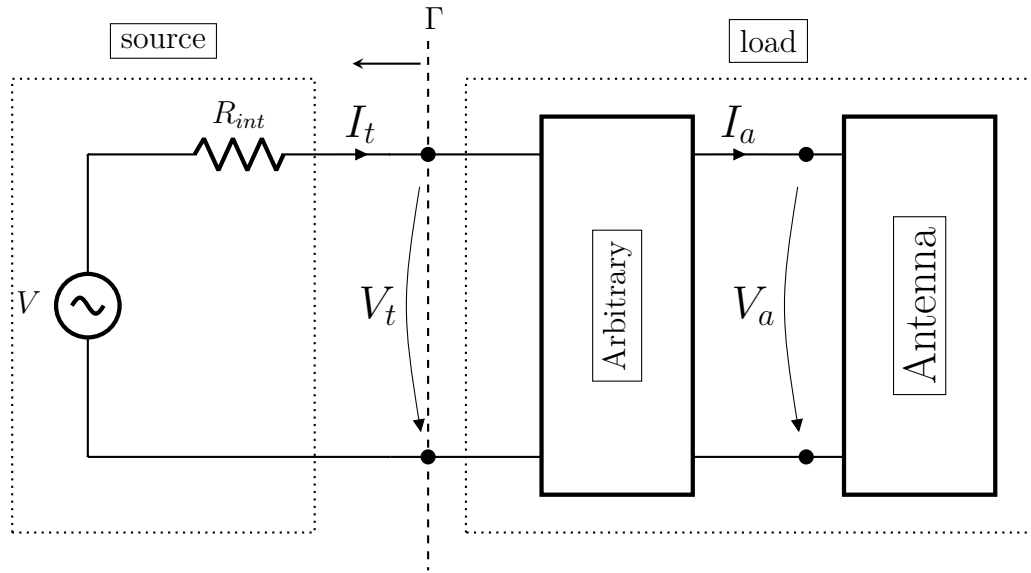


Figure 2.1: A non-ideal voltage source of open circuit voltage V with an internal resistance R_{int} with terminal voltage V_t and current I_t attached to a load composed of an arbitrary circuit and an antenna with terminal voltage V_a and current I_a . The reflection coefficient observed from the source Γ is shown.

The efficiency of an antenna describes how well it converts between energy in the form of incident electromagnetic radiation and energy in the form of currents and voltages in a circuit. It is of great practical importance, as the higher the efficiency of the antenna, the longer its range for communication and sensing [1]. We define efficiency in terms of power ratios. For an antenna (shown in Fig. 2.1) with a time-varying current $I_a(t)$ through it

and potential $V_a(t)$ across it, the power P dissipated in the antenna is:

$$P = \frac{1}{T} \int_0^T I_a(t)V_a(t)dt, \quad (2.1)$$

where T is the period of the function $I_a(t)V_a(t)$ [25]. In this thesis, we will assume the antenna converts all power P dissipated in it into electromagnetic radiation. The antenna is attached to a source of power through some arbitrary circuit (shown in Fig. 2.1). We collectively call the antenna and the arbitrary circuit the “load”, which we connect directly to the power source. Here, the power source pictured in figure 2.1 is a non-ideal voltage source composed of an ideal voltage source V in series with a resistance R_{int} , which is the *internal resistance* of the source. We call the non-ideal voltage source, just the “source” from now on. Following Merenda [26, 27], there are two distinct ways to compute the efficiency of this system, η_a and η_b . Efficiency η_a is the ratio of power radiated by the antenna to the power *available* in the source. Efficiency η_b is the ratio of power radiated by the antenna to the power *delivered* by the source. The power *available* from the source depends on only the source, while the power *delivered* by the source depends on the source *and* the load it is connected to.

The power *available* from the source is the maximum power the source can output. This occurs when the load is a resistor equal to the internal resistance of the source, here R_{int} . [25]. When the source is harmonic $V(t) = V_0 \sin(\omega t + \delta)$, the power available $P_{available}$ is given by [25]:

$$P_{available} = \frac{V_0^2}{4R_{int}}. \quad (2.2)$$

The efficiency η_a is then:

$$\eta_a = 4 \frac{P_L R_{int}}{V_0^2}, \quad (2.3)$$

where P_L is the power dissipated in the antenna calculated from equation 2.1 [25–27].

Efficiencies η_a and η_b are, in general, distinct, and maximising one does not guarantee maximisation of the other [27]. No source is infinite; it will have finite power output and finite total energy to output. If the energy available from the source is constrained while the power is not, then η_b should be maximised. An example of such a source is a battery in a flashlight [27]. If the power available from the source is constrained while the total

energy in the source is not, then η_a should be maximised. An example of such a source is the power outlet in your home. It is common for only η_a to be considered by antenna engineers; however, both are important depending on the application [27]. In this thesis, we primarily consider η_a , which we just call efficiency.

So far, we have considered only a source of a single frequency ω_s . However, due to parametric effects which we introduce later (see Sec. 2.5.1), the source will couple to other modes, exciting frequencies ω in the antenna potentially distinct from the source frequency, ω_s . To incorporate this, we extend our definition of efficiency and define $\eta_{a,\omega}$ (Eq. 2.4) as the ratio of power radiated in the antenna at a frequency ω to the power *available* from the source:

$$\eta_{a,\omega} = 4 \frac{P_{L,\omega} R_{int}}{V_0^2}. \quad (2.4)$$

Here $P_{L,\omega}$ is the power dissipated in the antenna at frequency ω . Using the Fourier transformed current $\tilde{I}_t(\omega)$ through, and potential $\tilde{V}_t(\omega)$ across the antenna, $P_{L,\omega}$ is given by

$$P_{L,\omega} = \frac{1}{2} \operatorname{Re} \left(\Delta \tilde{V}(\omega) \tilde{I}^*(\omega) \right). \quad (2.5)$$

Here, superscript * denotes the complex conjugate [25].

2.1.2 Reflection and Transmission coefficients

In practice, it is difficult to measure the total power radiated by an antenna directly [2]. Instead, it is common to use the power reflected back at the source from the load as a proxy for antenna efficiency [1]. When a wave travels from a medium of impedance Z_s into a different medium of impedance Z_{in} , a fraction of its energy $|\Gamma|^2$ is reflected back, and a fraction of its energy $|T|^2$ is transmitted through the boundary [1, 28]. Γ and T are the reflection and transmission coefficients and given by equations 2.6 and 2.7 [1, 7, 28].

$$\Gamma = \frac{Z_s - Z_{in}}{Z_s + Z_{in}}. \quad (2.6)$$

$$1 = |T|^2 + |\Gamma|^2 \quad (2.7)$$

In our setup, this is analogous to a source with impedance Z_s connected to a load with impedance Z_{in} . The transmission $|T|^2$ can be thought of as the energy that passes from the source into the load. If the arbitrary circuit in figure 2.1 dissipates no energy, and the circuit is LTIP, then efficiency η_a is given by [7]:

$$\eta_a = |T|^2 = 1 - |\Gamma|^2. \quad (2.8)$$

In antennas, the process of minimising the reflection $|\Gamma|^2$ is called impedance matching, as it minimises the difference between the source impedance Z_s and antenna impedance Z_{in} .

2.1.3 Bandwidth and information rate

An antenna operates over a spectrum of frequencies to encode information. However, over this spectrum, the efficiency, and thus the range of the antenna, change [1]. To quantify this, the bandwidth is used. The bandwidth is a continuous range of frequencies $\Delta\omega (|\Gamma_0|)$ over which the reflection coefficient $|\Gamma|$ is below a tolerance $|\Gamma_0|$ [5–7]. Alternatively, through equation 2.8, the bandwidth $\Delta\omega (\eta_{a,0})$ can be defined in-terms of a frequency range over which the efficiency η_a is above a tolerance efficiency $\eta_{a,0}$. This construction is shown in figure 2.2. Note that by changing the efficiency tolerance $\eta_{a,0}$ (dashed line) and thus the acceptable range of the antenna, the bandwidth ($\Delta\omega$) is changed. If this range, $\Delta\omega(\eta_{a,0})$ is centred about a frequency ω_{op} , then the fractional bandwidth $B_f(\eta_{a,0})$ is [14]

$$B_f(\eta_{a,0}) = \frac{\Delta\omega(\eta_{a,0})}{\omega_{op}}. \quad (2.9)$$

In the 1920s and 40s, Nyquist [29] and later Shannon [30] studied the relation between bandwidth and the rate at which information can be sent/received by a device, called the information rate. They showed that the information rate is proportional to the bandwidth, and so maximisation of bandwidth is of direct practical importance for antenna engineers. Through the work of Bode [6] and Fano [7], the bandwidth is tied to the quality factor.

2.1.4 Quality Factor

The quality factor of an antenna is a property of an antenna's materials and geometry. Antennas are made of conductors, which due to their geometry, generate near electric and magnetic fields; giving antennas non-zero capacitance and inductance [1]. When driven by a source, the capacitance and inductance store and release the energy held in the near electric and magnetic fields. Simultaneously, energy leaves the system through far field radiation and ohmic losses such as heating [1, 26, 27]. The ratio of energy stored in the system to that leaving is the quality factor. In an antenna operating at a frequency ω (rad/s), the quality factor Q is the ratio of energy stored in the near electric and magnetic fields W to the power dissipated P over one period $\frac{2\pi}{\omega}$ [8, 10, 16].

$$Q = \omega \frac{W}{P} \quad (2.10)$$

There are different definitions for Q [31, 32]. Here we have followed Chu [5] and used the thermodynamic quality factor.

2.2 Limitations of electrically small antennas

2.2.1 Limitations on quality factor

In the late 1940s, Wheeler and Chu were the first to study the limitations and relations between efficiency, quality factor and bandwidth of Linear Time-Invariant Passive (LTIP) Electrically Small Antennas (ESAs). In 1947, Wheeler [4] studied the tradeoff between quality factor and antenna size for a parallel plate capacitor and a coil inductor antenna.

Wheeler defined the electrical size κ of an antenna operating at a wavelength λ with largest length $2h$ as,

$$\kappa = \frac{2\pi h}{\lambda}, \quad (2.11)$$

and considered an antenna as electrically small if $\kappa \ll 1$. Wheeler found that for ESAs, the quality factor was inversely proportional to the cube of their electrical size κ .

In 1948, Chu [5] studied the tradeoff between quality factor and efficiency for an arbitrary omnidirectional ESA. Chu considered the antenna as an arbitrary current distribution within a sphere of radius h much less than $\frac{1}{2\pi}$ times the wavelength of radiation λ . Assuming no energy was stored in the antenna, he computed the possible fields to find the radiated power and stored energy. From the ratio of stored energy to radiated power he computed the quality factor (Eq. 2.10), and the efficiency directly from the radiated power. By analytically optimising efficiency, quality factor and the efficiency-quality-factor ratio independently, he demonstrated a fundamental tradeoff between efficiency and quality factor as well as a minimum quality factor for omnidirectional ESA. However, Chu failed to give an exact expression for minimum quality factor as a function of electrical size. The work of Chu was extended by Collin [8], Hansen [9] and later McLean [10] to give an analytic lower bound on the quality factor of ESAs. McLean, Collin and Rothschild [10, 16, 33] found the antenna quality factor obeys

$$Q \geq \frac{1}{n\kappa^3} + \frac{1}{\kappa}, \quad (2.12)$$

where $n = 1$ and $n = 2$ for antenna transmitting/receiving radiation using one and two modes respectively. Equation 2.12 is the Chu limit and is not universally accepted. More recent work [11–14] has developed tighter bounds on quality factor Q than equation 2.12. All of these bounds, however, agree that minimum quality factor Q scales with electrical size κ to the power -3 as $\kappa \rightarrow 0$. This is the main result of the Chu limit - that decreasing the size of an antenna will rapidly increase its quality factor. This means that as the antenna becomes smaller, the majority of instantaneous power delivered to the antenna will be stored in the near fields rather radiated into the far field - limiting its performance. This problem is always true for ESAs, as being electrically small requires $\kappa \ll 1$ and so $Q \gg 1$ by equation 2.12.

2.2.2 The relation between quality factor, bandwidth and efficiency

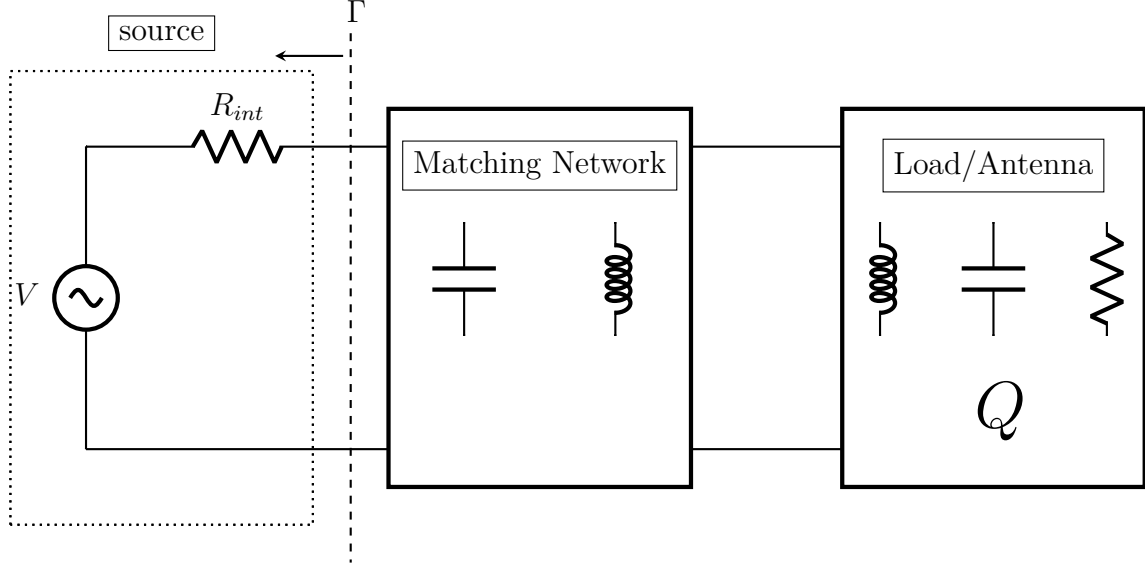


Figure 2.3: A non-ideal source connected to a load or antenna with quality factor Q through a matching network consisting of capacitors and inductors. The reflection coefficient Γ observed by the source is shown.

For high quality $Q \gg 1$ antennas like ESAs, the fractional bandwidth is inversely proportional to its quality factor [12]. To obtain an accurate relation between bandwidth and quality factor, the efficiency tolerance used in the definition of bandwidth [5–7] must be considered [5–7].

In 1945, Bode [6] considered the relation between bandwidth and reflection coefficient $|\Gamma|$ looking from the source in a circuit composed of a matching network and load shown in figure 2.3. The matching network here is any circuit entirely composed of inductors and capacitors. This implies the matching network is LTIP and non-dissipative [6, 25]. For a load composed of a series resistor R and capacitor C , Bode gave the following bound

$$\int_0^\infty \ln\left(\frac{1}{|\Gamma|}\right) d\omega \leq \frac{\pi}{CR}, \quad (2.13)$$

where Γ is the reflection coefficient looking from the source into the matching network and ω is the frequency of the source. Later, Fano [7] generalised Bode's result to parallel and series circuits with a resistor R and inductance L or capacitance C . As discussed in

section 2.3, ESAs are well approximated by these circuits. For an ESA of quality factor Q at an operational frequency ω_{op} with a LTIP non-dissipative matching network, Fano derived [7]

$$\frac{1}{\omega_{op}} \int_0^\infty \ln \left(\frac{1}{|\Gamma|} \right) d\omega \leq \frac{\pi}{Q}. \quad (2.14)$$

Typically, we operate an antenna over a fixed frequency range $\omega_r \in [\omega_{op} - \frac{\Delta\omega}{2}, \omega_{op} + \frac{\Delta\omega}{2}]$ about its operational frequency ω_{op} . Within this frequency range ω_r , we desire an efficiency above some minimum and so desire a reflection coefficient below some maximum $|\Gamma_0|$. Equation 2.14 implies

$$\int_0^{\omega_0 - \frac{\Delta\omega}{2}} \ln \left(\frac{1}{|\Gamma|} \right) d\omega + \int_{\omega_0 + \frac{\Delta\omega}{2}}^\infty \ln \left(\frac{1}{|\Gamma|} \right) d\omega + \Delta\omega \ln \left(\frac{1}{|\Gamma_0|} \right) \leq \frac{\omega_{op}\pi}{Q}. \quad (2.15)$$

To maximise efficiency (minimise $|\Gamma_0|$) in the frequency range ω_r , equation 2.15 implies $|\Gamma| \rightarrow 0$ for frequencies $\omega \notin \omega_r$. This is an important constraint for engineers designing matching networks, as it implies that for best efficiency within a frequency band, matching should be poor ($|\Gamma| \approx 1$) outside of the frequency band. Interpreting $\Delta\omega$ as the bandwidth within which the reflection tolerance $|\Gamma_0|$ is satisfied gives the Bode-Fano limit [6, 7, 16]

$$B_f(|\Gamma_0|) \ln \left(\frac{1}{|\Gamma_0|} \right) \leq \frac{\pi}{Q}. \quad (2.16)$$

where $|\Gamma_0|$ is the reflection coefficient tolerance used to define the fractional bandwidth $B_f(|\Gamma_0|)$. Equation 2.16 implies that large fractional bandwidths $B_f(|\Gamma_0|)$ require large reflection coefficients $|\Gamma_0|$ and thus low efficiencies. This tradeoff between bandwidth and efficiency becomes more extreme as the quality factor Q of the load grows.

The Bode-Fano limit (Eq. 2.16) is not tight. In [15], Yaghjian and Best considered antennas with a matching network consisting of either a single inductor or capacitor in series with an antenna. They assumed the matching network was selected as to maximise efficiency at the antenna's operational frequency ω_{op} ; such an antenna is called a "tuned" antenna. Yaghjian and Best derived

$$B_f(|\Gamma_0|) \lesssim \frac{1}{Q} \frac{2 |\Gamma_0|}{\sqrt{1 - |\Gamma_0|^2}}. \quad (2.17)$$

This is a tighter bound than the Bode-Fano limit (Eq. 2.16) on fractional bandwidth [15]. By assuming that all power dissipated in the antenna is converted to radiation, equations 2.17, 2.8 and the Chu limit (Eq. 2.12) give the Wheeler-Chu limit [16]

$$B_f(\eta_{a,0}) \sqrt{\frac{\eta_{a,0}}{1 - \eta_{a,0}}} \leq \left(\frac{1}{\kappa} + \frac{1}{n\kappa^3} \right)^{-1}. \quad (2.18)$$

Here, $n = 1$ is for single mode antennas, $n = 2$ is for dual mode antennas and $\eta_{a,0}$ is the efficiency tolerance used to define the fractional bandwidth $B_f(\eta_{a,0})$. Critically, the Wheeler-Chu limit guarantees that tuned LTIP ESAs can have either high efficiency (long range) or high bandwidth (large information rate); not both, and this tradeoff between efficiency and bandwidth becomes increasingly unfavourable as electrical size decreases $\kappa \rightarrow 0$. Other authors have experimentally verified a looser Wheeler-Chu limit [16] using a reflection tolerance $|\Gamma_0| = \frac{1}{3}$ to define the bandwidth. They additionally showed that a looser Wheeler-Chu limit, and thus equation 2.18 does not hold for general LTIP matching networks [16, 34]. In chapter 3, we derive a generalised Wheeler-Chu limit for LTIP ESAs with arbitrary LTIP non-dissipative matching networks.

2.3 Lumped Element Models

Antennas have non-trivial input impedance and radiation characteristics which in general cannot be solved for without directly solving Maxwell's equations [35, 36]. This is analytically challenging and numerically expensive [35]. A common method for analysing antennas is to model them as a circuit of resistors, inductors, and capacitors in series and/or parallel - which is easier to solve. The inductors and capacitors model the near electric and magnetic fields. A resistor, called the *radiation resistance* models the conversion of energy into far field electromagnetic radiation. The power radiated by the antenna *is* the power dissipated in the radiation resistance [19, 20].

Here, we consider electrically small magnetic loop and electrical dipole antennas shown in figure 2.4. These antennas are some of the simplest and most commonly used [1]. Importantly, the loop and dipole have capacitive and inductive input impedances, which are the two classes of ESAs [1]. By studying both, we show that the methods discussed in this thesis apply to a broad class of ESAs.

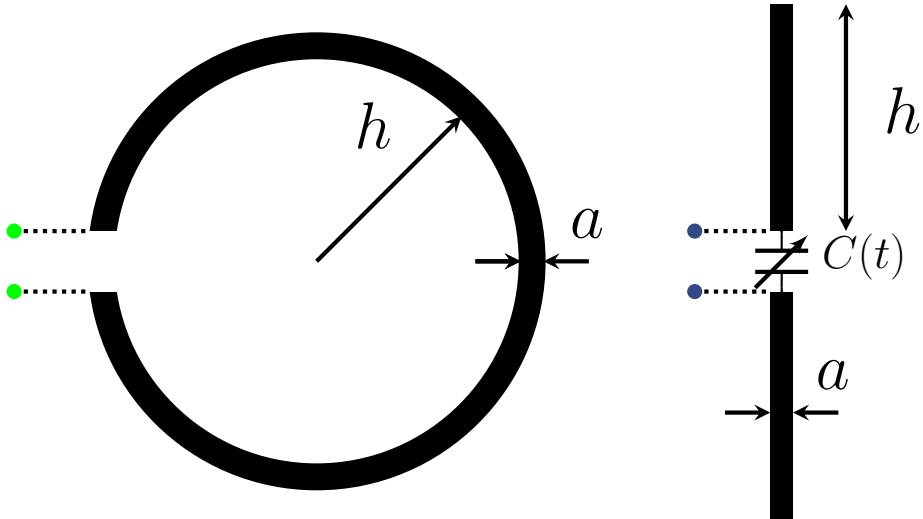


Figure 2.4: Loop (left) and dipole (right) antennas of size h with wire of radius a . The variable capacitor $C(t)$ at the input terminals of the antenna is an addition and not part of the basic dipole antenna. Dotted lines indicate the terminals of the antenna - where it is connected to a circuit. Terminals are colour coded with figures 2.5 -2.8.

2.3.1 The Loop Antenna

The magnetic loop antenna is a conductive wire of radius a wound in a planar loop of radius h with N turns. A loop antenna with $N = 1$ is shown in figure 2.4. Its geometry approximates an inductor and so is modelled as an inductance L_a in series with a radiation resistance R_a . The inductance L_a is:

$$L_a = \mu h \log \left(\frac{8h}{a} - \frac{7}{4} \right), \quad (2.19)$$

where μ is the permeability of free space [37]. The radiation resistance is approximated as:

$$R_a = \left(\frac{177N\omega^2 h^2}{4\pi c^2} \right)^2, \quad (2.20)$$

where ω is the frequency of the radiation being transmitted and c is the speed of light [37].



Figure 2.5: Lumped element model of an electrically small loop antenna. Terminals are colour coded with figures 2.4, 2.6, 2.7 and 2.8.

2.3.2 The Dipole Antenna

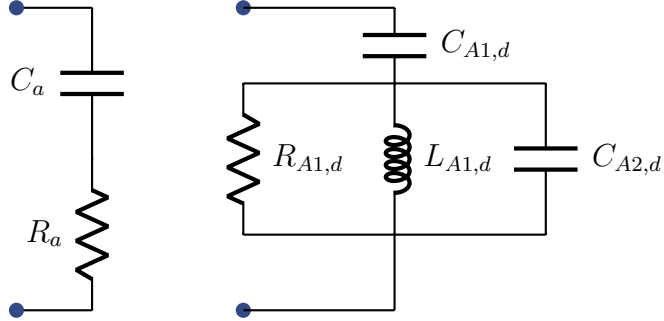


Figure 2.6: Two lumped element models of electrically small dipole antennas. Terminals are colour coded with figures 2.4, 2.5, 2.7 and 2.8

The dipole antenna consists of two wires, each of length h and radius a , as shown in figure 2.4 (right). The dipole antenna is largely capacitive, as it consists of two separated conductors. Because of this, it is approximated as a capacitance and a radiation resistance in series (left) figure 2.6 [27]. In figure 2.6 (left) the radiation resistance scales as ω^4 where ω is the frequency of the current through the antenna [27]. We also use a more complex and accurate dipole model adopted from [38] which is shown in figure 2.6 (right). The values for its components are given in appendix A.3.

2.3.3 Sources

A non-ideal harmonic voltage source is used to stimulate transmission in the antennas. This is modelled using an ideal voltage source of magnitude V and a series resistor R_{int} , which we take as 50Ω as is standard (Fig. 2.7).

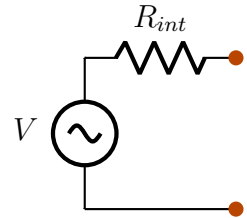


Figure 2.7: Model of a non-ideal voltage source using a series resistor R_{int} and an ideal voltage source V . Terminals are colour coded with figures 2.4, 2.5, 2.6 and 2.8

2.3.4 Matching networks for electrically small loop and dipole antennas

Connecting an ESA directly to the source will yield low performance as the majority of the power input into the ESA will be stored in the near fields and then dumped back into the source where it is lost in the internal resistance [26, 27]. To minimise this

reflection of power, a matching network is placed between the antenna and the source (Fig. 2.3) [1, 2]. If the matching network has no dissipative elements (e.g resistors), then by equation 2.8, minimising the reflection coefficient maximises the antenna efficiency. LC bridge matching networks are chosen for the loop and dipole antennas due to their simplicity. An LC bridge matching network is a non-dissipative circuit consisting of an inductor L and a capacitor C , shown in figure 2.8. The leftmost (red) set of terminals connect to the source. For a dipole antenna, connected across the blue terminals, the inductor L is placed in series to cancel the antenna's capacitance. For a loop antenna, connected across the green terminals, the capacitor C is placed in series to cancel the antenna's inductance [39].

With the antennas connected to their matching networks, values for L and C in the matching network can be found to minimise the reflection coefficient; this is the process of matching. Here, we match the antennas perfectly when the source frequency ω_s equals the central frequency ω_{op} . To do this, we find values of L and C using equation 2.21 [40]

$$|\Gamma(\omega_{op}, L, C)| = 0. \quad (2.21)$$

Equation 2.21 is equivalent to $\text{Re}(\Gamma(\omega_{op}, L, C)) = 0$ and $\text{Im}(\Gamma(\omega_{op}, L, C)) = 0$ and so gives a unique solution for L and C .

2.4 Kirchoff's Laws

The antenna, matching network and source are now in circuit form, whose dynamics are easily solved using Kirchoff's laws. Kirchoff's laws give a set of voltage and current equations in a circuit which can be solved to find all currents and voltages.

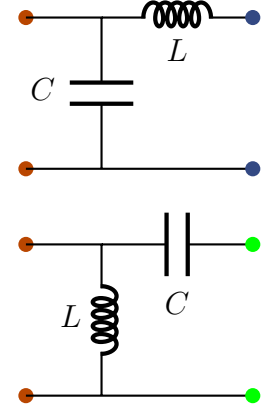


Figure 2.8: LC Bridge matching circuits between source (red) and capacitive dipole antenna (top) and inductive loop antenna (bottom). Terminals are colour coded with figures 2.4 - 2.7.

2.4.1 Current and Voltage Laws

The first law is the current law. It states that the sum of currents into a junction must be equal to the currents coming out of that junction:

$$\sum I_{in} = \sum I_{out}. \quad (2.22)$$

The second law says the voltage drop across any closed loop in a circuit must be zero [41]:

$$\sum_{i \in \{loop\}} V_i = 0. \quad (2.23)$$

Kirchoff's voltage and current laws are coupled through the current-voltage equations of resistors 2.24, capacitors 2.25 and inductors 2.26 [41],

$$V = IR, \quad (2.24)$$

$$I = \frac{d}{dt} (CV), \quad (2.25)$$

$$V = \frac{d}{dt} (LI) \quad (2.26)$$

Together, equations 2.22-2.26 applied to a circuit of inductors, capacitors and/or resistors give a set of time-dependent Ordinary Differential Equations (ODEs) in currents and voltages [42]. If N is the number of derivatives in the set of ODEs, the system can be solved given N consistent independent initial conditions. When the circuit is harmonic with frequency ω , all currents and voltages are of the form $f_0 e^{i\omega t + i\phi}$ where $f_0 \in \mathbb{C}$ and $\omega, t, \phi \in \mathbb{R}$. If C and L are also time-independent, then equations 2.25 and 2.26 reduce to:

$$Z_r = \frac{V}{I} = R, \quad (2.27)$$

$$Z_c = \frac{V}{I} = \frac{-i}{\omega C} = iX_C \quad (2.28)$$

and,

$$Z_l = \frac{V}{I} = i\omega L = iX_L. \quad (2.29)$$

Here Z_r , Z_c and Z_l are the impedances of the resistor R , capacitor C and inductor L respectively. X_C and X_L are the reactances of the capacitor C and inductor L .

For two impedances Z_1 and Z_2 in series, their combined effective impedance is

$$Z_3 = Z_1 + Z_2. \quad (2.30)$$

If Z_1 and Z_2 are in parallel, their combined effective impedance is [41]

$$Z_3 = \frac{1}{\frac{1}{Z_1} + \frac{1}{Z_2}}. \quad (2.31)$$

2.5 Breaking assumptions of the Chu and Wheeler-Chu limits

We have defined and established bounds on the performance of ESAs under the assumption the system is Linear, Time-Invariant and Passive (LTIP). The problem of analysing the antennas has been reduced to a circuit problem, which can be solved using Kirchoff's laws. In this framework, we now consider breaking the LTIP condition. In this thesis, we break the assumptions of time-invariance and passivity using a parametric process.

2.5.1 Parametric processes

A parametric system is one where the properties of the system depend on time. Here, following Yariv [43], we further restrict this definition to systems whose properties associated with energy distribution depend on time. An example is a pendulum driven at a frequency ω_s in which we modulate the pendulum length at a frequency ω_c . By modulating the pendulum length, we modulate the distribution between kinetic and potential energy within the system [3, 43].

Here, we consider an oscillator driven by a source at a frequency ω_s with a property associated with its energy distribution periodically modulated at frequency ω_c - this

breaks time-invariance. By driving the system at a frequency ω_s and modulating its energy distribution at a frequency ω_c , we excite modes of frequencies $\omega_n = \omega_s + n\omega_c, n \in \mathbb{Z}$ in the system [44]. We call the $n = 0$ mode, at frequency $\omega_0 = \omega_s$ the carrier and the remaining modes $\omega_k, k \neq 1$ the sidebands. The distribution of energy between the carrier and sidebands depends on the system.

In this thesis, we consider two cases, the *slow regime*, where energy distribution modulation is much slower than the source $\omega_c \ll \omega_s$ and the *amplification regime*, where the energy distribution is modulated at approximately twice the source frequency $\omega_c \approx 2\omega_s$. In the slow regime, it is assumed that no energy is introduced into the system and $\omega_{\pm 1}$ are supported. The slow regime does not break passivity. The amplification regime is broken into two cases; degenerate and non-degenerate. In the degenerate amplification regime, we modulate the system at exactly double its source frequency $\omega_c = 2\omega_s$, making the carrier ω_0 and sideband ω_{-1} degenerate $|\omega_0| = |\omega_{-1}|$. This means that the carrier ω_0 and sideband ω_{-1} are indistinguishable. In the non-degenerate regime we modulate the system at approximately ($\omega_c \approx 2\omega_s$), but not exactly ($\omega_c \neq 2\omega_s$) twice the source frequency. In both degenerate and non-degenerate cases, the sideband ω_{-1} and carrier ω_0 overlap and modulation introduces or dissipates energy in the carrier ω_0 [43], breaking passivity. Here, we modulate a variable capacitor to stimulate sideband generation and amplification.

2.5.2 Methods for introducing parametric interactions

To modulate the energy distribution in a circuit, a variable capacitor or inductor can be modulated. The most common type of variable inductor uses a ferrite core, which can be modulated in and out of the inductor to vary the local permeability and change the inductance [20]. Instead, we consider variable capacitors realised using varactor diodes, which can be modulated ≈ 1000 times faster than ferrite core variable inductors [45]. Using these variable capacitors then, the modulated antennas discussed in this thesis then can operate at higher frequencies.

A varactor diode uses a p-n junction to produce a voltage-controlled capacitance. The junction consists of a common semiconductor substrate with a conductive negatively

doped n-type and positively doped p-type [46]. The electrons in the n-type and holes (lack of electrons) in the p-type combine in a non-conducting depletion region at the p-n interface, whose width is controlled by the voltage across the diode. This structure approximates a parallel plate capacitor [46]. The p and n-type act as the plates, the depletion region acts as the dielectric filling and a plate distance is controlled by the voltage. By varying voltage across the varactors terminals, the capacitance can be changed.

To realise a variable capacitor (Fig. 2.9 right) a modulation voltage V_m at a frequency distinct from the signal (across the black terminals) and two frequency filters f_1 and f_2 are used (Fig. 2.9 left). The modulation voltage V_m changes the voltage across the terminals of the varactor diode to change its capacitance. The filters f_1 and f_2 stop the signal voltage across the black terminals influencing the modulation voltage and vice versa [47]. The result is an approximate variable capacitor (Fig. 2.9 right). In this thesis, we do

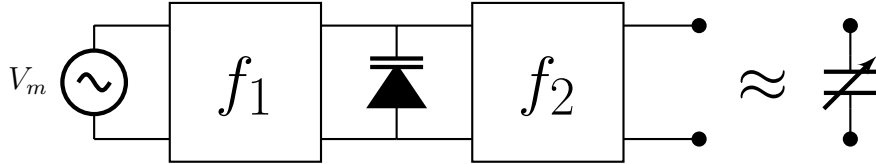


Figure 2.9: Realisation of a variable capacitor with terminals (black) using a varactor diode (black triangle with parallel lines) and two frequency filters f_1 and f_2 with a modulation voltage V_m .

not model the varactor diode in our variable capacitors. Rather, we recognise that such a variable capacitor can be produced and assume an ideal variable capacitor that follows equation 2.25. This simplification ignores non-linearity produced by the diode and the effect of the frequency filters f_1 and f_2 .

2.6 Conclusion

We have defined, and reviewed the fundamental limitations and relations between antenna size, quality factor, bandwidth and efficiency through the early work of Wheeler [4], Chu [5], Bode [6] and Fano [7] for electrically small antennas (ESAs). Using this early work, we rationalised and discussed the Wheeler-Chu limit, which says that Linear, Time-Invariant and Passive (LTIP) ESAs can either have high range or high information rate; not both, and both are desirable. We then simplified the problem of analysing antennas to one of analysing circuits, which through Kirchoff's laws can be solved. Finally, we discussed how the condition of LTIP in the Wheeler-Chu limit can be broken using physically realisable components, potentially allowing for ESAs with superior efficiency (range) and bandwidth (information rate).

A Generalized Wheeler-Chu Limit

Here we derive the first main result of the thesis - a new and more general bound for the efficiency and bandwidth of electrically small antennas.

3.1 Introduction

The Wheeler-Chu limit (Eq. 2.18) bounds the efficiency-bandwidth of tuned LTIP ESAs. Thus, an ESA can either have long range or a high information rate; not both. Here, we generalize the limit to include ESAs with any LTIP non-dissipative matching network. This extension is highly practical, as antennas are commonly connected to complex matching networks to improve bandwidth and thus information rate [1, 35]. The limit derived here is extremely powerful, as it allows us to check if the techniques studied in this thesis surpass the efficiency-bandwidth performance of **all** LTIP ESAs with **any** traditional LTIP non-dissipative matching network.

3.2 Derivation

We consider a LTIP ESA with a quality factor Q attached to a non-ideal source through a LTIP non-dissipative matching network pictured in figure 2.3. By defining a minimum efficiency tolerance $\eta_{a,0}$, we define a bandwidth for this tolerance $B_f(\eta_{a,0})$. As the ESA is LTIP and the matching network is LTIP and non-dissipative, equation 2.8 gives the maximum tolerable reflection coefficient, $|\Gamma_0|$ within the bandwidth:

$$|\Gamma_0| = \sqrt{1 - \eta_{a,0}}, \quad (3.1)$$

where we have ignored the unphysical $|\Gamma_0| < 0$ solution. Applying equation 3.1 to the Bode-Fano limit (Eq. 2.16) gives the modified Bode-Fano limit:

$$B_f(\eta_{a,0}) \ln \left(\frac{1}{1 - \eta_{a,0}} \right) \leq \frac{2\pi}{Q}. \quad (3.2)$$

Applying the Chu limit (Eq. 2.12) to equation 3.2 gives the generalized Wheeler-Chu limit:

$$B_f(\eta_{a,0}) \ln \left(\frac{1}{1 - \eta_{a,0}} \right) \leq 2\pi \left(\frac{1}{\kappa} + \frac{1}{n\kappa^3} \right)^{-1}, \quad (3.3)$$

where κ is the electrical size of the antenna and $n = 1$ for single mode antennas and $n = 2$ for dual mode antennas. In LTIP ESAs and LTIP non-dissipative matching networks the efficiency is less than 1 ($\eta_{a,0} \leq 1$) by energy conservation. Excluding $\eta_{a,0} = 1$, the LHS of equation 3.3 is real and finite. In the perfect efficiency case $\eta_{a,0} \rightarrow 1$, $\ln \left(\frac{1}{1 - \eta_{a,0}} \right) \rightarrow \infty$ and bandwidth is zero ($B_f \rightarrow 0$).

3.3 Comparison

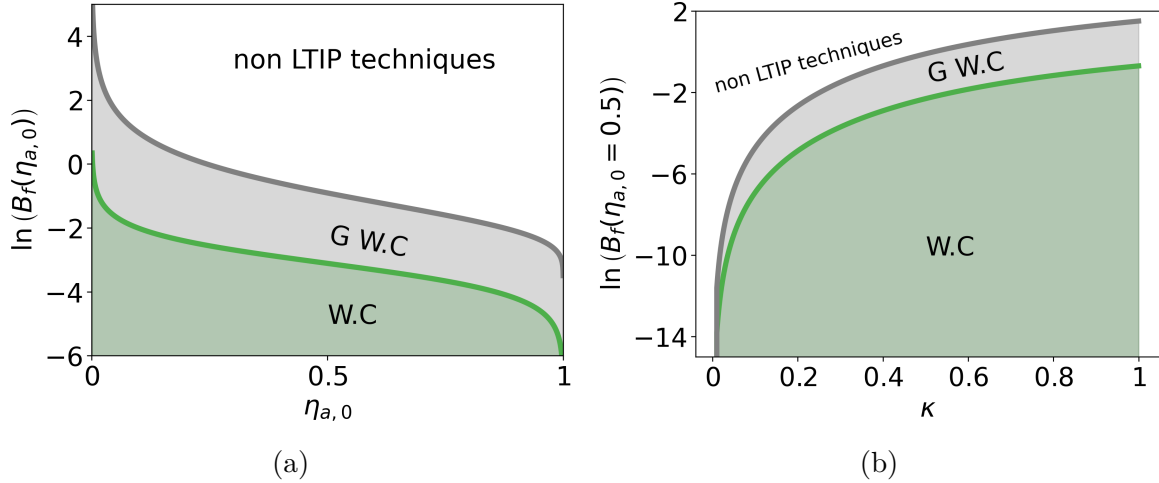


Figure 3.1: The fractional bandwidth-efficiency space permitted by the Wheeler-Chu limit [16] (W.C, green) and generalized Wheeler-Chu limit (G W.C, grey) for a fixed electrical size $\kappa = 0.37$ (a) and a fixed efficiency tolerance $\eta_{a,0} = 0.5$ (b).

The permitted bandwidth-efficiency space in the Wheeler-Chu (green) and generalized Wheeler-Chu (grey) limits are plotted in figure 3.1 for a fixed electrical size $\kappa = 0.37$ with efficiency tolerance varied (Fig. 3.1a) and a fixed efficiency tolerance $\eta_{a,0} = 0.5$ and

electrical size κ varied (Fig. 3.1b). The permitted bandwidth-efficiency region (green) in the Wheeler-Chu limit (Eq. 2.18) is a subset of the permitted bandwidth-efficiency regions (grey) in the generalized Wheeler-Chu limit (Eq. 3.3). This is expected as the generalized Wheeler-Chu limit (Eq. 3.3) allows for an arbitrary LTIP non-dissipative matching network, while the Wheeler-Chu limit only permits a special case. This validates the generalized Wheeler-Chu limit. In this thesis, we break the LTIP condition and achieve super-unity efficiency ($\eta_a > 1$). In this case, the left hand side of the generalized Wheeler-Chu limit (Eq. 3.3) is complex and the limit is ill-defined.

3.4 Conclusion

We have developed a new and more general bound on the efficiency-bandwidth of LTIP ESAs with arbitrary LTIP non-dissipative matching networks. This bound is in agreement with other work [16].

Time-Dependent Antennas

In this chapter, we derive the second main result of the thesis - that modulating an antenna's impedance slower than its source frequency gives no improvement to bandwidth and efficiency. We also develop methods for analysing antennas.

4.1 Motivation

The limits on quality factor, efficiency and bandwidth of Electrically Small Antennas (ESAs) in the Chu and generalised Wheeler-Chu limits (Eq. 2.12 and 3.3) assume the antenna and matching circuit are time-invariant. Here, we break the assumption of time-invariance to surpass the limits on simultaneous efficiency and bandwidth imposed by the generalised Wheeler-Chu limit (Eq. 3.3).

Many authors have broken time-invariance to surpass the limitations on efficiency-bandwidth for transmitting ESAs. The most common is Antenna Keying (AK), developed in the 1950s and 60s [3, 17, 48, 49]. In AK, the properties of the antenna are varied according to the transmitted signal. An example is frequency-key-shifting AK, where the resonant frequency of the antenna is varied (keyed) to match the frequency of the transmitted signal. This allows the antenna to be at resonance across a large frequency range, increasing its efficiency and bandwidth [3]. These AK techniques, however, require prior knowledge of the signal, and are not generally applicable to receiving antennas.

In 2009, Manteghi [22] broke time-invariance in an electrically small antenna; by theoretically modulating the antenna's resonance frequency with a saw-tooth function, he showed frequency-broadening of the antenna's impedance and a decrease in quality factor. Critically, Manteghi's antenna modulation was not varied to accommodate a particular signal - unlike AK, and so allows his technique to be applied to transmitting and receiving ESAs. Manteghi claimed this technique can be used to break the Chu limit

(Eq. 2.18), but did not show it directly [22]. Importantly, lowering the quality factor below the Chu limit implies this technique can break the Wheeler-Chu and generalised Wheeler-Chu limits (eq. 2.18 and 3.3) and increase the efficiency and bandwidth of ESAs. This would allow ESAs to transmit at large information rates over large distances, outside of what is traditionally possible.

More recently, Liu [23] simulated an antenna with resonance frequency modulated by a varactor diode at a frequency much less than the source. By considering the reflection coefficients, a two-fold increase in bandwidth was found.

In this chapter, I test the tantalising potential improvements to efficiency and bandwidth suggested by Liu [23] by considering a magnetic loop and electric dipole antenna with resonance frequency modulated well below the source frequency. Critically, the loop and dipole cover the two classes of ESAs, capacitive and inductive, showing that the results apply to all ESAs. By developing a comprehensive time-domain numerical method and simplified frequency-domain analytic method, I study parametric effects and their qualitative effects on how impedance, reflection coefficient and efficiency vary with source frequency. Through comparison, I analyse the accuracy of the numerical and analytic methods, concluding that the numerical method is more accurate. Finally, using a general resonance frequency modulation much slower than the source frequency, I optimise the efficiency and bandwidth of the loop and dipole antennas. **In this slow frequency modulation regime, I report no improvement in efficiency and bandwidth and explain my results in the context of other work [23].**

4.2 Loop Antenna model

In this section, I introduce the model of the first antenna - the loop antenna. I then show how time-dependence is introduced in this model using a variable capacitor.

An operational frequency of $\omega_{op} = 2\pi \times 10^7 \text{ rad/s}$, a half-length of $h = 1.8m$ and a wire radius of $a = 0.00264m$ is chosen for all antennas. This gives the antennas an electrical size of $\kappa = 0.37 \ll 1$, which we consider electrically small according to Chu's definition [5]. For the loop antenna, one turn of wire is used. The loop antenna (Fig. 4.1), is

modelled as a series inductance $L_{A1,l}$ and resistance $R_{A1,l}$ given in equations 2.19 and 2.20 respectively. The matching network is an LC-Bridge consisting of a capacitor C_0 and an inductor L . For all antennas, a harmonic voltage source of frequency ω_s , open circuit voltage magnitude $V_0 = 1$ V and internal resistance $R_{int} = 50 \Omega$ is used. The entire circuit is shown in figure 4.1. As the circuit is harmonic, equations 2.27 - 2.31

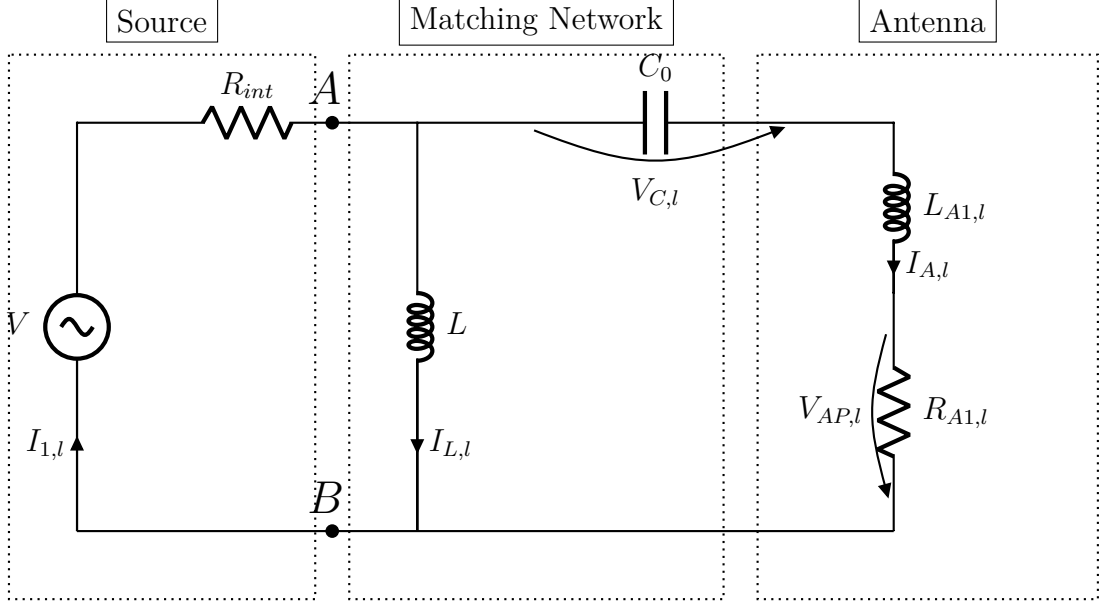


Figure 4.1: A loop antenna modelled as a series inductor and resistor connected to a non-ideal voltage source of internal resistance R_{int} via an LC matching network. The input terminals of the antenna-matching-network circuit are marked with A and B .

apply. The input impedance Z_{in} of the antenna-matching-network circuit (across the terminals A and B) is then

$$Z_{in} = \left(\frac{1}{R_{A1,l} + i(X_{L_{A1,l}} - X_{C_0})} - \frac{i}{X_L} \right)^{-1}, \quad (4.1)$$

where X_y is the reactance of the component y (see Eq. 2.28 and 2.29). We match the antenna with the source at a frequency $\omega_s = \omega_{op}$ by changing L and C_0 . The process of matching minimises the reflection coefficient at $\omega_s = \omega_{op}$, making $Z_s = Z_{in}$ and maximising efficiency η_a by equation 2.8. Equation 2.21 gives the matched values of $L = L_m$ and $C_0 = C_m$ as:

$$L_m = 2.34894 \times 10^{-7} \text{ H}, C_m = 1.61135 \times 10^{-11} \text{ F} \quad (4.2)$$

for the loop antenna.

4.2.1 Introducing time-dependence

To introduce time-dependence, the capacitor C_0 in the matching network is swapped for a variable capacitor $C(t)$ (Fig. 4.2). This capacitor is assumed ideal and follows equation 2.25. To optimise this capacitance, we give it the form

$$C(t) = C_0 \left(1 + \sum_{n=1}^N \epsilon_n \sin(n\omega_c t + \delta_n) \right). \quad (4.3)$$

Here, C_0 is the static capacitance, t is time, ω_c is the smallest modulation frequency and ϵ_n and δ_n parameterise the strength and phase of modulation. N is the number of sine terms used in $C(t)$. Equation 4.3 is a representation of a periodic signal using a Fourier series. For large enough N , the capacitance can be made an arbitrary periodic function. In this chapter, we consider $N = 0, 1$ with a frequency-domain analytic method and $N = 0, 1, 2$ with a numerical time-domain method. The realisation of such a time-variable capacitor is explored in section 2.5.2. In this section, we restrict the largest frequency of modulation, $N\omega_c$, to much less than the source frequency ω_s to not introduce energy and so not break passivity. This variable capacitance modulates the circuit's resonance frequency and energy distribution, making it a parametric process [43].

4.3 Loop antenna analytic method

The first of two methods for analysing the loop antenna is developed - the analytic method. This is a simplified method which we use for checking other more general and complex methods of analysing antennas throughout the thesis.

We develop a simplified frequency-domain analytic method and apply it to the loop antenna circuit in figure 4.2. The goal of this method is to find all currents and voltages throughout the circuit. From this, the input impedance, reflection coefficient, efficiency and bandwidth are determined. The three assumptions for this method are inspired by [19]. First, for simplicity, we assume that the variable capacitance $C(t)$ is modulated with one sine ($N = 1$ in Eq. 4.3). Due to this parametric process, we expect currents

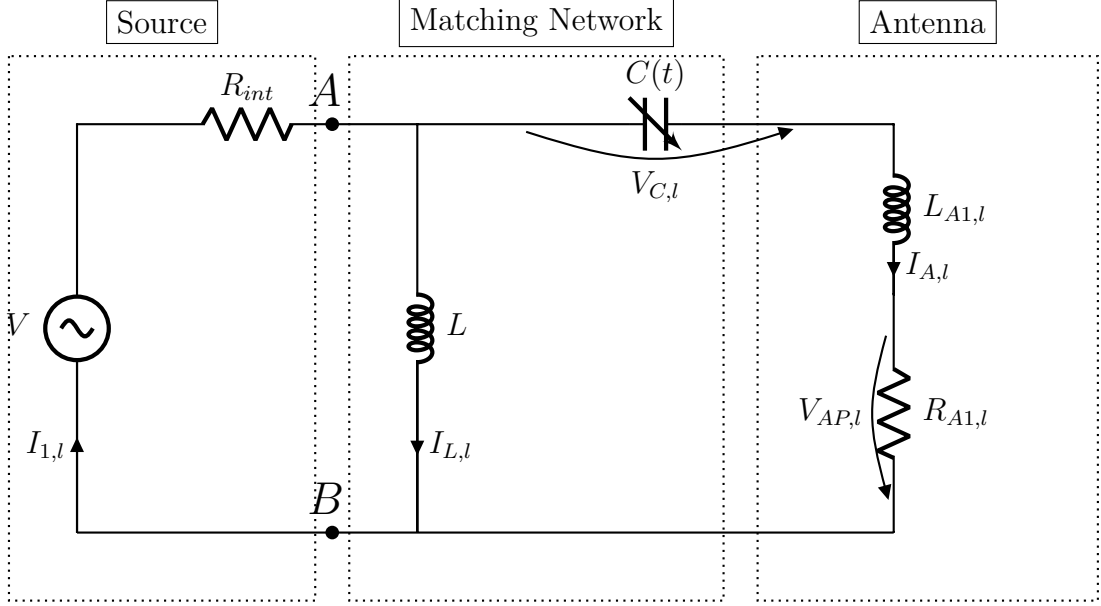


Figure 4.2: A loop antenna modelled as a series inductor and resistor connected a non-ideal voltage source of internal resistance R_{int} via an LC-Bridge matching network. The capacitor in the LC-bridge matching network has been promoted to a variable capacitor $C(t)$. Input terminals of the antenna-matching-network circuit are marked with A and B .

of frequencies $\omega_n = \omega_s + n\omega_c, n \in \mathbb{Z}$ in the circuit; we model three of these - the carrier frequency ω_0 and two sideband frequencies $\omega_{\pm 1}$. Second, we assume that these frequencies are non-degenerate:

$$|\omega_0| \neq |\omega_1| \neq |\omega_{-1}|. \quad (4.4)$$

This assumption allows us to solve each frequency component independently in the circuit. Third, we suppress the frequency ω dependence of the radiation resistance $R_{a,l}(\omega)$ and give it a constant value $R_{a,l}$, equal to its value at the operational frequency $\omega = \omega_{op}$. Due to the first assumption, every voltage drop $v(t)$ (e.g $V_C, l, V_{AP,l}$) and current $i(t)$ (e.g $I_{l,l}, I_{A,l}$) in figure 4.2 is given the form

$$\begin{aligned} v(t) &= \sum_{n=-1}^1 v_n \exp(i\omega_n t) \\ i(t) &= \sum_{n=-1}^1 i_n \exp(i\omega_n t). \end{aligned} \quad (4.5)$$

Here $v_n, i_n \in \mathbb{C}$ are the ω_n frequency components of $v(t)$ and $i(t)$. By equation 2.25 the current $I_{A,l}$ and voltage $V_{C,l}$ across the capacitor $C(t)$ are related by

$$\sum_{n=-1}^1 I_{A,l,n} \exp(i\omega_n t) = \frac{d}{dt} \left(C(t) \sum_{n=-1}^1 V_{C,l,n} \exp(i\omega_n t) \right). \quad (4.6)$$

We divide both sides by $\exp(i\omega_s t)$ to obtain

$$\sum_{n=-1}^1 I_{C,l,n} \exp(in\omega_c t) = \exp(-i\omega_s t) \frac{d}{dt} \left(C(t) \sum_{n=-1}^1 V_{C,l,n} \exp(in\omega_n t) \right). \quad (4.7)$$

Using a Fourier series, we write the RHS of equation 4.7 as:

$$\begin{aligned} \exp(-i\omega_s t) \frac{d}{dt} \left(C(t) \sum_{n=-1}^1 V_{C,l,n} \exp(in\omega_n t) \right) &= a_{-1} \exp(-i\omega_c t) + a_0 + a_1 \exp(i\omega_c t) \\ &\quad + \text{Higher frequency terms}, \end{aligned} \quad (4.8)$$

where the Higher frequency terms¹ are neglected and a_{-1}, a_0, a_1 are the Fourier coefficients associated with frequencies $-\omega_c, 0$ and ω_c . Each Fourier coefficient a_i depends on the voltage across the capacitor $C(t)$, $V_{C,l}$ and the modulation of $C(t)$. Using equation 4.8 with 4.6 gives

$$\sum_{n=-1}^1 I_{A,l,n} \exp(i\omega_n t) = \sum_{n=-1}^1 a_n \exp(i\omega_n t). \quad (4.9)$$

Each frequency component $\omega_0, \omega_1, \omega_{-1}$ is orthogonal due to the assumption of non-degeneracy (Eq. 4.4) and so can be solved independently. For convenience, all currents $i(t)$ and voltages $v(t)$ are recast into matrix form:

$$\tilde{i} = \begin{pmatrix} i_0 \\ i_{-1} \\ i_1 \end{pmatrix}, \tilde{v} = \begin{pmatrix} v_0 \\ v_{-1} \\ v_1 \end{pmatrix}, \quad (4.10)$$

where $v_n, i_n \in \mathbb{C}$ are the ω_n frequency components of $v(t)$ and $i(t)$.

Equation 4.9 is then:

$$\tilde{I}_{C,l} = \tilde{a}, \quad (4.11)$$

¹These high frequency terms $a_k, |k| > 1$ correspond to effects from sidebands $\omega_k, |k| > 1$.

the source voltage is:

$$\tilde{V} = \begin{pmatrix} V_0 \\ 0 \\ 0 \end{pmatrix} \quad (4.12)$$

and the remaining relations derived from Kirchoff's laws are:

$$\begin{aligned} \tilde{V} - \tilde{I}_{1,l} R_{int} - \tilde{V}_{L,l} &= \tilde{0} \\ \tilde{V}_{L,l} &= L \tilde{D} \tilde{I}_{L,l} \\ \tilde{V} - \tilde{I}_{1,l} R_{int} - \tilde{V}_{C,l} - \tilde{V}_{LA1,l} - \tilde{I}_{A,l} R_{A1,l} &= \tilde{0} \\ \tilde{V}_{LA1,l} &= L_{A1,l} \tilde{D} \tilde{I}_{A,l} \\ \tilde{I}_{1,l} &= \tilde{I}_{L,1} + \tilde{I}_{A,l}, \end{aligned} \quad (4.13)$$

where \tilde{D} is given in appendix equation A.3 and all currents and voltages are described in figure 4.2. Here, we use superscript (j) to denote the j th entry of a column vector. For example, $\tilde{i}^{(0)} = i_0$, $\tilde{i}^{(1)} = i_{-1}$ and $\tilde{i}^{(2)} = i_1$ in equation 4.10. The set of linear algebraic equations 4.11-4.13 are solved using Mathematica's Solve function, giving all currents and voltages throughout the circuit.

The input impedance of the antenna-matching-network circuit at the source frequency ω_s is then

$$Z_{in,\omega_s} = \frac{\tilde{V}_{in}^{(0)} - \tilde{I}_{1,l}^{(0)} R_{int}}{\tilde{I}_{1,l}^{(0)}}, \quad (4.14)$$

the reflection coefficient for the source frequency ω_s is

$$\Gamma_{\omega_s} = \frac{Z_{in,\omega_s} - R_{int}}{Z_{in,\omega_s} + R_{int}}, \quad (4.15)$$

and the carrier efficiency η_{a,ω_0} and sideband efficiencies $\eta_{a,\omega_{\pm 1}}$ are given by equation 2.4.

4.4 Loop antenna analysis using the analytic method

Using the analytic method derived above, we show how modulating the capacitor in the loop antenna affects properties of the circuit and discuss their relations to efficiency and bandwidth.

Here using the analytic method, we examine in general terms how modulating the variable capacitance at a frequency ω_c much less than the source ω_s with one sine wave ($N = 1$ in Eq. 4.3) affects the input impedance (Eq. 4.14), reflection coefficient (Eq. 4.15) and efficiency at the carrier $\eta_{a,0}$ and sidebands $\eta_{a,1}$ and $\eta_{a,-1}$.

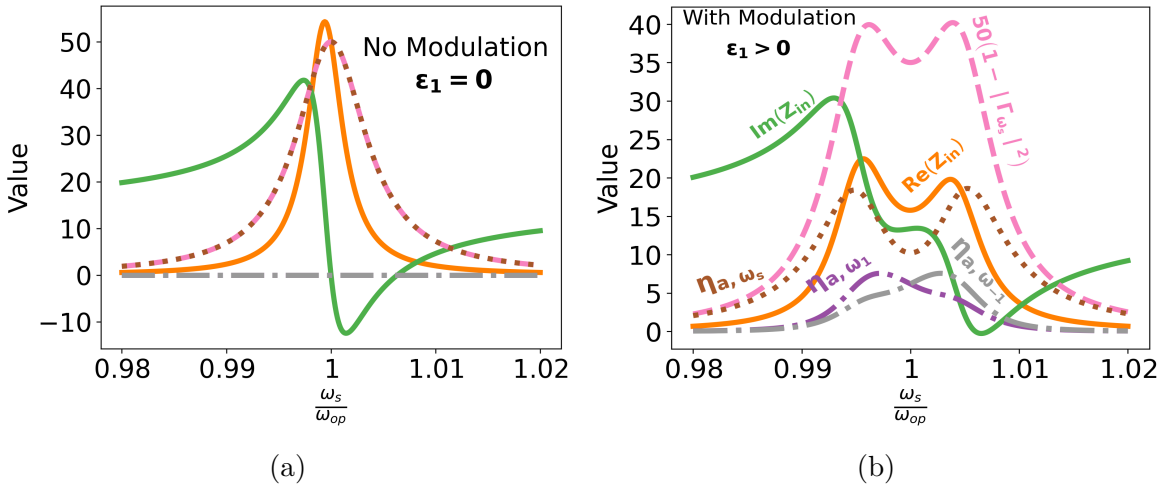


Figure 4.3: The input impedance Z_{in,ω_s} (green and orange solid) from equation 4.14, carrier efficiency $\eta_{a,\omega_s} = 1 - |\Gamma_{a,\omega_s}|^2$ derived from reflection coefficients (pink dashed) (Eq. 2.8) and carrier efficiency η_{a,ω_s} (dotted brown) and sideband efficiencies $\eta_{a,\omega_{\pm 1}}$ (dash-dot purple and silver) derived from power through the radiation resistor (Eq. 2.4). (a) shows no capacitance modulation. (b) shows properties with capacitance modulation. All quantities are expressed as a function of source frequency ω_s . The results are produced using the analytic method (Sec. 4.3) for the loop antenna circuit (Fig. 4.2). The carrier efficiency derived from reflection coefficient overlaps with the carrier efficiency derived from powers in (a). The sideband efficiencies also overlap in (a).

In figure 4.3a, these properties are shown for the loop antenna in the matched case. By definition, matching requires that the real and imaginary components of the input impedance Z_{in} are equal to the source impedance $50 + 0i \Omega$ at the operational frequency $\omega_s = \omega_{op}$. We see this in figure 4.3a, confirming matching is correct. As there is no capacitance modulation, the circuit is LTIP, equation 2.8 is satisfied and $\eta_{a,\omega_s} = 1 - |\Gamma_s|^2$ as seen in figure 4.3a. About the operational frequency $\omega_s = \omega_{op}$, the real (orange) and

imaginary (green) input impedance varies rapidly. Because of this, for small changes in source frequency ω_s , the antenna quickly becomes “unmatched” leading to a low bandwidth. By decreasing the magnitude of the slope of the input impedance, the antenna remains matched over a larger range of frequencies, potentially increasing its bandwidth.

In figure 4.3b we apply capacitance modulation with one sine wave. There are three main results of this when compared to the case without modulation (Fig. 4.3a). First, due to the parametric process, the sidebands (purple and silver dash dot) are excited, leading to a non-zero sideband efficiency. Second, a plateau in the input impedance (green and orange) has occurred near the operational frequency $\omega_s = \omega_{op}$, leading to a more constant efficiency (purple and brown) and thus larger bandwidth near the operational frequency. However, the input impedance at the operational frequency $\omega_s = \omega_{op}$ has deviated from the impedance of the source, decreasing the efficiency. In this chapter, we aim to trade efficiency for bandwidth using capacitance modulation in ways not achievable with traditional techniques. Finally, with the introduction of time-dependence, the pink and brown lines no longer match, implying that $\eta_{a,\omega_s} \neq 1 - |\Gamma_{\omega_s}|^2$. **Critically, this means we can no longer use the reflection coefficient to measure the carrier efficiency η_{a,ω_s} in time-dependent antennas; η_{a,ω_s} must be computed directly using equation 2.4 - this is the main result of this section.**

4.5 Dipole antenna models

We have developed the loop antenna model and briefly analysed it. Here, we develop two distinct models of the dipole antenna - one with a modulated capacitor placed within its matching network and the other with a modulated capacitor placed directly within the dipole antenna.

The first dipole antenna model is from [38], and shown in figure 4.4. In this case, the variable capacitor $C(t)$ is in parallel with the antenna in the matching network as shown in figure 4.4. The second dipole antenna directly incorporates the variable capacitor, placing it across its feed - we call this antenna the dipole antenna with variable capacitor. The construction is shown in figure 2.4. We now develop a lumped element model for the dipole antenna with variable capacitor by extending the lumped element dipole model in

figure 4.4.

The dipole antenna (Fig. 2.4) is two space-separated conductors (arms); these approximate the plates of a parallel plate capacitor. In the dipole lumped element model, $C_{a1,d}$ contributes the majority of the capacitance and so $C_{a1,d}$'s plates model the arms of the dipole antenna. By placing a variable capacitor $C_{a3,dv}(t)$ across the arms of the dipole then, we place $C_{a3,dv}(t)$ across the plates of the capacitor $C_{a1,d}$ in the lumped element model. This is equivalent to placing $C_{a3,dv}(t)$ in parallel with $C_{a1,d}$ in the lumped element model. The resulting lumped element model for the dipole antenna with variable capacitor $C_{a3,dv}(t)$ placed across its arms is shown in figure 4.5. The dipole antenna with variable capacitor uses the same matching circuit as the dipole, except the variable capacitor $C(t)$ in the matching network is replaced by a static capacitor C_0 , as the variable capacitor is incorporated into the antenna.

The antenna half-length $h = 1.8 \text{ m}$, wire radius $a = 0.00264 \text{ m}$ and operational frequency $\omega_{op} = 2\pi \times 10^7 \text{ rad/s}$ for the dipole antennas are the same as the loop antenna.

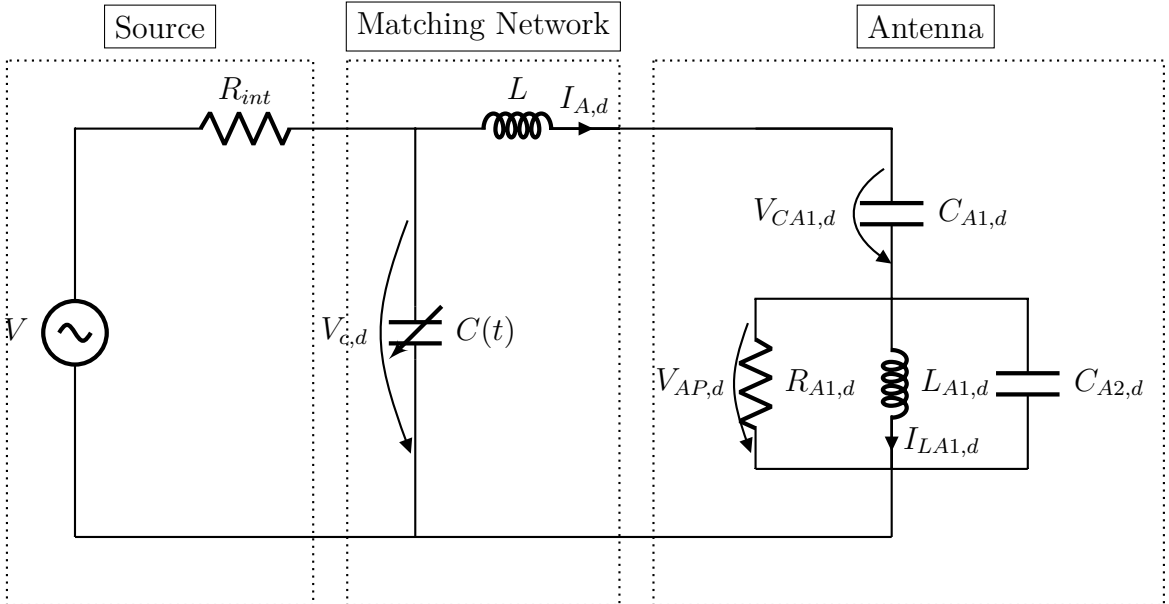


Figure 4.4: A dipole antenna approximated by a lumped element model given in [38] connected to a non-ideal voltage source of internal resistance R_{int} via an LC-Bridge matching network with a modulated capacitance $C(t)$.

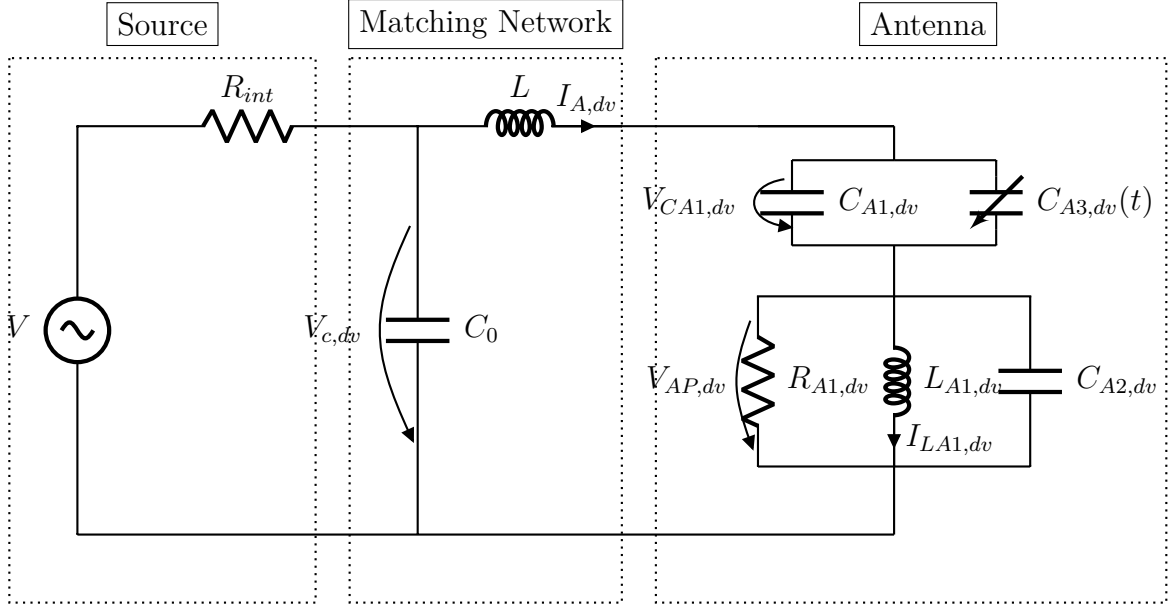


Figure 4.5: A dipole antenna with a variable capacitor placed across its feed approximated by a lumped element model connected to a non-ideal voltage source of internal resistance R_{int} via an LC-Bridge matching network with a modulated capacitance $C_{a3,dv}(t)$.

4.6 Time-domain simulation technique

We have developed computable models for the loop, dipole and dipole with capacitor antennas and developed a limited analytic method for the loop antenna. In this section, we develop a more general time-domain simulation method for use with all antennas studied. This method is used throughout the thesis.

The analytic method developed in section 4.2 is limited. First, it makes restrictive assumptions on frequencies excited in the system. Second, it has only been developed for the loop antenna circuit. Third, it only models capacitance modulation with one sine ($N = 1$ in Eq. 4.3). Of these, only the assumption of non-degeneracy (Eq. 4.4) in the analytic method is fundamental. The analytic method can be extended to all antennas for more complex capacitance modulation incorporating more sideband frequencies. However, the extension to more sideband frequencies and more complex capacitance modulation is analytically challenging; even for Mathematica.

Here, we develop a time-domain simulation for the dipole and loop antennas that incorporates more complex capacitance modulation without assumptions on what frequencies exist in the system. Later in this thesis, this time-domain simulation method

becomes crucial as we explore degenerate parametric amplification, which breaks the non-degeneracy assumption (Eq. 4.4) and thus making the analytic method invalid.

The numerical time-domain simulation is constructed from scratch in Mathematica and Python. Given a source frequency ω_s , the Mathematica program solves a set of ODEs from Kirchoff's laws describing the loop or dipole antenna circuits (figures 4.2, 4.4, 4.5). Unlike the analytic method, this numerical method simulates all frequencies; it then applies signal processing to find the efficiencies of the carrier η_{a,ω_0} and sidebands $\eta_{a,\omega_{-1}}$ and η_{a,ω_1} . A python program repeats this process over a set of source frequencies, giving efficiency against source frequency for the carrier and sidebands.

In the Mathematica program, all initial conditions for currents and voltages in the ODEs are set to zero. These initial conditions are made consistent by setting the voltage source to zero initially. The voltage source is then smoothed over 10 source periods using a \tanh and step function (see appendix Eq. A.1 for exact form). Mathematica's NDSolve finds the currents and voltages for the next 10,000 source periods. The first 5000 source periods are discarded due to transients produced from the initial conditions² and the next 5000 are used to compute the power radiated by the antenna. An example of a current time-series for the loop antenna is shown in figure 4.6. In (b) the transients are seen to last ≈ 100 source periods before periodic behaviour occurs. This is well within the 5000 source-period-long transient time which is discarded. To determine the

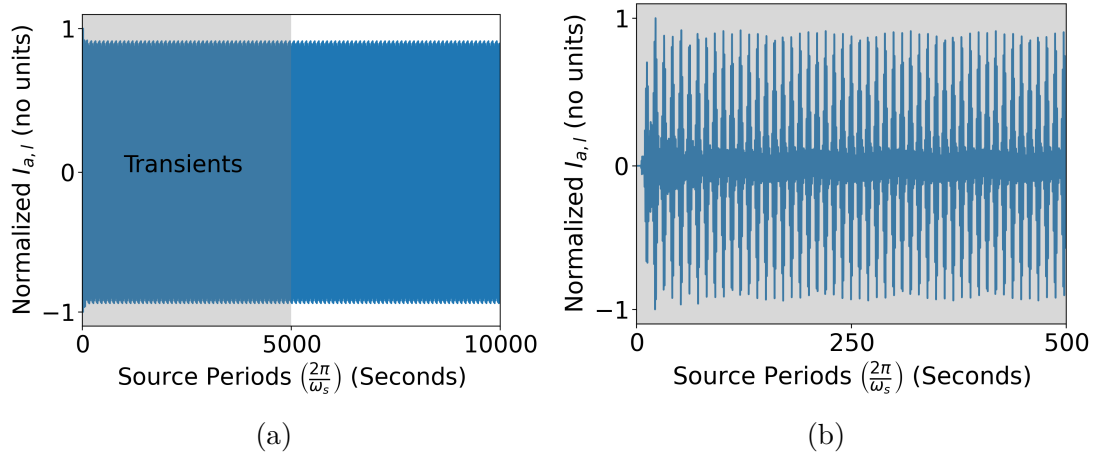


Figure 4.6: The current through radiation resistance $I_{a,l}$ as a function of time for the loop antenna. The data is generated by the numerical time-domain method. (a) shows the long-term dynamics with transient time labelled in grey, (b) shows early dynamics.

²In future different initial conditions should be studied to reduce transient time.

efficiency, we require the power radiated by the antenna - this is the power dissipated in the radiation resistance. The radiation resistance is constant in the dipole antennas and scales as ω^4 where ω is the frequency of the current through the antenna in the loop. For now, we approximate both radiation resistors as constant. Using equations 2.24 and 2.1, the power radiated by the antenna across all frequencies is then:

$$P_{avg,all} \approx \frac{1}{TR_{A1}} \int_0^T V_{AP}(t)^2 dt. \quad (4.16)$$

Due to the capacitance modulation, the antenna will exhibit currents of frequencies $\omega = \omega_s + n\Omega, n \in \mathbb{Z}$ and so radiate electromagnetic radiation at these frequencies. To isolate each frequency component, mathematica's DSTFourier function is used. First, time is discretised by

$$t_i = \frac{i}{S_r}, 0 \leq i < n \quad (4.17)$$

where t_i is the i th time point which occurs at a time $t = t_i$, S_r is the sample rate in Hz and n is the number of time points. The choice of S_r is critical. For a given S_r , the maximum frequency that can be discerned in the discretised data is the Nyquist frequency $0.5S_r$ Hz. Here, we take the sample rate as 10 times the sideband frequency ω_2 . This allows for detection of frequencies $\omega_n, n \in [-2, -1, 0, 1, 2]$ in the system. DSTFourier is used to produce coefficients $U_{AP}(\omega_r), 1 \leq r < n + 1$ satisfying:

$$V_{AP}(t_i) = \frac{2}{\sqrt{n}} \sum_{r=1}^n U_{AP}(\omega_r) \sin(\omega_r t_i), \quad (4.18)$$

where $\omega_r = \frac{\pi}{n} \left(r - \frac{1}{2} \right)$. As $\frac{1}{S_r}$ is significantly smaller than any period considered in $V_{AP}(t)$, we replace discretised time t_i by continuous time t . Using equations 4.16 and 4.18, the power radiated across all frequencies is then

$$P_{avg,all} \approx \frac{1}{TR_{A1}} \int_0^T \left(\frac{2}{\sqrt{n}} \sum_{r=1}^n U_{AP}(\omega_r) \sin(\omega_r t) \right) \left(\frac{2}{\sqrt{n}} \sum_{k=1}^n U_{AP}(\omega_k) \sin(\omega_k t) \right) dt, \quad (4.19)$$

which simplifies to

$$P_{avg,all} \approx \frac{4}{nR_{A1}} \sum_{k,r=1}^n U_{AP}(\omega_r) U_{AP}(\omega_k) \left(\frac{1}{T} \int_0^T \sin(\omega_k t) \sin(\omega_r t) \right) dt, \quad (4.20)$$

$$\lim_{T \rightarrow \infty} \frac{1}{T} \int_0^T \sin(\omega_k t) \sin(\omega_r t) dt = \begin{cases} 0 & \text{if } k \neq r \\ \frac{1}{2} & \text{if } k = r. \end{cases} \quad (4.21)$$

Using equation 4.21 in equation 4.20 gives

$$P_{avg,all} \approx \frac{2}{nR_{A1}} \sum_{r=1}^n U_{AP}^2(\omega_r). \quad (4.22)$$

We now reinstate the frequency dependence of that radiation resistor R_{A1} and put it back under the sum:

$$P_{avg,all} \approx \frac{2}{n} \sum_{r=1}^n \frac{U_{AP}^2(\omega_r)}{R_{A1}(\omega_r)} \quad (4.23)$$

Each term in the sum with index r corresponds to a power at a frequency ω_r . Within a frequency range $\omega_L < \omega < \omega_U$ the total power is then:

$$P_{avg}(\omega_L, \omega_U) = \frac{2}{n} \sum_{r=\lceil \frac{N\omega_U}{\pi} + \frac{1}{2} \rceil}^{\lfloor \frac{N\omega_L}{\pi} + \frac{1}{2} \rfloor} \frac{U_{AP}^2(\omega_r)}{R_{A1}(\omega_r)}. \quad (4.24)$$

Figure 4.7 shows the power through the loop antenna as a function of frequency for a fixed source frequency. The power is radiated at the carrier and sideband frequencies as predicted by section 2.5.1, with the carrier and sidebands being separated by the modulation frequency ω_c . To find the power associated with a carrier/sideband frequency ω_n , we sum the power from frequency $\omega_n - \frac{\omega_c}{2}$ to $\omega_n + \frac{\omega_c}{2}$. Using equation 4.24 the power associated with frequency ω_n is:

$$P_{\omega_n} \approx P_{avg} \left(\omega_n - \frac{\omega_c}{2}, \omega_n + \frac{\omega_c}{2} \right), \quad (4.25)$$

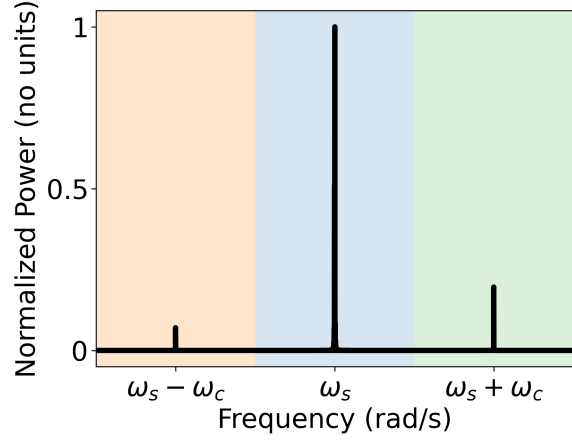


Figure 4.7: The power radiated in the loop antenna (circuit in Fig. 4.2) as a function of frequency for a fixed source frequency. The power is normalised by the power at the carrier frequency ($\omega_0 = \omega_s$). The capacitance $C(t)$ in figure 4.2 is modulated with one sine ($N = 1$ in Eq. 4.3). Coloured and shaded regions indicate where the power is summed over to obtain power at frequency $\omega_s - \omega_c$ (orange), ω_s (blue) and $\omega_s + \omega_c$ (green).

and by equation 2.3, the efficiency is:

$$\eta_{a,\omega_n} = \frac{4R_{int}P_{\omega_n}}{V_s^2} \quad (4.26)$$

Other methods for obtaining the power associated with the carrier/sideband frequencies were explored. These included taking the value of the power at a singular frequency, and fitting the peaks in power as a function of frequency and integrating. The first method fails as the peaks in power at the carrier/sideband frequencies have finite width. The widening is caused by taking a frequency-transform of a function finite in time; this cannot be avoided. Because of this broadening, we need to take the sum over a frequency range in equation 4.25. Automated fitting of the peaks had similar results to the method above (Eq. 4.25). However, in rare cases, the fitting was inaccurate. Later in the chapter, we run optimisation over the efficiency at the carrier frequency. The optimiser was found to exploit fitting inaccuracies rather than optimise the antenna, so fitting was not used.

4.7 Comparison with the analytic method

*The analytic and time-domain methods that we have created are vastly different, currently untested, **and** the basis for much of the results in this thesis. In this section, we verify these methods through comparison and explanation of their results. Through this, we also highlight the limitations of the analytic method.*

Here, we compare the results of the time-domain method (Sec. 4.6) and analytic method (Sec. 4.3) for the loop antenna with simple capacitance $C(t)$ modulation,

$$C(t) = C_0(1 + \epsilon_1 \sin(\omega_c t + \delta_1)), \quad (4.27)$$

where C_0 is the static capacitance, ω_c is the modulation frequency, ϵ_1 is the strength of modulation and δ_1 is the phase of modulation. The values for the matching network, L and C_0 (see Fig. 4.2 and Eq. 4.27), are given in equation 4.2.

The efficiencies at the carrier η_{a,ω_0} (green) and sideband $\eta_{s,\omega_{\pm 1}}$ (purple and blue) are plotted as a function of the source frequency ω_s in figure 4.8. We explain these results

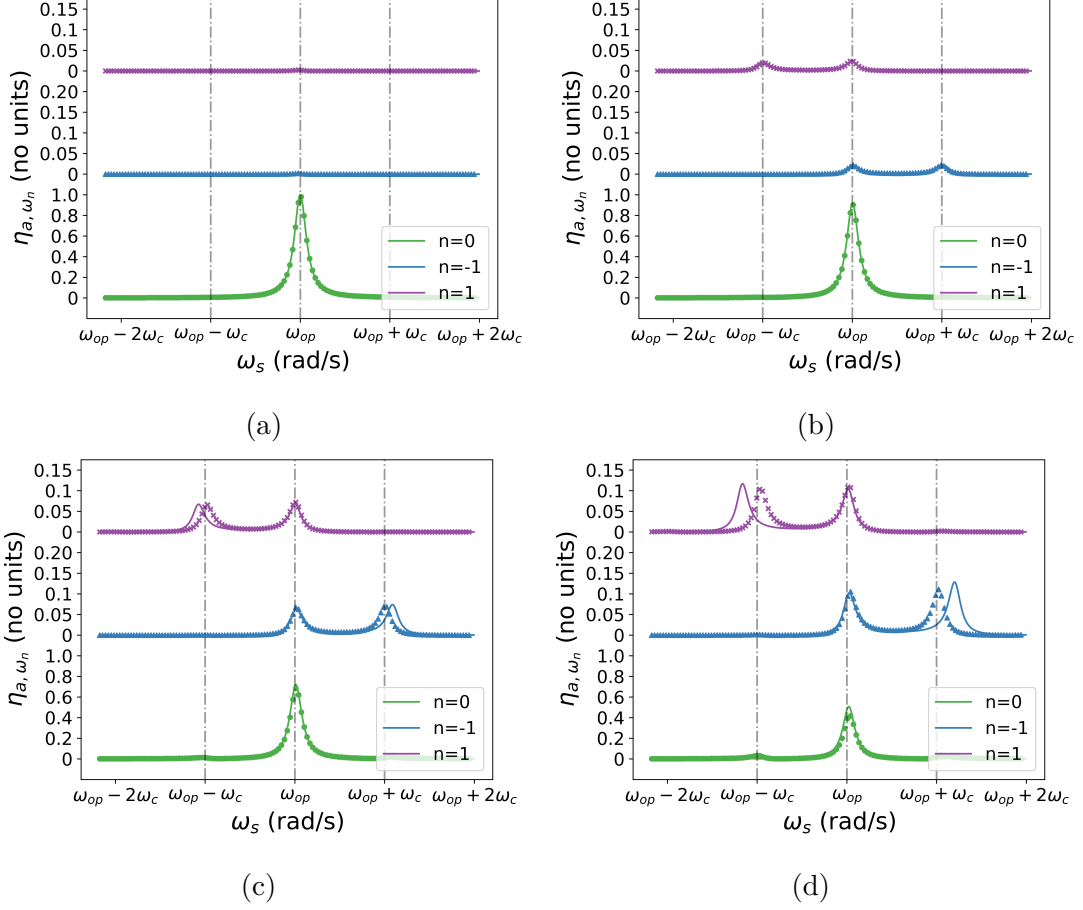


Figure 4.8: A comparison of numerical (points, crosses, triangles) and analytic (solid line) efficiencies for carrier $n = 0$ (green) and sidebands $n = -1$ (blue) and $n = 1$ (purple) for the loop model (Fig. 4.2) with $\epsilon_1 = 0$ (a), 0.03(b), 0.06(c), 0.08(d). Capacitor modulation described in equation 4.27 with $\delta_1 = 0$ and $\omega_c = 0.05\omega_{op}$, $\omega_{op} = 2\pi \times 10^7$ (rad/s). Dashed grey lines indicate source frequencies $\omega_s = \omega_{op}$, $\omega_{op} - \omega_c$, $\omega_{op} + \omega_c$, $\omega_{op} + 2\omega_c$. Values for C_0 and L used in circuit (Fig. 4.2) are given in equation 4.2.

by considering resonance and resonant enhancement of the parametric process

Figure 4.8a (green) shows that with no modulation, the efficiency of the carrier is maximal when the source frequency is the operational frequency, which by construction the circuit resonates at. As the carrier frequency ω_0 is equal to the source frequency ω_s by definition, the peak in carrier efficiency without modulation is due to resonance within the circuit. We note that in figure 4.8a there is no modulation, and so no coupling to the sidebands (green and blue), leading to sideband efficiencies of zero.

In figure 4.8b, the modulation is non zero and two additional peaks appear in each sideband (green and blue). We consider the peak at $\omega_s = \omega_{op} + \omega_c$ in sideband ω_{-1}

(blue) first. Near $\omega_s = \omega_{op} + \omega_c$, the sideband frequency is $\omega_{-1} = \omega_{op}$. Because of this, the sideband is at resonance and so is excited. A similar analysis explains the peak in sideband ω_1 (purple) at $\omega_s = \omega_{op} - \omega_c$. As this process is driven by coupling between the source and sidebands, the peaks in sideband efficiency grow with increased parametric driving ϵ_1 as shown in figures 4.8b - 4.8d.

The peaks in sideband efficiencies (blue and purple) at $\omega_s = \omega_{op}$ are explained by a different mechanism, resonant enhancement of the parametric process. As the source frequency approaches resonance $\omega_s \rightarrow \omega_{op}$, the energy imparted to the circuit by the source increases. Without modulation (Fig. 4.8a) there is no coupling to the sideband frequencies, and all this energy is distributed to the carrier, giving a peak in the carrier efficiency (green) at $\omega_s = \omega_{op}$. With modulation, a fraction of this energy is coupled into the sidebands, giving peaks in the sideband efficiencies (purple and blue) at $\omega_s = \omega_{op}$. As the modulation ϵ increases, the coupling between the source frequency and sidebands increases, coupling a greater fraction of the energy input into the circuit into the sidebands. This explains why the peaks in the sideband efficiencies (blue and purple) grow with growing modulation ϵ_1 .

For small driving $\epsilon_1 = 0$ (Fig. 4.8a) and $\epsilon_1 = 0.03$ (Fig. 4.8a), the analytic results (lines) and numerical results (points) agree with each other and qualitatively with the mechanisms discussed above. **Thus, for small modulations $\epsilon \lesssim 0.03$, the numerical and analytic methods are accurate.** However, as driving increases $\epsilon_1 = 0.06$ (Fig. 4.8a), $\epsilon_1 = 0.09$ (Fig. 4.8a), the analytic results (lines) begin to diverge from the qualitative behaviour discussed and the numerical results (points). This discrepancy in the analytic results arises from the third assumption in the analytic model - that only frequencies ω_0, ω_{-1} and ω_1 exist in the circuit. As the modulation grows $\epsilon > 0$, higher order sidebands $\omega_k, |k| > 1$ appear in the circuit. The analytic model ignores these sidebands (see Eq. 4.8); the numerical model does not. The numerical model solves for a time-series of currents and voltages including all sidebands and then uses a frequency filter to select a subset of them. **For this reason, we take the analytic method as inaccurate for high modulation $\epsilon_1 \gtrsim 0.1$ and consider the numerical method as accurate regardless of modulation ϵ_1 - this is the main conclusion of this section.**

Figure 4.9 shows the circuit has no dependence on the capacitor's modulation phase δ_1 . This is expected, as the source frequency is much larger than the capacitance modulation frequency $\omega_s \approx 10^2\omega_c$, and so any change in phase between the source and the capacitor modulation is averaged out over many periods - leading to no change in the system.

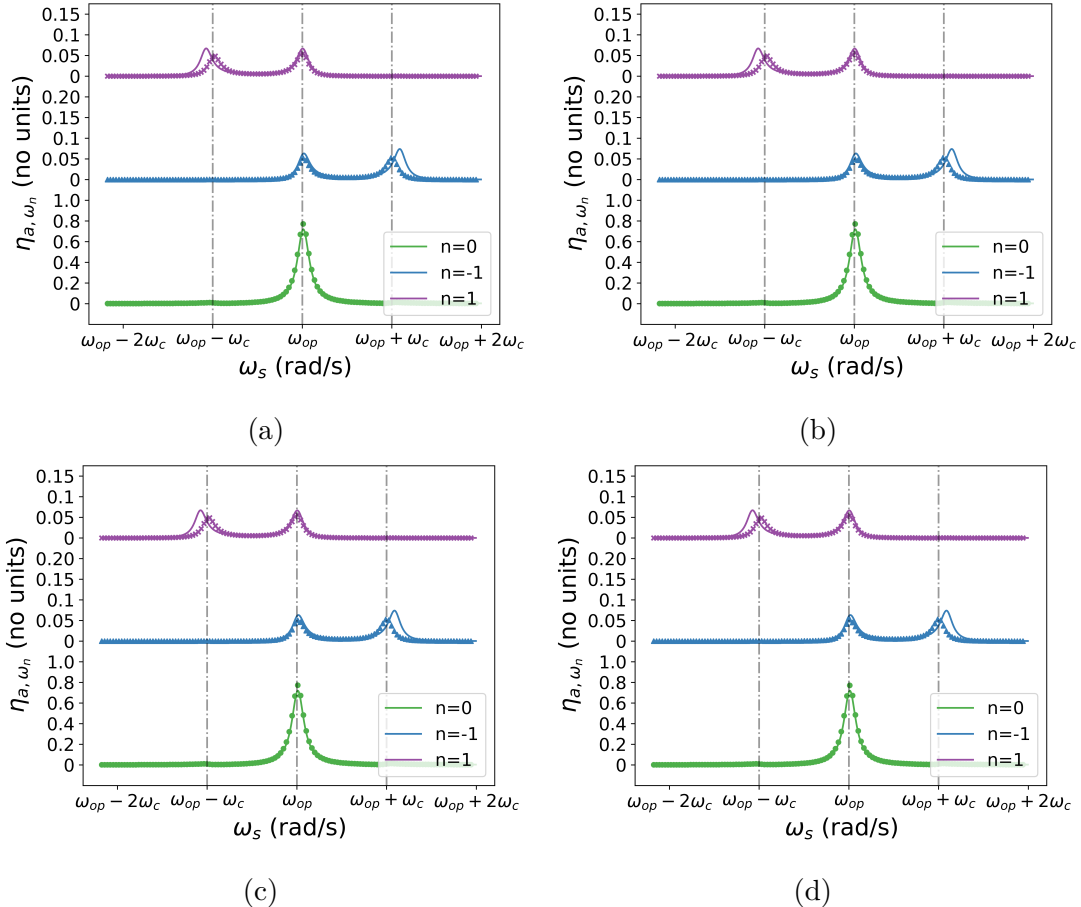


Figure 4.9: A comparison of numerical (points, crosses, triangles) and analytic (solid line) efficiencies for carrier $n = 0$ (green) and sidebands $n = -1$ (blue) and $n = 1$ (purple) for the loop model (Fig. 4.2) with $\delta_1 = 0$ (a), $\frac{\pi}{2}$ (b), π (c), $\frac{3\pi}{2}$ (d). Capacitor modulation described in equation 4.27 with $\epsilon_1 = 0.05$ and $\omega_c = 0.05\omega_{op}$, $\omega_{op} = 2\pi \times 10^7$ (rad/s). Solid (dashed) grey lines indicate source frequencies $\omega_s = \omega_{op}$, $\omega_{op} - \omega_c$, $\omega_{op} + \omega_c$. Values for C_0 and L used in circuit (Fig. 4.2) are given in equation 4.2.

4.8 Optimisation

The three antenna models have been developed, and a time-domain numerical method for analysing capacitance modulation in each antenna has been developed, tested and verified. Now we use the numerical method with optimisation to maximise efficiency and bandwidth of the three antennas with respect to capacitance modulation.

When the antenna source is driven at a frequency ω_s , ideally, the antenna radiates at a frequency ω_s . Then, information encoded in the source by frequency-modulation can be transmitted, received and interpreted. As discussed, due to parametric effects, the antenna transmits the source/carrier frequency ω_s and an array of sidebands $\omega_n = \omega_s + n\omega_c, n \in \mathbb{Z}$. These sideband frequencies are distinct from the source and therefore introduce unwanted noise into the radiated/received signal. At the same time, we desire an antenna with high efficiency and high bandwidth that breaks the generalised Wheeler-Chu limit (Eq. 3.3). Thus, we want to maximise the efficiency η_{a,ω_0} and bandwidth at the carrier frequency, while minimising the efficiency of the sidebands. **In this section, we maximise the efficiency and bandwidth of the carrier.**

A Bayesian optimisation library Bays-opt [50] was incorporated into the Python component of the time-domain simulation program. The program linearly ramps the source frequency ω_s , producing carrier efficiency-source-frequency points $\{(\eta_{a,\omega_0}, \omega_s)\}$. These points are interpolated using cubic interpolation, giving carrier efficiency η_{a,ω_0} as a function of the source frequency ω_s , $\eta_{a,\omega_0}(\omega_s)$. We define a score s on this function by:

$$s = \min_{\omega_s \in \{\Omega_{3B}\}} (\eta_{a,\omega_0}(\omega_s)), \quad (4.28)$$

where $\{\Omega_{3B}\}$ is all source frequencies ω_s within 3 times the bandwidth with an efficiency tolerance of $\frac{1}{\sqrt{2}}$ for the impedance matched antenna with no modulation ($N = 0$). Note that $\{\Omega_{3B}\}$ is different for the three antennas considered here as they have different bandwidths when matched.

Here, interpolation is critical, as the interpolated function is defined for all source frequencies while raw data exists for a finite number of source frequencies. In equation 4.28, s computes the minimum over a source-frequency range. This minimum may not coincide with a data point, leading to an overestimation of s . The interpolated function $\eta_{a,\omega_0}(\omega_s)$ is defined for all source-frequencies and so provided interpolation is accurate, will give a more accurate estimation of s .

The scoring function in equation 4.28 is inspired by the optimal matching condition given in the Bode-Fano limit (Eq. 2.16) - specifically, that efficiency should be constant and maximal within the frequency range of operation. Here, the frequency range of

operation is $\{\Omega_{3B}\}$. In figure 4.10 the properties of the scoring function are qualitatively shown. Figure (a) shows a Gaussian $\eta_{a,\omega_0}(\omega_s)$ function centred about $\omega_s = \omega_{op}$. Figure (b) shows that same $\eta_{a,\omega_0}(\omega_s)$ function shifted in frequency away from ω_{op} has a lower score (red dashed line). Thus, the scoring function incentivises the antenna to have high efficiency for source frequencies near the operational frequency $\omega_s \approx \omega_{op}$. Figure (c) shows that the scoring function takes the minimum over $\{\Omega_{3B}\}$. Thus, it incentivises increasing the minimum efficiency in the frequency range $\{\Omega_{3B}\}$ and so maximises the efficiency and bandwidth. Figure (d) shows how $\eta_{a,\omega_0}(\omega_s)$ under optimal matching according to the Bode-Fano limit (Eq. 2.16) is scored. To summarise, the scoring function is maximal for antennas of high efficiency and high bandwidth operating about a source frequency $\omega_s = \omega_{op}$. The Bayesian optimiser will therefore try to maximise the carrier efficiency and bandwidth about a source frequency equal to the operational frequency $\omega_s = \omega_{op}$.

4.8.1 Parameter Space

Optimisation in the Bayesian algorithm occurs strictly within a predetermined and bounded parameter space. If a maximum lies outside this parameter space, then it will not be found. Simultaneously, a larger search space requires more computation. The choice of parameter space is therefore critical to finding a global score maxima and maximising the efficiency and bandwidth. Here, we optimise over the matching circuit and the modulated capacitance. We include optimisation of the matching circuit, as changing capacitance modulation does influence the matching, as shown in section 4.4. For all antennas, C_0 and L control the static matching and $\epsilon_i, \delta_i, \omega_c$ control the capacitance modulation. The parameters to be optimised are then:

$$L, C_0, \epsilon_i, \delta_i, \omega_c. \quad (4.29)$$

However, in the dipole with the variable capacitor, the variable capacitor's static value $C_{a30,dv}$ changes the antenna impedance and so controls matching. Here, we fix $C_{a30,dv} = C_{a1,dv}$. This choice was found to give similar parametric effects to the loop while not changing the static properties of the dipole with capacitor significantly when compared to the dipole.

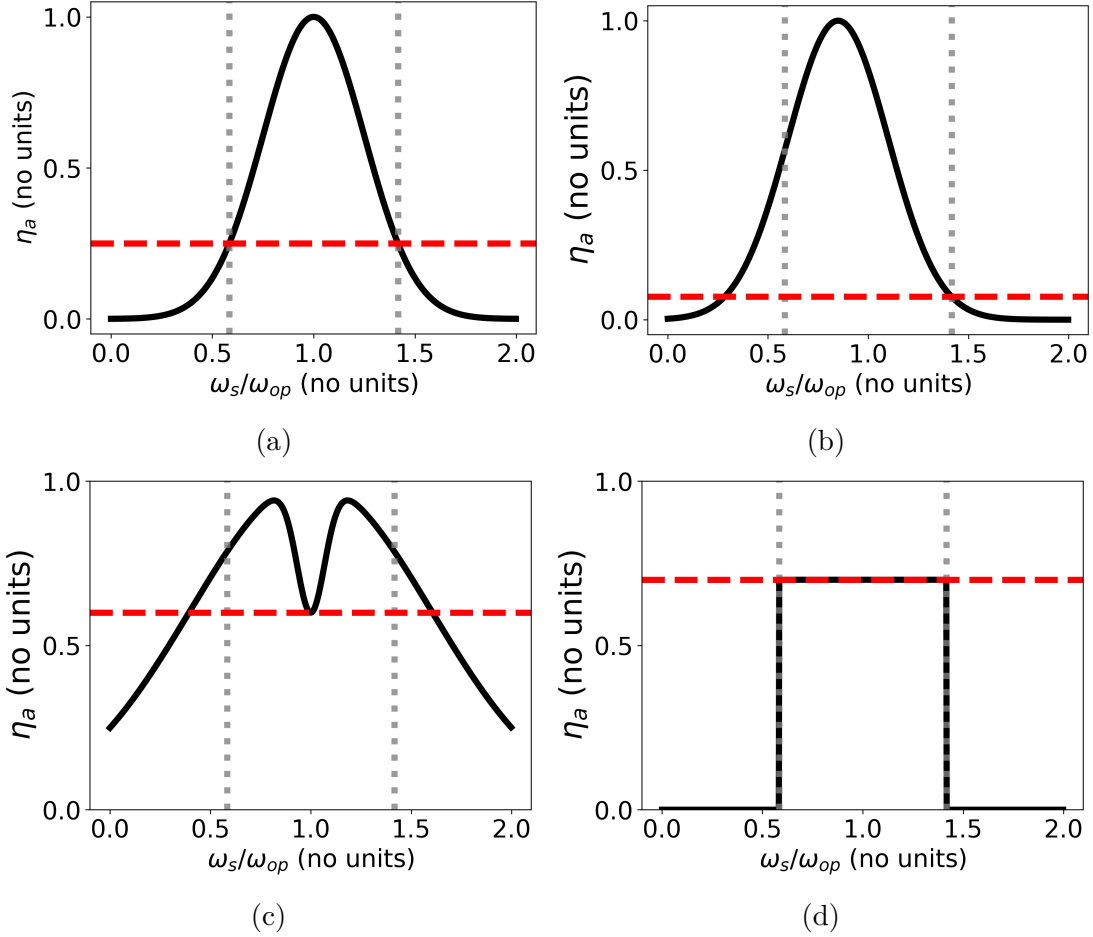


Figure 4.10: Sketch of the score (higher is better) (red dashed line) for idealised $\eta_{a,\omega_0}(\omega_s)$ functions (solid black) showing properties of the scoring function (Eq. 4.28). The region between the dotted grey lines indicates $\{\Omega_{3B}\}$.

Choice of parameter space

In figure 4.8 we see that the source-frequency-location of the η_{a,ω_0} peak does not change drastically with modulation strength. To bound the parameter space of L and C_0 then, we turn off modulation ($N = 0$). The combination of L and C_0 shift η_{a,ω_0} in source frequency ω_s and control its width. We bound C_0 such that for any choice of L , the maximum value of $\eta_{a,\omega_0}(\omega_s)$ can occur anywhere in $\{\Omega_{3B}\}$. Similarly, we bound L such that for any choice of C_0 , the maximum value of $\eta_{a,\omega_0}(\omega_s)$ can occur anywhere in $\{\Omega_{3B}\}$. Following Liu [23], we take ω_c to be approximately 1 to 3 bandwidths of the matched antenna with no modulation ($N = 0$) depending on the antenna (see appendix Sec. A.4). The modulation strengths $\epsilon_i, i \in [1, \dots, N]$ were chosen so that the relative power in the sidebands was at most comparable to the power in the carrier. The relative phase of the

source and capacitance modulation δ_1 was set to zero, and the remaining phases δ_i are free $\delta_i \in [0, 2\pi]$. These standards for parameter space were found to give the optimisation algorithm enough freedom to find optima while still being computable on a laptop in ≈ 1 day.

4.9 Optimisation Results

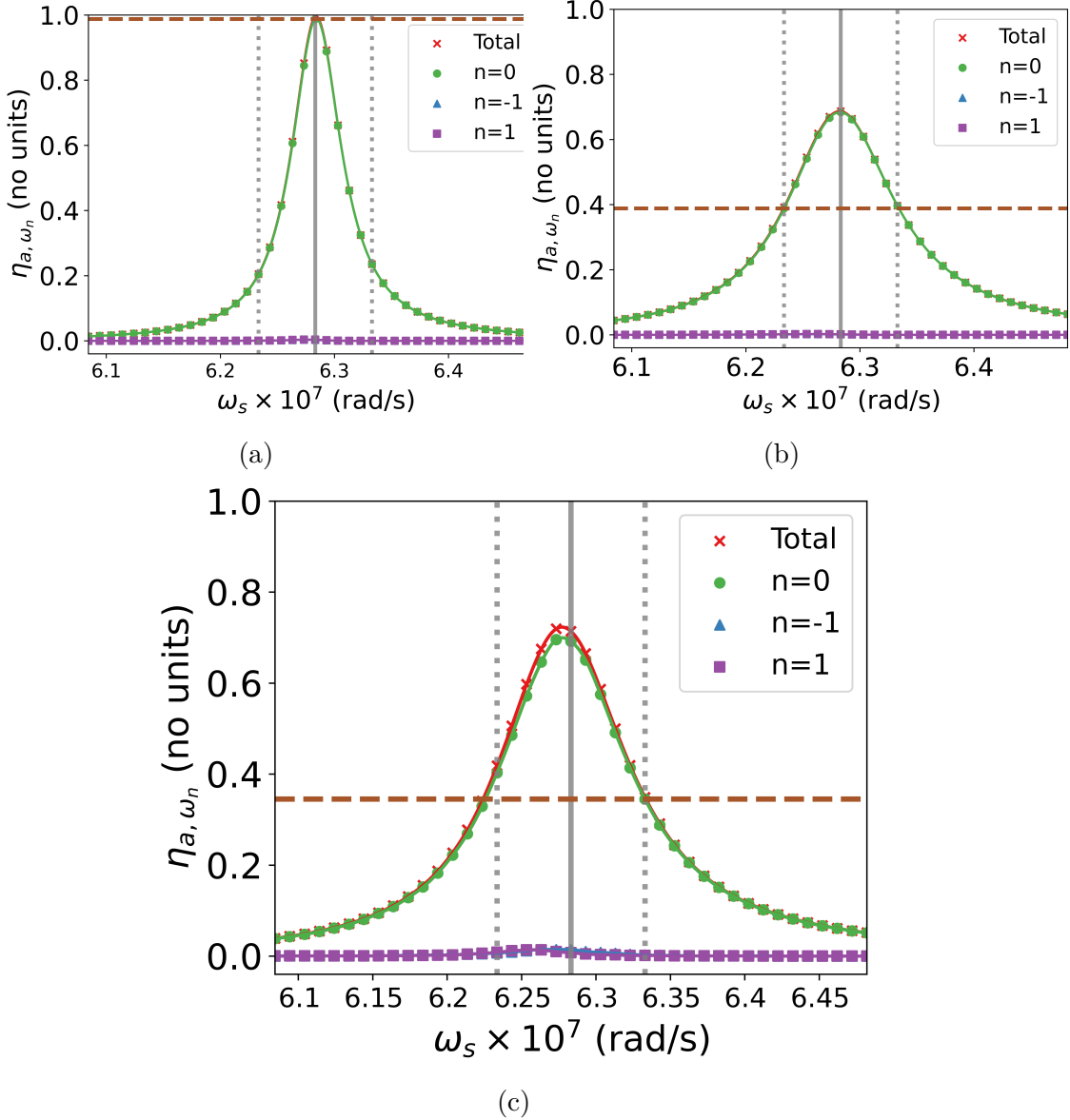


Figure 4.11: The optimisations of the loop antenna (circuit in Fig. 4.2) carrier efficiency η_{a,ω_0} . Optimisation is with respect to $C(t)$ and L , with the parameter space given in equation A.9. (a) shows maximisation of carrier efficiency η_{a,ω_0} for $\omega_s = \omega_{op}$ (score given by Eq. A.11) with no capacitance modulation ($N = 0$ in Eq. 4.3). The following graphics show maximisation of carrier efficiency η_{a,ω_0} in the $\{\Omega_{3B}\}$ (scoring function in Eq. 4.28) region with no modulation $N = 0$ (b) and modulation with two sines $N = 2$ (c). The score maximised in each case is indicated by a horizontal brown dotted line and read on the η_{a,ω_n} axis. $\omega_s = \omega_{op}$ is indicated by solid vertical grey line. The region $\{\Omega_{3B}\}$ is between the two vertical dotted lines. Sideband efficiencies $\eta_{a,\omega_{-1}}$ and η_{a,ω_1} shown with blue triangles and purple squares. Purple squares obscure the blue triangles. Total efficiency of sidebands and carrier $\sum_{n=-1}^1 \eta_{a,\omega_n}$ shown with red crosses.

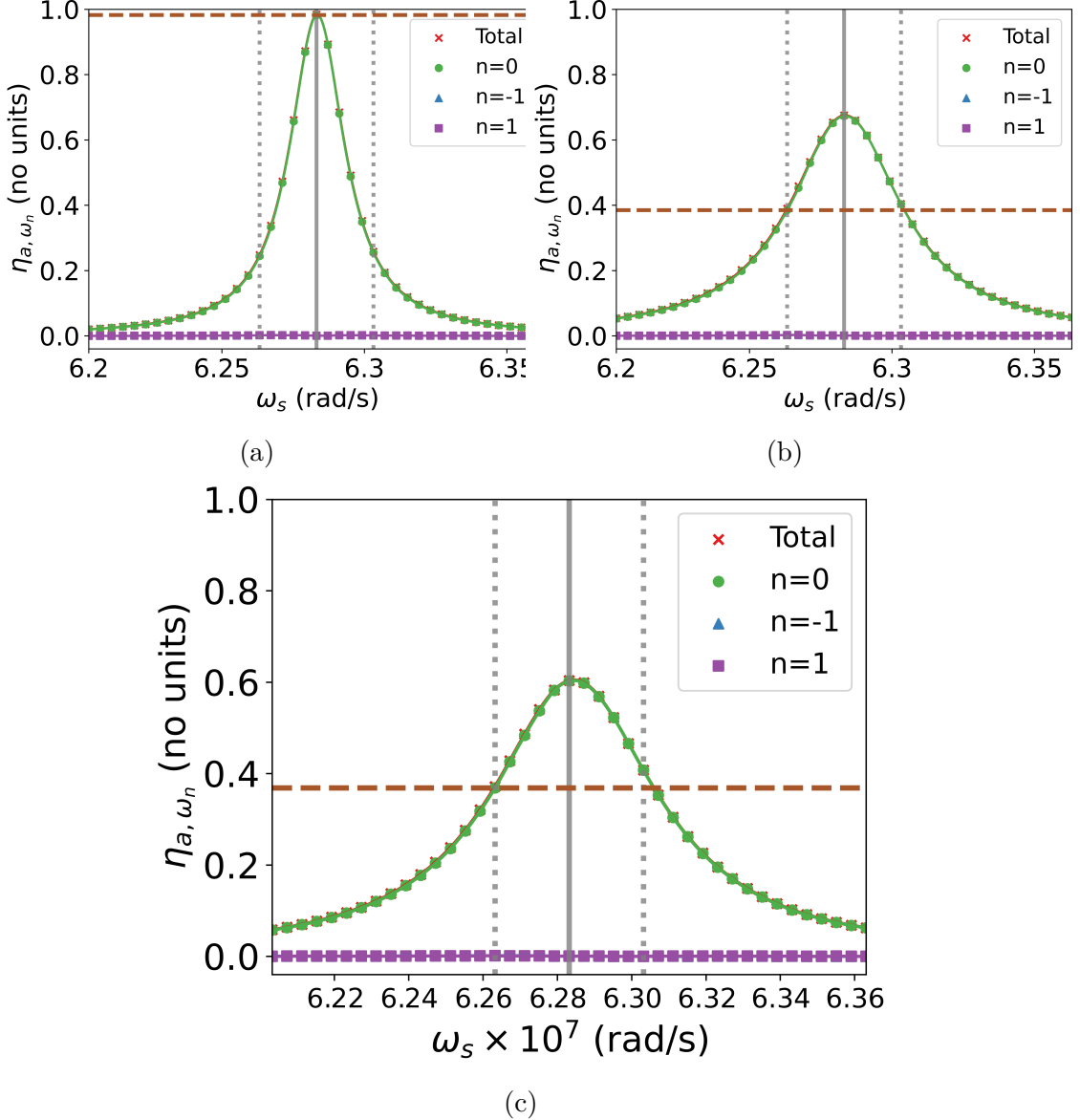


Figure 4.12: The optimisations of the dipole antenna (circuit in Fig. 4.4) carrier efficiency η_{a,ω_0} . Optimisation is with respect to $C(t)$ and L , with the parameter space given in equation A.8. (a) shows maximisation of carrier efficiency η_{a,ω_0} for $\omega_s = \omega_{op}$ (score given by Eq. A.11) with no capacitance modulation ($N = 0$ in Eq. 4.3). The following graphics show maximisation of carrier efficiency η_{a,ω_0} in the $\{\Omega_{3B}\}$ (scoring function in Eq. 4.28) region with no modulation $N = 0$ (b) and modulation with two sines $N = 2$ (c). The score maximised in each case is indicated by a horizontal brown dotted line and read on the η_{a,ω_n} axis. $\omega_s = \omega_{op}$ is indicated by solid vertical grey line. The region $\{\Omega_{3B}\}$ is between the two vertical dotted lines. Sideband efficiencies $\eta_{a,\omega_{-1}}$ and η_{a,ω_1} shown with blue triangles and purple squares. Purple squares obscure the blue triangles. Total efficiency of sidebands and carrier $\sum_{n=-1}^1 \eta_{a,\omega_n}$ shown with red crosses.

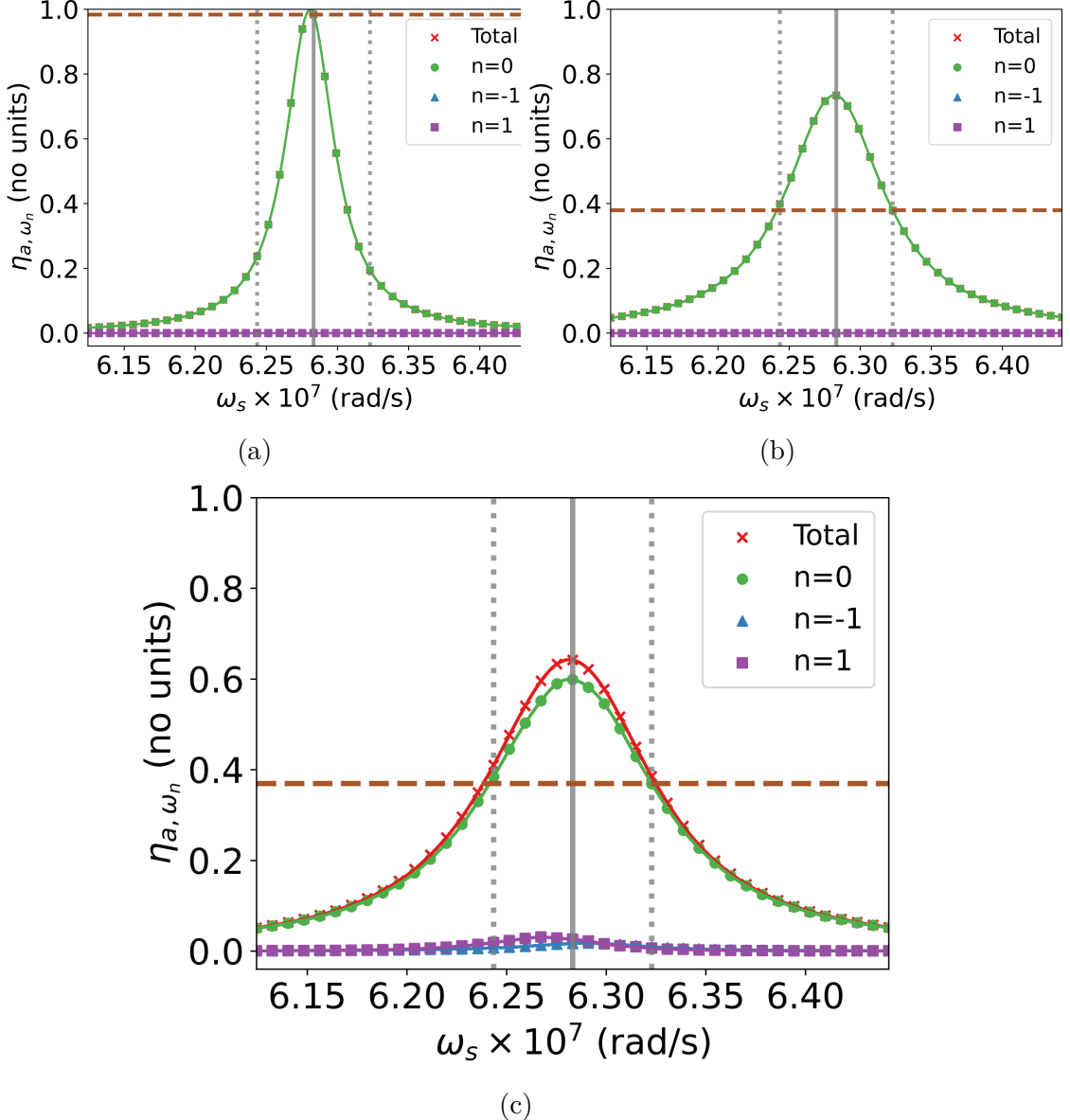


Figure 4.13: The optimisations of the dipole antenna with a variable capacitor placed across its feed (circuit in Fig. 4.5) carrier efficiency η_{a,ω_0} . Optimisation is with respect to $C(t)$ and L , with the parameter space given in equation A.10. (a) shows maximisation of carrier efficiency η_{a,ω_0} for $\omega_s = \omega_{op}$ (score given by Eq. A.11) with no capacitance modulation ($N = 0$ in Eq. 4.3). The following graphics show maximisation of carrier efficiency η_{a,ω_0} in the $\{\Omega_{3B}\}$ (scoring function in Eq. 4.28) region with no modulation $N = 0$ (b) and modulation with two sines $N = 2$ (c). The score maximised in each case is indicated by a horizontal brown dotted line and read on the η_{a,ω_n} axis. $\omega_s = \omega_{op}$ is indicated by solid vertical grey line. The region $\{\Omega_{3B}\}$ is between the two vertical dotted lines. Sideband efficiencies $\eta_{a,\omega_{-1}}$ and η_{a,ω_1} shown with blue triangles and purple squares. Purple squares obscure the blue triangles. Total efficiency of sidebands and carrier $\sum_{n=-1}^1 \eta_{a,\omega_n}$ shown with red crosses.

4.10 Discussion of optimised results

All three antennas, the loop, dipole, and dipole with variable capacitor (circuits in Fig. 4.2, 4.4 and 4.5) follow a similar optimisation process. First, I show using a simple optimisation problem, peak maximisation, that optimisation is working. Second, I optimise efficiency and bandwidth, initially without modulation ($N = 0$) and then, with two-sine modulation ($N = 2$).

In figures 4.11a, 4.12a and 4.13a carrier efficiency η_{a,ω_0} at a source frequency $\omega_s = \omega_{op}$ is maximised without capacitance modulation. This is equivalent to matching the antenna at $\omega_s = \omega_{op}$ which we know gives $\eta_{a,\omega_0} = 1$ at $\omega_s = \omega_{op}$. $\eta_{a,\omega_0}(\omega_s = \omega_{op})$ is the vertical intercept of the dashed brown line. For all antennas, η_{a,ω_0} at $\omega_s = \omega_{op}$ is optimised to ≈ 1 . **This result shows that the Bayesian optimisation algorithm is working.**

In figures 4.11b, 4.12b and 4.13b the efficiency and bandwidth are optimised without capacitor modulation. In figures 4.11c, 4.12c and 4.13c we introduce capacitor modulation. In all cases, the capacitance modulation strength $\epsilon_i, i \in [1, 2]$ was minimised. **This indicates that eliminating capacitance modulation is optimal for simultaneously increasing efficiency and bandwidth.** This result is also seen in the score between figures (b) and (c), with no modulation (b) having a higher score (brown dotted line) and thus a higher efficiency and bandwidth than with modulation (c). The decrease in score with the introduction of modulation is due to an increase in the size of the parameter space; the optimisation with capacitance modulation (c) has 4 more parameters in its optimisation space than optimisation without modulation (b). **We conclude that modulation in this regime gives no improvement to bandwidth and efficiency at the carrier.**

This conclusion disagrees with preliminary work by Liu [23]. In Liu's work, he simulated a transmitting ESA with impedance modulated at ω_c much less than the source-frequency ω_s , with ω_c within the bandwidth of the antenna - similar to the analysis in this chapter. For a given efficiency tolerance, Liu found an increase in bandwidth by a factor of ≈ 2 - which we do not observe. There are two fundamental differences between Lius method and ours. First, Liu simulated the varactor diode used to construct the variable capacitor. This accounts for any non-linearity produced by the varactor diode. Here, we

used an ideal model of the variable capacitor that does not simulate the varactor diode or its non-linearity. Therefore, Liu additionally broke the condition of linearity in the generalised Wheeler-Chu limit (Eq. 3.3), which we do not do here.

More importantly, Liu [23] did not compute the efficiency directly from power, instead using reflection coefficients. In section 4.4, we found that efficiency computed from the reflection coefficients is not equivalent to the efficiency of the antenna when capacitance modulation is non-zero. Here, we have computed efficiency directly.

4.11 Chapter Conclusion

We considered the two classes of electrically small antennas, the capacitive antenna represented by the dipole, and the inductive antenna represented by the loop antenna. Using a variable capacitor modulated at a frequency below the antenna's source frequency, we introduced time-dependence without breaking passivity. We did this to break the limits on efficiency and bandwidth imposed by the generalised Wheeler-Chu limit (Eq. 3.3). In the loop antenna, we introduced the variable capacitor into the matching network. In the dipole antenna, we introduced the variable capacitor into the matching network and the antenna.

The antennas were converted into circuit representations using lumped element models. Two methods for analysing the circuit representation of the antennas were developed based on Kirchoff's laws; a simplified analytic method in the frequency-domain, and a numerical time-domain simulation coded from scratch.

Using the analytic method, the effect of sinusoidal capacitance modulation on reflection coefficient, input impedance, efficiency and bandwidth were qualitatively studied and found to agree qualitatively with [22]. Critically, it was found that efficiency cannot be computed from the reflection coefficient directly with modulation. The analytic and numerical methods were then compared and shown to closely match for small capacitance modulation, validating the numerical method.

Finally, using Bayesian optimisation, the efficiency and bandwidth was maximised with respect to capacitance modulation much slower than the source frequency. **From this, we obtained the main result of this chapter - that modulating the an-**

tenna impedance much slower than the antenna source frequency yields no improvement to bandwidth and efficiency. This disagrees with previous preliminary work by Liu [23] and this discrepancy is explained by an incorrect characterisation of efficiency by Liu and model simplifications made in this work that ignore non-linearity.

Parametric Amplification

Here we develop the third main result of this thesis - that the limits on efficiency and bandwidth for electrically small antennas can be broken using a novel parametric amplification technique.

5.1 Motivation

The Chu limit bounds the quality factor of Linear, Time-Invariant and Passive (LTIP) ESAs, and the generalised Wheeler-Chu limit (Eq. 3.3) bounds the efficiency and bandwidth of LTIP ESAs with LTIP non-dissipative matching networks. Here, we explore breaking the condition of passivity¹ in the generalised Wheeler-Chu limit to simultaneously increase the efficiency and bandwidth of ESAs outside of traditional LTIP techniques, giving an ESA with superior range and information rate. Breaking passivity in antenna engineering is not new; it is the job of the amplifier. The amplifier amplifies the signal from or to the antenna, allowing communication over longer distances.

In [21], Loghmannia and Manteghi used parametric amplifiers and resistors to account for the high quality factor of ESAs guaranteed by Chu (Eq. 2.12). Loghmannia and Manteghi placed a resistor in series with an ESA, trading efficiency for bandwidth. Then, using a parametric amplifier, the efficiency was increased across the bandwidth. Using a loop antenna, they showed this method improves the efficiency and bandwidth of the loop antenna, but did not show the system surpassed the Chu, Wheeler-Chu or generalised Wheeler-Chu limits and so its performance may be achievable with traditional LTIP methods.

In 2021, Mekawy and Li [19] studied a similar loop antenna, with a variable capacitor built into a non-dissipative matching network. By mismatching the antenna with the source and modulating the capacitor in the parametric amplification regime, the bandwidth and efficiency were simultaneously increased. They also study the stability of this

¹A passive system is one which has no introduction of energy aside from the source.

method. Mekawy and Li showed the antenna-matching-network had a lower quality factor than all LTIP antennas using the Chu limit. However, this does not imply the method can surpass the limits on efficiency and bandwidth from the generalised Wheeler-Chu limit, and so its performance may be achievable with traditional antenna techniques.

Here, we consider the method of Mekawy and Li [19]. We first recreate their work by studying a similar inductive loop antenna [19]. We then extend the method of Mekawy and Li to capacitive antennas using variable capacitors, which has not been done before. We use the circuit models, time-domain simulation techniques and analytic methods developed in chapter 4. Practically important limitations on stability and dependence on the phase of the source and capacitor's modulation are analysed. **From this, we show the main result of this chapter - that breaking passivity directly in the antenna or antenna matching network can give efficiency and bandwidth that surpass the bounds on LTIP ESAs with LTIP non-dissipative matching networks..**

5.2 Breaking passivity using modulation

This chapter is about adding energy to an electrically small antenna to break passivity. In this section, I explain though a toy model how modulating a capacitor can introduce energy into the system.

In this chapter, we consider parametric amplification, whereby the input impedance of the antenna-matching-network circuit is modulated at approximately double the frequency of the energy source ω_s [43, 51]. To do this, we place a variable capacitor either in a matching circuit or the antenna and modulate it at approximately twice the source frequency $\omega_c \approx 2\omega_s$. Like chapter 4, this does introduce time-dependence. Unlike chapter 4, this modulation regime breaks passiv-

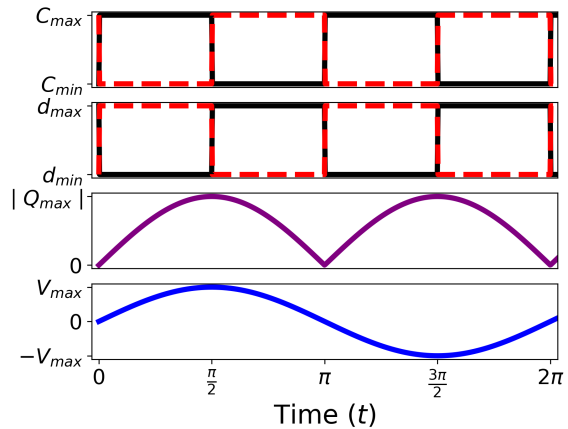


Figure 5.1: A variable parallel plate capacitance C with plate distance d and charge magnitude $|Q|$ modulated at double the frequency of a voltage source V across its terminals. Two phases $\delta_1 = 0$ (black) and $\delta_1 = \pi$ (red dashed) of the variable capacitor are shown.

ity via parametric amplification [51] - and is the defining trait of this regime. Through a simplified qualitative model, I explain how capacitance modulation at twice the source frequency introduces energy and breaks passivity.

Consider a circuit with a voltage $v(t) = \sin(t)$ across a parallel plate capacitor $C(t)$ given by:

$$C(t) = C_0(1 + \epsilon_1 f(2t + \delta_1)), \quad (5.1)$$

where $f(x)$ is the square wave function with period 2π and amplitude 1 (shown in appendix A.2), ϵ_1 is the strength of modulation and δ_1 is the phase between the capacitance modulation and the source. We consider small modulation $\epsilon_1 \ll 1$ and ignore its effect on the voltage $v(t)$ and charge magnitude $|Q(t)| = |C_0v(t)|$ [52] on the plates of the capacitor. Note that the capacitor has two plates, one charged to Q the other charged to $-Q$. If $d(t)$ is the distance between the plates of the capacitor, then $d(t) \propto \frac{1}{C(t)}$ [52]. The modulation of the capacitance $C(t)$ and plate distance $d(t)$ is shown in figure 5.1 for phases $\delta_1 = 0$ (black) and $\delta_1 = \pi$ (red). With $\delta_1 = 0$ at time $t = 0$, the uncharged capacitor plates move together, requiring no work. When $t = \frac{\pi}{2}$, the now oppositely charged plates are pulled apart. This does work on the circuit, adding energy. This two-step process repeatedly adds energy to the circuit. When $\delta_1 = \pi$ (red) the opposite is true. When the plates are oppositely charged, they are moved together, so the circuit does work on the capacitor. **This simplified model of degenerate parametric amplification shows how modulating a capacitor at twice the source frequency introduces/dissipates energy and so breaks passivity.** How much energy is introduced/dissipated depends on the relative phase of the source and the capacitance modulation. The energy imparted by/on the capacitor will appear as an increase/decrease in magnitude of voltage and charge.

5.3 Antenna models and analysis methods

The parametric amplification regime that we study in this chapter has different behaviour to the slow modulation regime we studied in chapter 4. In this section, we study and then adapt our analysis methods to this new regime.

In this chapter, we study the same loop, dipole, and dipole with variable capacitor antennas with the same models (Fig. 4.2, 4.4, 4.5) as in chapter 4. To analyse these antennas in the parametric amplification regime, we use the same analytic method in section 4.3 and extend the time-domain numerical method of section 4.6

Consider our variable capacitor $C(t)$ modulated with one sine ($N = 1$) oscillating at frequency ω_c (see Eq. 4.3) at approximately double the source frequency $\omega_c \approx 2\omega_s$. Then, currents and voltages of frequencies (carrier $n = 0$ and sidebands $n \neq 0$) $\omega_n = \omega_s + n\omega_c, n \in \mathbb{Z}$ are excited in the system [51]. Note that sidebands ω_k have a negative frequency for $k < 0$, and so appear as a frequency $|\omega_k|$ in the system. Degenerate parametric amplification occurs when the capacitor is driven at twice the source frequency $\omega_c = 2\omega_s$. In this case, frequencies ω_n and ω_{-n-1} are degenerate ($|\omega_n| = |\omega_{-n-1}|, \forall n \in \mathbb{Z}$) and so cannot be distinguished. Non-degenerate parametric amplification occurs when the modulation frequency ω_c is not an even integer multiple of the source frequency ω_s ($\omega_c \neq 2k\omega_s, k \in \mathbb{Z}$). In this case, all frequencies excited in the system are non-degenerate ($|\omega_i| \neq |\omega_j| \forall i \neq j$) and can be distinguished. For simplicity, we consider carrier ω_0 and sideband frequencies ω_{-1}, ω_1 only. Other sideband frequencies $\omega_k, |k| > 1$ are weaker, as they exist at frequencies outside the resonance of the antenna-matching-network circuit.

The analytic model of section 4.3 assumes that the carrier and sidebands are non-degenerate ($|\omega_0| \neq |\omega_{-1}|$). This is false in the degenerate parametric amplification regime. **The analytic method we use is therefore restricted to the non-degenerate parametric regime.**

5.3.1 Modification of the numerical time-domain method

Here we adapt the time-domain method to select power associated with the carrier and sidebands and compute efficiencies in the parametric amplification regime. In chapter 4, the carrier and sideband frequencies were separated by the modulation frequency ω_c , in-

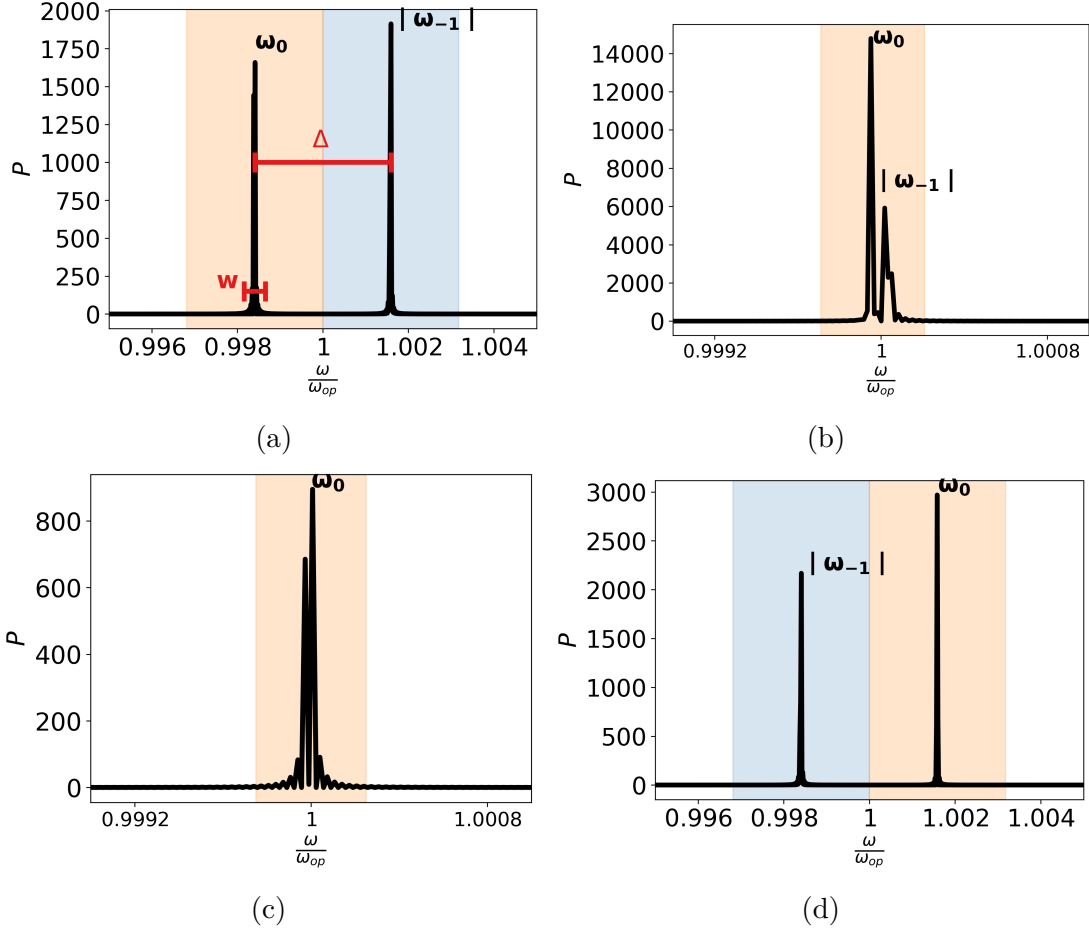


Figure 5.2: The power radiated P by the loop antenna (circuit in Fig. 4.2) as a function of frequency ω , with capacitance modulation at frequency ω_c about two times the source frequency ω_s . The peaks are labelled by frequency ω_0 or $|\omega_{-1}|$ with width w and gap Δ between them. The orange region is the power associated with the carrier frequency, the blue region is the power associated with the sideband ω_{-1} . (a) shows $\omega_c > 2\omega_s$, (b) shows $\omega_s < 2\omega_c$ with the gap between carrier ω_0 and sideband $|\omega_{-1}|$ frequencies comparable to peak width. (c) shows degenerate parametric amplification where $\omega_c = 2\omega_s$. (d) shows $\omega_c < 2\omega_s$. Then time-domain method of section 4.6 is used to produce the results.

dependent of the source frequency. In the parametric regime, the sideband frequency ω_{-1} appears as a positive frequency $|\omega_{-1}|$ in the circuit. Figure 5.2 shows how changing the source frequency ω_s (panes a-d) changes the power spectrum through the antenna. The peaks in figure 5.2 at the carrier ω_0 and sideband $|\omega_{-1}|$ frequencies have a characteristic width w due to broadening, and a frequency-gap $\Delta = |\omega_0 - |\omega_{-1}||$ between them. When the frequency-gap is much larger than the width $\Delta \gg w$ (Fig. 5.2a and 5.2d), the power

associated with the carrier/sidebands frequency ω_n , P_{ω_n} is given by

$$P_{\omega_n} = P_{avg}(|\omega_n - \Delta/2|, |\omega_n + \Delta/2|), \quad (5.2)$$

where P_{avg} is given in equation 4.24. In figure 5.2, the frequency range used to compute the carrier power P_{ω_0} and sideband $P_{\omega_{-1}}$ is shaded orange and blue, respectively.

When the separation between the carrier and sideband frequencies Δ is comparable to the peak widths w (Fig. 5.2b and 5.2c), the frequencies ω_0 and ω_{-1} are considered degenerate. Then, the power associated with the carrier P_{ω_0} includes the power from the ω_{-1} and ω_0 regions and is given by:

$$P_{\omega_0} = P_{avg}\left(\left|\frac{\omega_0 + \omega_{-1}}{2} - w\right|, \left|\frac{\omega_0 + \omega_{-1}}{2} + w\right|\right). \quad (5.3)$$

As Δ may be less than the peak width w in this case, the power associated with the frequency ω_1 is given by a region of frequency-width w

$$P_{\omega_1} = P_{avg}(|\omega_1 - w/2|, |\omega_1 + w/2|). \quad (5.4)$$

The rest of the time-domain simulation is the same and applies to the degenerate and non-degenerate cases.

5.4 Parametrically amplified loop antenna

Our analytic and numerical methods have been adapted for the parametric amplification regime. In this section, we use these methods to study the loop antenna with parametric amplification.

5.4.1 Circuit setup

We consider the loop antenna circuit in figure 4.2. We operate the antenna about an operational frequency $\omega_{op} = 2\pi \times 10^7 \text{ rad/s}$ with the capacitance $C(t)$ given by

$$C(t) = C_0(1 + \epsilon_1 \sin(\omega_c t + \delta_1)), \quad (5.5)$$

where $\omega_c = 2\omega_{op}$, ϵ_1 is the strength of driving and δ_1 is the phase of driving. Like chapter 4, we use a sinusoidal source $V(t) \approx \sin(\omega_s t)$, so the phase δ_1 is the relative phase between the source and the variable capacitor. The setup is otherwise the same as in chapter 4.

5.4.2 Parametric Instability

Here we discuss how a parametrically amplified system can become unstable and explain how this stability can be qualified in the analytic method.

When the power delivered by parametric modulation overcomes dissipation in the circuit, the circuit exhibits negative real input impedance and becomes unstable [43]. This instability is characterised by exponentially growing currents and voltages [43]. The input impedance, Z_{in,ω_0} seen by the ideal voltage source (see Fig. 4.2) is

$$Z_{in,\omega_0} = \frac{\tilde{V}_{in}^{(0)}}{\tilde{I}_{1,l}^{(0)}}. \quad (5.6)$$

Here we have used the notation of the analytic model for voltages and currents (see Sec. 4.3). We compute \tilde{V}_{in} and $\tilde{I}_{1,l}$ using the analytic model and obtain Z_{in,ω_0} in equations 5.7 and 5.8. The expressions for Z_{in,ω_0} are valid only in the non-degenerate regime ($\omega_s \neq \omega_{op} = \frac{1}{2}\omega_c$) due to the degeneracy assumption (Eq. 4.4) of the analytic model. Critically, Z_{in,ω_0} depends on the source frequency ω_s , driving ϵ_1 (see Eq. 5.5) and the parameters of the circuit (see Fig. 4.1); it does not depend on the relative phase between the source and the capacitor modulation δ_1 . **Thus, the analytic model predicts that in the non-degenerate regime, the circuit stability is independent of the modulated capacitor's phase δ_1 .**

$$\begin{aligned} Re(Z_{in,\omega_0}) = & \frac{\epsilon_1^2 (-R_{int}) - \epsilon_1^2 R_{A1,l}}{4 \left(2C_0^2 R_{int} \omega_s^2 R_{A1,l} + C_0^2 \omega_s^4 L_{A1,l}^2 - 2C_0 \omega_s^2 L_{A1,l} + C_0^2 \omega_s^2 R_{A1,l}^2 + C_0^2 R_{int}^2 \omega_s^2 + 1 \right)} + \\ & \frac{3 (\epsilon_1^2 R_{A1,l} + \epsilon_1^2 R_{int})}{4 \left(18C_0^2 R_{int} \omega_s^2 R_{A1,l} + 81C_0^2 \omega_s^4 L_{A1,l}^2 - 18C_0 \omega_s^2 L_{A1,l} + 9C_0^2 \omega_s^2 R_{A1,l}^2 + 9C_0^2 R_{int}^2 \omega_s^2 + 1 \right)} \end{aligned} \quad (5.7)$$

$$Im(Z_{in,\omega_0}) = \frac{-2C_0\epsilon_1^2 R_{int}\omega_s R_{A1,l} - C_0\epsilon_1^2\omega_s^3 L_{A1,l}^2 - C_0\epsilon_1^2\omega_s R_{A1,l}^2 + \epsilon_1^2\omega_s L_{A1,l} - C_0\epsilon_1^2 R_{int}^2\omega_s}{4(2C_0^2 R_{int}\omega_s^2 R_{A1,l} + C_0^2\omega_s^4 L_{A1,l}^2 - 2C_0\omega_s^2 L_{A1,l} + C_0^2\omega_s^2 R_{A1,l}^2 + C_0^2 R_{int}^2\omega_s^2 + 1)} - \frac{9(2C_0\epsilon_1^2 R_{int}\omega_s R_{A1,l} + 9C_0\epsilon_1^2\omega_s^3 L_{A1,l}^2 + C_0\epsilon_1^2\omega_s R_{A1,l}^2 - \epsilon_1^2\omega_s L_{A1,l} + C_0\epsilon_1^2 R_{int}^2\omega_s)}{4(18C_0^2 R_{int}\omega_s^2 R_{A1,l} + 81C_0^2\omega_s^4 L_{A1,l}^2 - 18C_0\omega_s^2 L_{A1,l} + 9C_0^2\omega_s^2 R_{A1,l}^2 + 9C_0^2 R_{int}^2\omega_s^2 + 1)} \quad (5.8)$$

The analytically-predicted stable ($Re(Z_{in,\omega_0}) > 0$) and unstable ($Re(Z_{in,\omega_0}) \leq 0$) $\epsilon_1 - \omega_s$ regions are plotted in figure 5.4.

5.4.3 Numerically-predicted stability

In this section, we outline how stability is classified using in the numerical time-domain method.

The numerical time-domain method is used to study the stability of the degenerate regime, and to cross-verify the results of the analytic model in the non-degenerate regime. The current through the radiation resistance as a function of time, $I_A(t)$, is found using the time-domain simulation. The simulation runs for 30,000 source periods. The first 5,000 are considered transients; the remaining time is considered non-transient. If the amplitude of the current grows in the non-transient period, then the system is labelled unstable. To assess stability, we label the first half and second half of the non-transient period D_a and D_b , respectively. In each region D_a and D_b , we compute the maximum value of the current M_a and M_b respectively, given by:

$$M_i = \max_{t \in D_i} (|I(t)|), i \in [a, b] \quad (5.9)$$

This construction is illustrated in figure 5.3b. We pick a tolerance $a = 0.1$. If $M_b > (1 + a)M_a$, then the system has a growing current amplitude and is labelled unstable, else it is labelled stable. This method labels all stable systems as stable for $a > 0$, but will label weakly unstable systems, those that do not grow by more than $(1 + a)$ times from D_a to D_b , as stable. For more accurate classification of weakly unstable systems, a can be decreased.

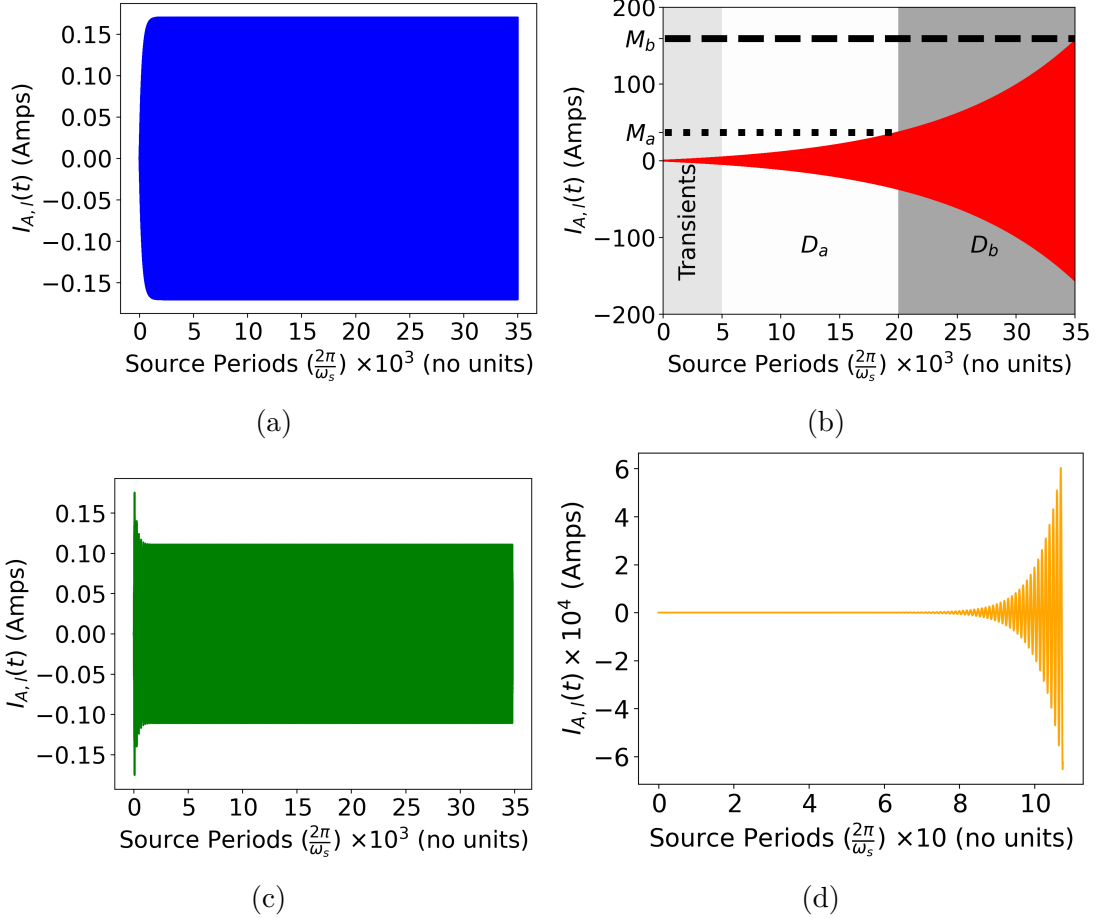


Figure 5.3: The current through the loop antenna radiation resistance $I_{A,l}(t)$ generated by the numerical time-domain simulation as a function of source periods. Plots ($\frac{\omega_s}{\omega_{op}} = 1, \epsilon_1 = 0.112$) (a), ($\frac{\omega_s}{\omega_{op}} = 1, \epsilon_1 = 0.11455$) (b), ($\frac{\omega_s}{\omega_{op}} = 1.005, \epsilon_1 = 0.112$) (c) and ($\frac{\omega_s}{\omega_{op}} = 0.93, \epsilon_1 = 0.22$) (d) are colour coded with points in figure 5.4.

5.4.4 Comparison of analytically and numerically-predicted instabilities

We have used two different models to detect stability in two different ways. Here, we compare them, and through this, obtain the boundary of stability for the loop antenna.

In figure 5.4, the regions of stability and instability predicted by the time-domain (stable black, unstable white points) and analytic (blue and white regions) methods are shown. The dynamics of the current through the antenna $I_{A,l}(t)$ for different modulation ϵ_1 and source-frequency ω_s combinations are shown in figure 5.3 and colour coded with figure 5.4. $\epsilon_1 - \omega_s$ points within the numerically predicted stable region (blue, green) show no non-transient exponential growth in antenna current $I_{A,l}(t)$, while the orange

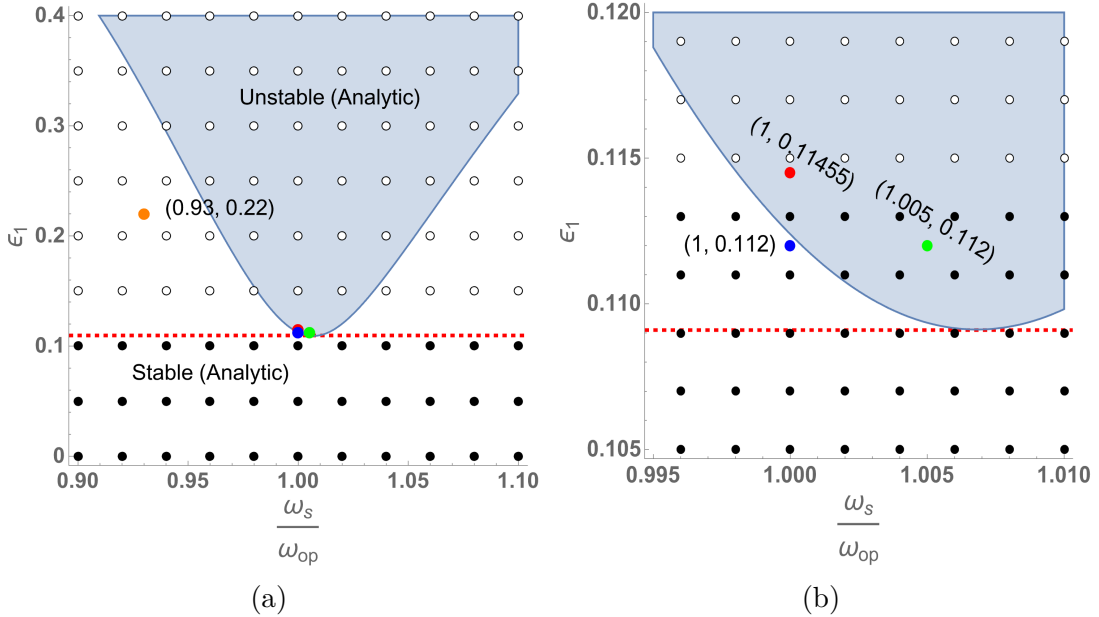


Figure 5.4: The analytically-predicted stable (white) and unstable (light blue) ($\frac{\omega_s}{\omega_{op}}, \epsilon_1$) space plots. The numerically-predicted stable (black) and unstable (white) points are shown. The numerical results for selected points (green, red, blue, orange) shown in figure 5.3. Figure (b) is a small, higher resolution section of figure (a). The red dashed line indicates the analytically-predicted stability threshold.

point in the numerically predicted unstable region does. **From this, we conclude the numerical stability detection method (Sec. 5.4.3) correctly classifies stability.** In the $\epsilon_1 \gtrsim 0.1$ region, the analytic and numerically predicted stability disagree - some numerically-predicted stable (black) points lie within the analytically-predicted unstable (blue) region and vice-versa. These discrepancies between the analytic and numerical model occur exclusively in the $\epsilon_1 \gtrsim 0.1$ region, where the analytic model was found to be inaccurate (see Sec. 4.7) due to truncation of higher frequency terms in equation 4.8.

Unlike the analytic model, the numerical method solves the ODEs to a fixed precision and accuracy (here 10 decimal places). With a precision or accuracy too small, the numerical ODE solver in Mathematica can give incorrect results. To check this, the numerical points in figure 5.4 were repeated with double the accuracy and precision - no changes in the results were found.

The main result of figure 5.4 is that the analytic and numerical models predict similar drivings $\epsilon_1 = 0.10964$ and $0.113 < \epsilon_1 \leq 0.11455$ respectively as the thresholds for instability for the loop antenna. **As these bounds are both in the $\epsilon_1 \gtrsim 0.1$ driving**

region, we use the more accurate numerical result $0.113 < \epsilon_1 \leq 0.11455$ as the threshold for instability.

5.5 Simultaneous maximisation of bandwidth and efficiency

With stability checked, we frequency-broaden the efficiency and then apply parametric amplification to increase the efficiency and bandwidth simultaneously.

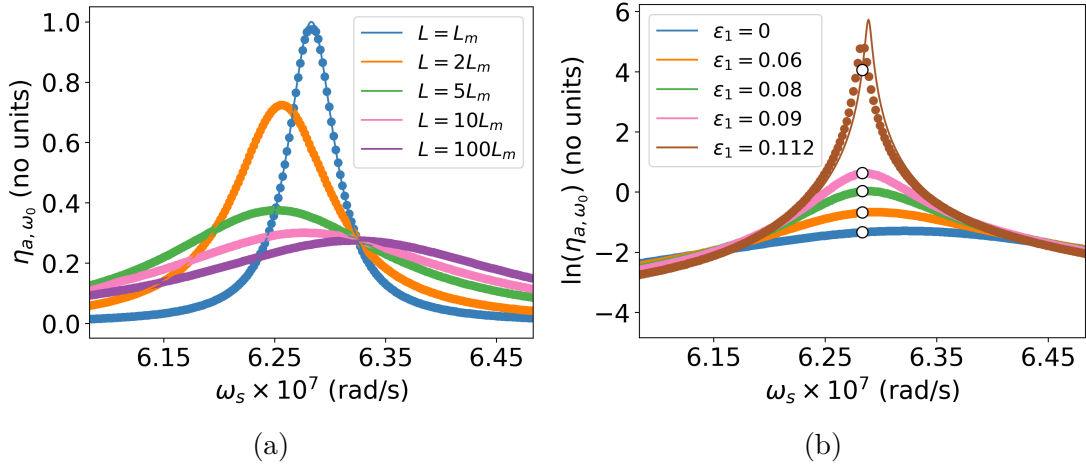


Figure 5.5: The efficiency of the carrier η_{a,ω_0} as a function of source frequency ω_s for the loop antenna with circuit in figure 4.2. Figure (a) shows efficiency broadening by increasing matching circuit inductance L (see Fig. 4.2) creating mismatch between the antenna and source. Figure (b) shows increasing parametric amplification driving ϵ_1 . Analytic (lines) and numerical (points) shown. The white points indicate the degenerate case, where the analytic model is invalid.

The generalised Wheeler-Chu limit bounds the bandwidth and efficiency. To improve the bandwidth and efficiency we follow the method of [19]. First, we trade efficiency for bandwidth by increasing the matching inductor L past its matched value, L_m , giving wider and shorter efficiency peaks - this is shown in figure 5.5a. Next, we take the broadest peak ($L = 100L_m$, purple) and apply parametric amplification by increasing parametric driving $\epsilon_1 > 0$; this is shown in figure 5.5b. We see that as driving ϵ_1 grows, the peak efficiency increases while maintaining approximately the same width. **By trading**

efficiency for bandwidth and then applying parametric amplification, we have simultaneously increased efficiency and bandwidth. Critically, in figure 5.5b, parametric driving ϵ_1 is below the threshold for instability ($0.113 < \epsilon_1 \leq 0.11455$) found in section 5.4.4. We additionally show in figure 5.3a that the maximum driving used, $\epsilon_1 = 0.112$ does not yield exponentially growing currents and so is stable.

The analytic (lines) and numerical (points) results in figure 5.5 agree for all but high driving $\epsilon_1 = 0.112$. This occurs in the $\epsilon_1 \gtrsim 0.1$ region where that analytic model is inaccurate (see Sec. 5.4.4). As such, we take the numerical result as correct.

5.5.1 Comparison to the Bode-Fano and Wheeler-Chu limits

Here we test if the increased efficiency and bandwidth derived through parametric amplification beats traditional LTIP techniques.

Given an efficiency tolerance $\eta_{a,\omega_0,T}$, the fractional bandwidth $B_f(\eta_{a,\omega_0,t})$ is the range of frequencies normalised by the central frequency for which the efficiency η_{a,ω_0} exceeds the tolerance $\eta_{a,\omega_0} \geq \eta_{a,\omega_0,T}$. Because of this, for a given efficiency curve $\eta_{a,\omega_0}(\omega_s)$, the fractional bandwidth $B_f(\eta_{a,\omega_0,T})$ changes with the choice of $\eta_{a,\omega_0,T}$. In figure 5.6, the bandwidth $B_f(\eta_{a,\omega_0,T})$ is plotted against the carrier efficiency tolerance $\eta_{a,\omega_0,T}$. The green and grey regions are the bandwidth-efficiency values permitted by the modified Bode-Fano (Eq. 3.2) and generalised Wheeler-Chu (Eq. 3.3) limits. If a point lies outside the green region, it violates the modified Bode-Fano limit (Eq. 3.2) and the matching network yields a higher bandwidth for a given efficiency than all LTIP non-dissipative matching networks with the loop antenna. If a point lies outside the grey region, then it violates the generalized Wheeler-Chu limit (Eq. 3.3) and has a higher bandwidth for a given efficiency than all LTIP antennas with any LTIP non-dissipative matching network.

The two matching networks without modulation (blue square and red circle) do not break passivity. Because of this, they obey the assumptions of the modified Bode-Fano (Eq. 3.2) and Wheeler-Chu (Eq. 3.3) limits and so lie within the green and grey regions. The loop with parametric amplification (brown triangles) breaks the assumption of passivity and lies outside the green and inside the grey regions. **Therefore, by introducing parametric amplification, we have broken the Bode-Fano limit (Eq. 3.2) but**

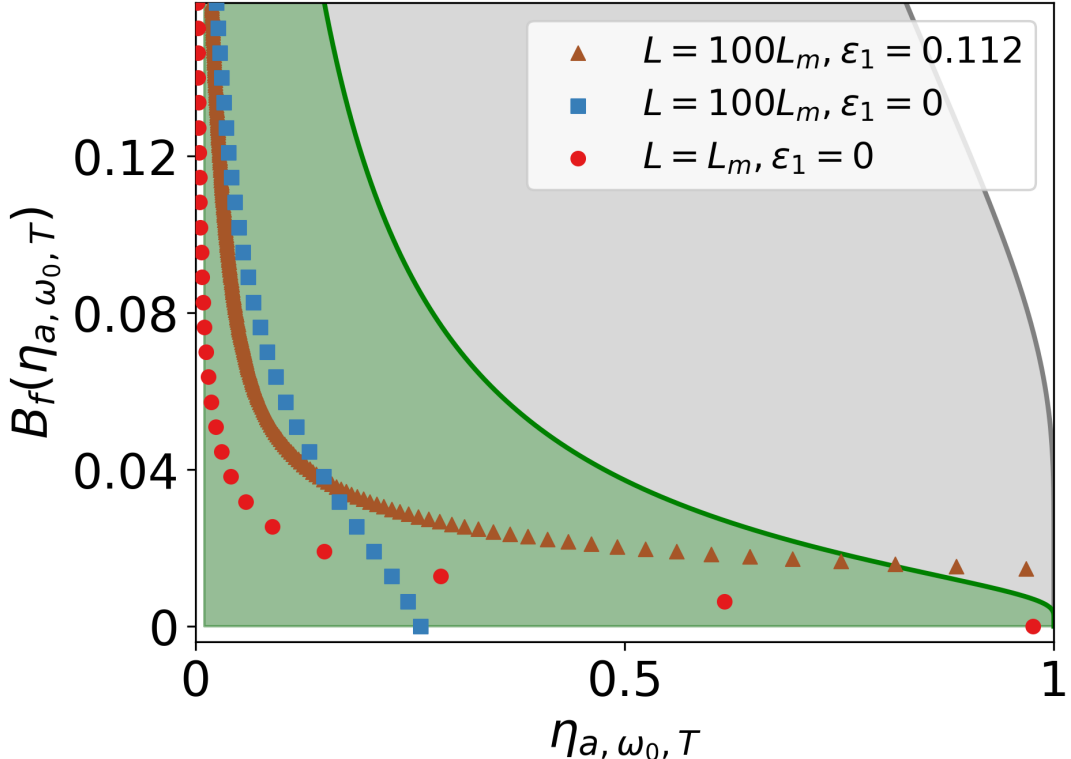


Figure 5.6: The bandwidth against efficiency tolerance for the loop antenna without (red circle, blue square) and with (brown triangle) capacitance modulation in the parametric amplification regime. Shaded regions are where bandwidth efficiency combinations are permitted by the generalised Wheeler-Chu limit (grey) and modified Bode-Fano limit (green). Results are produced by the modified time-domain numerical method.

not the generalised Wheeler-Chu limit (Eq. 3.3). Breaking the Bode-Fano limit does imply this method *can* break the generalised Wheeler-Chu limit (Eq. 3.2), as the Bode-Fano limit (Eq. 3.2) is used to derive the generalised Wheeler-Chu limit. We are not able to break the generalised Wheeler-Chu limit here because the quality factor of the loop antenna is $Q_{loop} \approx 243$, which is much larger than Chu's limiting value of $Q_{loop,Chu} \approx 22$ at the operational frequency. In future, antennas with quality factors close to the Chu limit (Eq. 2.12) such as fractal, metamaterial or wire cage antennas should be used [16] with this method to overcome the generalised Wheeler-Chu limit.

5.5.2 Dependence of bandwidth and efficiency capacitor modulation phase

Figure 5.5 excludes the degenerate case ($\omega_s = \omega_{op} = \frac{1}{2}\omega_c$) due to its dependence on the capacitor's modulation phase δ_1 . In figure, 5.7 we consider how the efficiency and bandwidth of the highest efficiency peak in figure 5.5b, ($L = 100L_m, \epsilon_1 = 0.112$, brown) depends on the capacitor's modulation phase.

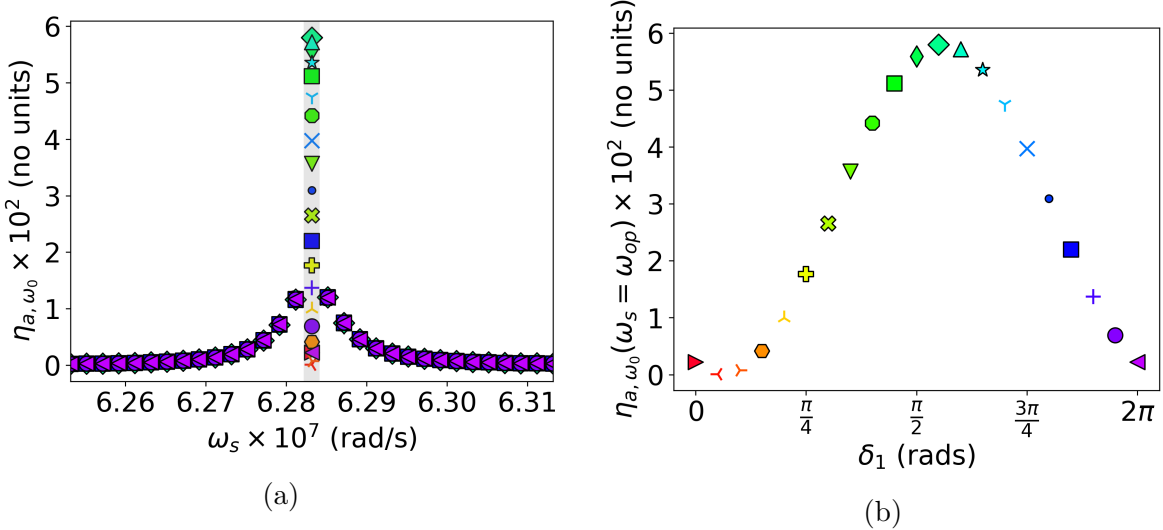


Figure 5.7: The effect of capacitor modulation phase δ_1 on the carrier efficiency η_{a,ω_0} as a function of source frequency ω_s for a loop antenna with circuit in figure 4.2 is shown. Points with different capacitor modulation phases δ_1 are shape and colour coded as shown in figure (b). Figure (a) shows η_{a,ω_0} vs ω_s data for different δ_1 in the degenerate (shaded) and non-degenerate (not shaded) case. Figure (b) shows how the efficiency in the degenerate case varies with δ_1 . All data is produced by the numerical method.

Figure 5.7a shows that in the non-degenerate amplification regime (not shaded), that the carrier efficiency η_{a,ω_0} has no dependence on the capacitor's modulation phase δ_1 , which agrees with the results of the analytic model in section 5.4.2. However, in figure 5.7b the efficiency in the degenerate case (shaded in figure 5.7a) is found to vary 2π -periodically with the capacitor's modulation phase. This agrees with other work [19, 51] and our simplified model (Sec. 5.2). Importantly, for capacitor phases $\delta_1 \in [0, \frac{\pi}{5}] \cup [\frac{9\pi}{10}, 2\pi]$, the efficiency of the degenerate point falls below that of its frequency-neighbours in figure 5.7a. In this capacitor modulation phase range, the bandwidth and efficiency of the antenna are decreased. At $\delta_1 \approx \frac{\pi}{20}$, the efficiency at the degenerate point is near zero,

making the bandwidth zero for any non-zero efficiency tolerance. This corresponds to the $\delta_1 = \pi$ case in the toy model (Sec. 5.2).

The degenerate point, and its associated efficiency-bandwidth dependence on the phase of the modulated capacitor occurs in an infinitesimal source-frequency range; exactly when the modulation frequency ω_c is twice the source frequency ω_s . In experiment and simulation on a similar parametrically amplified loop antenna, the effects of the degenerate point were not observed unless carefully selecting the source-frequency [19]. Because of this, we ignore the practical dependence on capacitor phase modulation here, like other authors [19, 20]. **This is the main result of this section - that in practice the loop antenna's efficiency and bandwidth does not depend on the modulation phase of the capacitor.**

Antenna Phase

To encode a phase into the transmitted signal, the phase of the source must change the phase of the radiated signal. Here, we test how the phase of the source changes the phase of the carrier and sidebands in the degenerate and non-degenerate case for the highest efficiency and broadest peak ($L = 100L_m$, $\epsilon_1 = 0.112$, brown) in figure 5.5b.

$$\phi_n = \text{Arg}(\tilde{I}_{a,l}^{(n)}) \quad (5.10)$$

The phase of the signal radiated by the antenna at a frequency ω_n , ϕ_n , is the phase of the current through the antenna $\tilde{I}_{a,l}^{(n)}$ at the frequency ω_n .

In figure 5.8, the analytic (lines) and numerical (points) antenna phases for carrier ϕ_0 (non-degenerate blue, degenerate

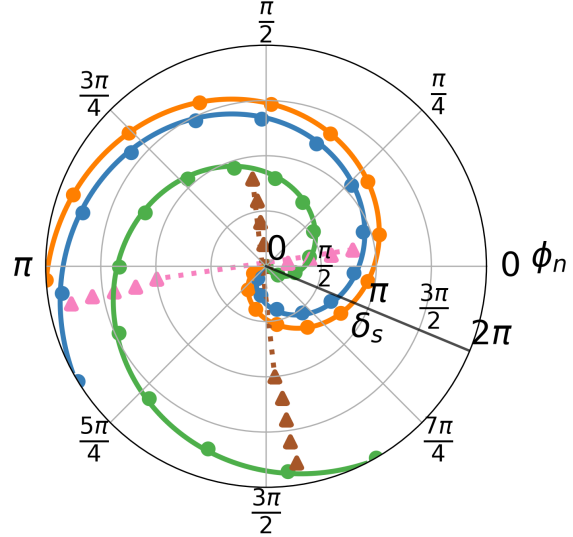


Figure 5.8: Phases ϕ_0 , ϕ_{-1} and ϕ_1 of the current through the loop (circuit in figure 4.2, $L = 100L_m$, $\epsilon_1 = 0.112$) antenna radiation resistance at carrier/sideband frequency ω_0 (blue), ω_{-1} (orange) and ω_1 (green) for degenerate case and ω_0 (pink) and ω_1 (brown) in the non-degenerate case. Figure shows how ϕ_n varies with the source phase δ_s . Analytic (lines) and numerical (points) are shown.

pink) and sidebands ϕ_{-1} (non-degenerate orange, degenerate brown) and ϕ_1 (non-degenerate green) are plotted against the phase of the source δ_s in the degenerate and non-degenerate case with a constant source frequency. In the non-degenerate case, the phase of the radiated carrier ϕ_0 (blue) and sidebands ϕ_{-1} (orange) and ϕ_1 (green) depend linearly on the source phase. Thus, by encoding information in the phase of the source, the information can be transmitted and received by the antenna at any of the carrier or sidebands. **So, in the non-degenerate case, the parametrically amplified loop antenna can be used to transmit phase-modulated communications.** This is not studied by other authors [19, 20].

In the degenerate case, the analytic model is invalid and only the numerical points for the phase of the carrier ϕ_0 (pink) and sideband ϕ_1 (brown) are shown in figure 5.8. Note that the sideband ω_{-1} is degenerate with the carrier ω_0 and so the phase of the sideband ϕ_{-1} is identical to the phase of the carrier ϕ_0 and is included in the carrier phase ϕ_0 . Unlike the non-degenerate case, the carrier ϕ_0 (pink) and sideband phases ϕ_1 (brown) do not depend linearly on the source phase δ_s . Instead, the carrier phase ϕ_0 is ≈ 0.16 rad/s for source phases $\delta_s \in [0, \frac{4\pi}{5}]$ and then discontinuously jumps to ≈ 3 rad/s for source phases $\delta_s \in [\pi, \frac{9\pi}{5}]$. A similar behaviour is observed in the phase of the sideband ϕ_1 . As the carrier and sideband phases ϕ_0 and ϕ_{-1} do not change smoothly with the source phase δ_s , they cannot be used to transmit high information rate phase-modulated signals. However, as discussed, this degenerate case occurs exactly when the frequency of capacitance modulation is double the source frequency and can be ignored in applications [19]. **In practice then, the parametrically amplified loop antenna can be used for phase-modulated communication, as changing the phase of the source linearly changes the phase of the sidebands and carrier..**

5.5.3 Relative Strength of the carrier and sidebands

In figure 5.9, the efficiency at the carrier ω_0 (blue) is compared with sidebands ω_{-1} (green) and ω_1 (orange). The power at the sideband ω_1 (green) is insignificant, being $e^7 - e^8$ times smaller than that of the carrier ω_0 (orange). This is expected as the sideband frequency is not near the resonant frequency $\omega_1 \not\approx \omega_{op}$ and so is not excited. However, the sideband ω_{-1} (orange) power is comparable to that of the carrier ω_0 . This is because the carrier ω_0 and sideband ω_{-1} are near resonance for the circuit and so are excited. In other simulation and experimental work with a similar parametrically amplified loop antenna, the power at sideband ω_{-1} was negligible relative to the power at the carrier ω_0 [19]. In [19], however, the variable capacitor is realised using a varactor diode with a frequency filter. This filter increases the impedance at the sidebands, decreasing the power radiated at the sideband ω_{-1} . Here, the idealised capacitor model does not include such filters, so we observe significant power radiated at sideband ω_{-1} . To model the varactor diode and the filters, the same numerical method with a modified set of current-voltage ODEs can be used.

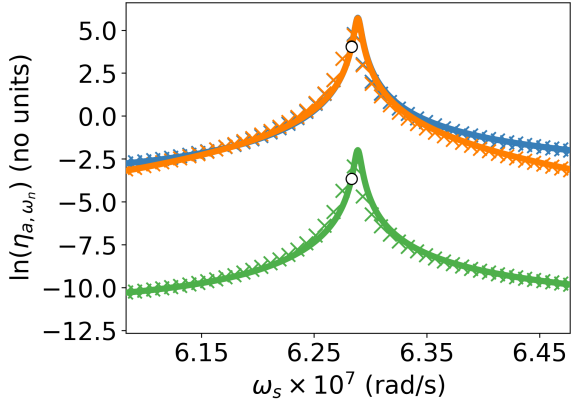


Figure 5.9: The relative strength of the carrier ω_0 (blue) and sidebands ω_{-1} (orange) and ω_1 (green) radiated for the loop antenna given by numeric (crosses) and analytic (lines) method. The white point is the degenerate case where the analytic model is invalid.

Figure 5.9 shows the relative strength of the carrier ω_0 (blue), sideband ω_1 (orange), and sideband ω_{-1} (green) radiated for the loop antenna. The y-axis is $\ln(\eta_a, \omega_n)$ (no units), ranging from -12.5 to 5.0. The x-axis is $\omega_s \times 10^7$ (rad/s), ranging from 6.15 to 6.45. The blue curve (carrier) has a peak around 6.3 rad/s. The orange curve (sideband ω_1) has a sharp peak at approximately 6.28 rad/s. The green curve (sideband ω_{-1}) has a deep minimum around 6.26 rad/s. Crosses represent numeric data, and solid lines represent analytic data. A white circle marks the degenerate case where the analytic model is invalid.

5.6 Extension to capacitive antennas

Here we extend capacitance modulation in the parametric amplification regime to capacitive antennas using the electrically small dipole antenna as an example. As the dipole antenna is capacitive, it uses the LC-bridge matching network with the variable capacitor $C(t)$ placed in parallel with the antenna (See Fig. 4.5). In the loop antenna, the variable capacitor was placed in parallel. In figure 5.10a, we follow the method for the loop antenna and decrease capacitance C_0 to mismatch the antenna, trading efficiency for bandwidth. In figure 5.10b, we take the broadest peak ($C_0 = 0.2C_m$) and apply

parametric amplification $\epsilon_1 > 0$. **Unlike the loop antenna, we observe no increase in efficiency.** This is the result of the variable capacitor $C(t)$ being placed in parallel with the antenna. When we broaden the efficiency curve by decreasing the capacitance C_0 , the impedance of the variable capacitor $C(t)$ approaches an open circuit, and so any modulation has little impact. Additionally, when parametric amplification is applied, the variable capacitor $C(t)$ introduces energy, giving it a negative resistance. When in parallel with the antenna, this causes all the current to flow through the variable capacitor rather than the antenna, yielding no increase in antenna efficiency - this is seen in figure 5.10b. To remedy this, other authors have modulated the inductance L in series

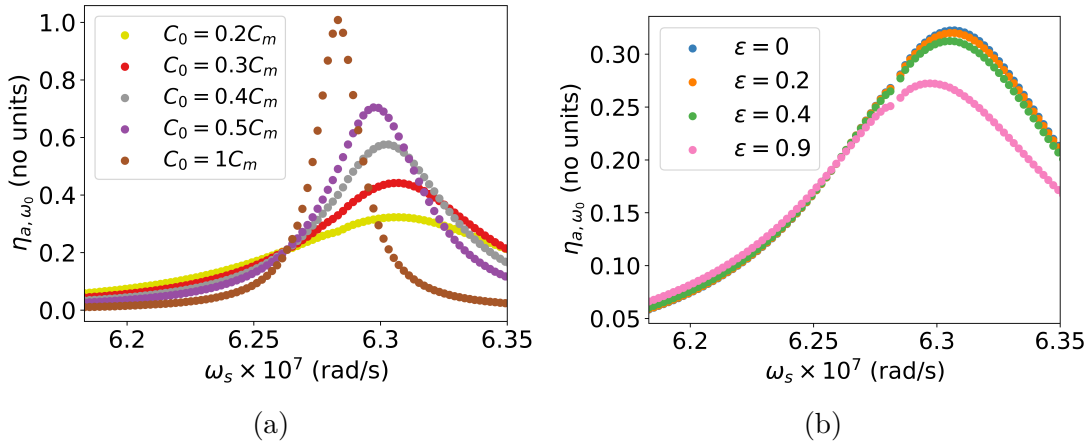


Figure 5.10: The efficiency of the carrier η_{a,ω_0} as a function of source frequency ω_s for the dipole antenna with circuit in figure 4.4. Figure (a) shows efficiency broadening using antenna mismatch. Figure (b) shows increasing parametric amplification driving ϵ_1 . Results produced by the time domain method.

with the dipole antenna [20]. However, this technique is frequency limited, as realisations of variable inductors are typically 10^3 times slower at modulation than varactor-diode-aided variable capacitors that we consider here [45]. Alternatively, a large inductor can be placed in series with the antenna, making the antenna inductive and allowing it to be treated similar to the loop. Physical realisations of such inductors incur significant parasitic losses and thus decrease η_b of the circuit. For antennas with power sources constrained primarily by total energy available - like portable devices, this is suboptimal [26, 27].

5.7 Dipole with variable capacitor

We remind ourselves of the dipole with variable capacitor antenna from chapter 4. We then perform a similar analysis to the loop using the numerical method.

Here, we consider a novel method where the impedance of the dipole antenna is modulated directly - as opposed to its matching network. To do this, a variable capacitor $C_{A3,dv}(t)$ is placed across the feed of the antenna (Fig. 2.4 (right)) and a static capacitor C_0 is used for matching. The circuit for this antenna is shown in figure 4.5 and the variable capacitor $C_{A3,dv}(t)$ is given the form

$$C_{A3,dv}(t) = C_{A30,dv}(1 + \epsilon_1 \sin(\omega_c t + \delta_1)), \quad (5.11)$$

where $C_{A30,dv}$ is the static capacitance which we set to $C_{A1,dv}$ and other parameters are similar to equation 5.5. We now follow a similar process to the parametrically amplified loop antenna to achieve superior efficiency-bandwidth performance.

5.7.1 Simultaneous maximisation of bandwidth and efficiency

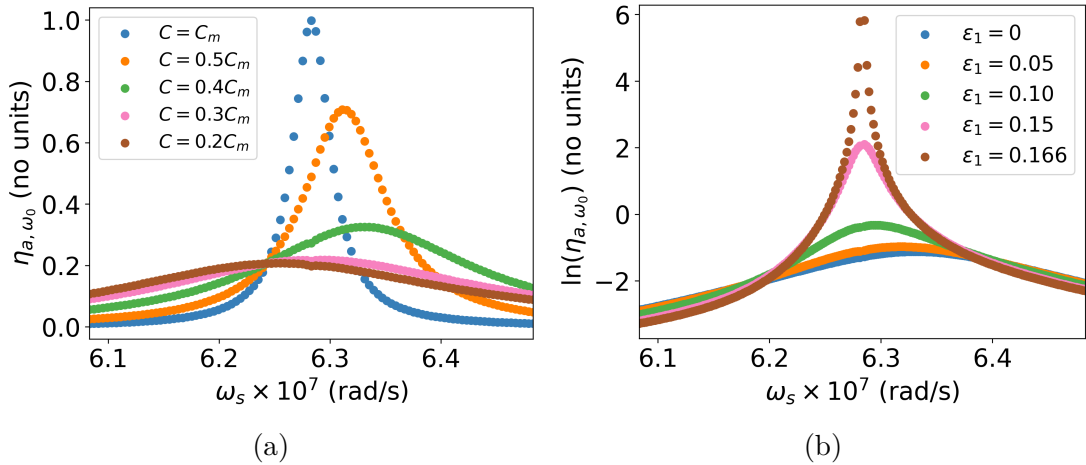


Figure 5.11: The efficiency of the carrier η_{a,ω_0} as a function of source frequency ω_s for the dipole antenna with capacitor (circuit in Fig. 4.5). Figure (a) shows broadening using antenna mismatch. Figure (b) shows increasing parametric amplification driving ϵ_1 . Data produced by the time-domain numerical method.

Like the loop antenna, we trade efficiency for bandwidth in figure 5.11a by decreasing the matching capacitance C_0 from its matched value C_m . **Then, by increasing driving**

$(\epsilon_1 > 0)$, parametric amplification increases the efficiency without dramatically changing bandwidth. This is distinct from the dipole antenna case, where no amplification was observed as the variable capacitor was in parallel with the antenna. The bandwidth and efficiency of the dipole with capacitor antenna is compared with the

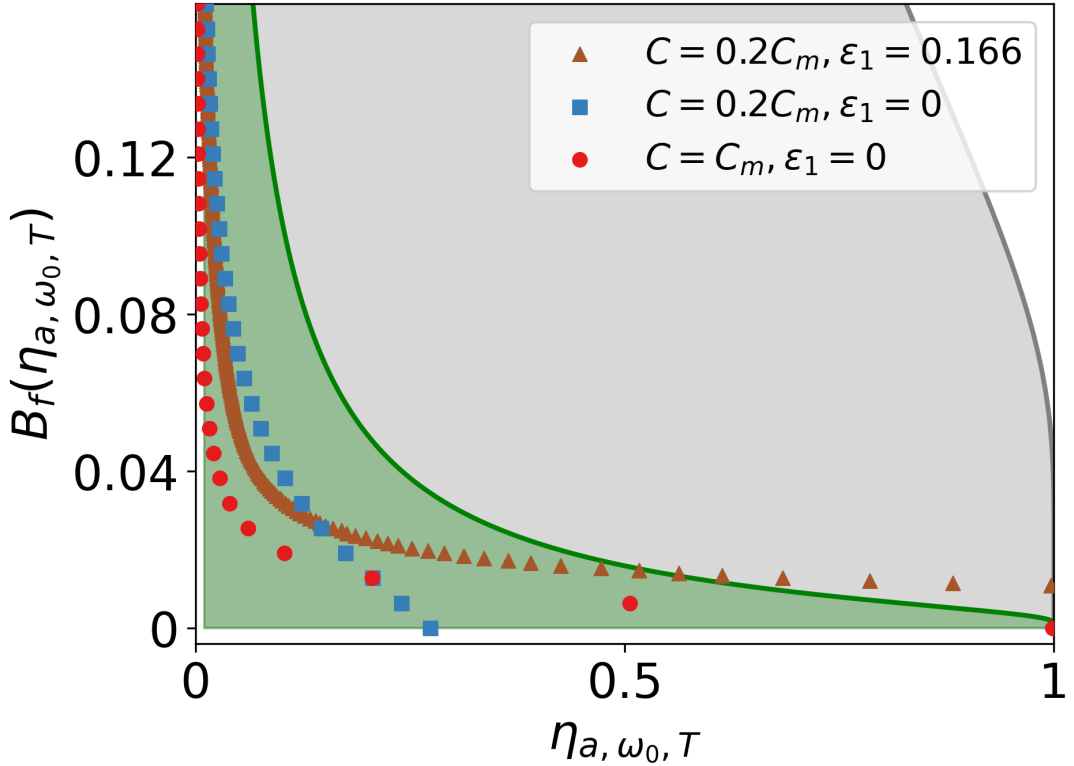


Figure 5.12: The bandwidth against efficiency tolerance for the dipole with capacitor antenna without (red circle, blue square) and with (brown triangle) capacitance modulation in the parametric amplification regime. Shaded regions are where bandwidth efficiency combinations are permitted by the generalised Wheeler-Chu limit (grey) and modified Bode-Fano limit (green). Results are produced by the time-domain numerical method.

modified Bode-Fano (green) and generalised Wheeler-Chu (grey) limits in figure 5.12. The results are similar to the loop antenna. The antenna-matching-networks that do not break passivity (red circle, blue square) have bandwidth and efficiency bounded by the modified Bode-Fano (green) and generalised Wheeler-Chu (grey) limits. The parametrically amplified dipole with capacitor antenna (brown triangle) surpasses the modified Bode-Fano limit, but not the Wheeler-Chu limit. Thus, the dipole with capacitor antenna has superior bandwidth and efficiency to a similar dipole antenna with any LTIP non-dissipative matching circuit. However, there may exist an

LTIP antenna with an LTIP non-dissipative matching network with a superior bandwidth and efficiency.

5.7.2 Dependence on the capacitor's modulation phase and source phase

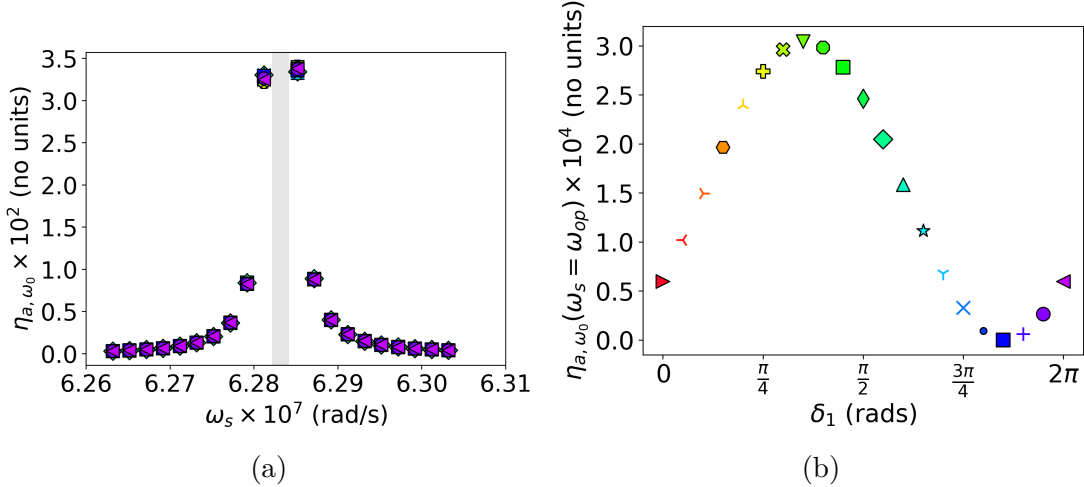


Figure 5.13: The effect of capacitance modulation phase δ_1 on the carrier efficiency η_{a,ω_0} as a function of source frequency ω_s for the dipole with capacitor antenna (circuit in Fig. 4.5). Points with different capacitance modulation phase δ_1 are shape and colour coded as shown in figure (b). Figure (a) shows η_{a,ω_0} vs ω_s data for different δ_1 in the degenerate (shaded) and non-degenerate (not shaded) case. Figure (b) shows how the efficiency in the degenerate case varies with δ_1 . All data is produced by the numerical method.

We take the highest efficiency and bandwidth peak ($C = 0.2C_m, \epsilon_1 = 0.166$, brown) in figure 5.11b and vary the capacitor's modulation phase δ_1 in figure 5.13. Like the loop antenna (Fig. 5.7), the non-degenerate amplification regime (Fig. 5.13a) shows no dependence on the capacitor's modulation phase, and the degenerate regime (Fig. 5.13b) shows a 2π -periodic dependence on the capacitance modulation phase. The increase in efficiency between the degenerate and non-degenerate regimes is $\approx 10^2$ times; while in the loop, this of order ≈ 1 times. In some medical ESA applications, the energy output must not exceed a threshold [53]. For the dipole with capacitor, complying with this threshold may involve decreasing its efficiency-performance. As in the loop, the degenerate case is ignored. **Thus, the dipole with capacitor antenna has efficiency and bandwidth independent of the phase of the capacitors modulation.**

In the non-degenerate regime, figure 5.14 shows that the phase of the radiated carrier ϕ_0 (blue) and sidebands ϕ_{-1} (orange) and ϕ_1 (green) depend linearly on the phase of the source δ_s . Thus, in the degenerate regime, information encoded in the phase of the source can be transmitted by the dipole with capacitor antenna. In the degenerate case, the phase of the radiated carrier ϕ_0 (pink) and sideband ϕ_1 (brown) do not depend linearly on the source phase δ_s . Rather, the phase of the radiated carrier ϕ_0 and sideband ϕ_1 take only two values, and change discontinuously between them (indicated by dashed lines in Fig. 5.14) at a source phase of $\delta_s \approx \frac{12\pi}{30}$. This is similar to the loop (Fig. 5.8). Again, as the degenerate point and its effects can be ignored in practice, **the dipole with capacitor antenna can be used for phase-modulated communication.**

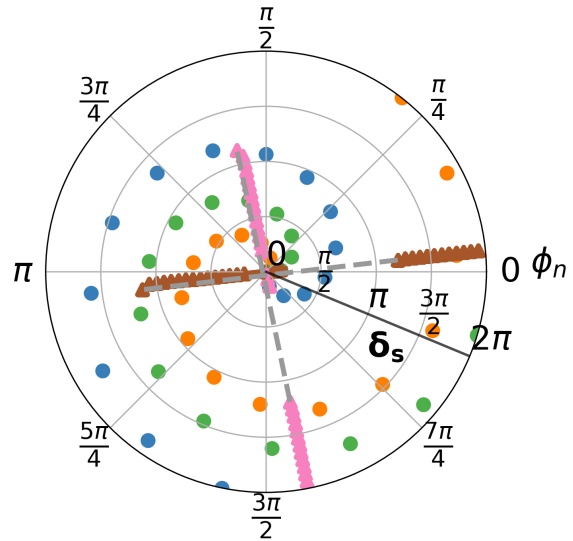


Figure 5.14: Phases of the carrier ϕ_0 (non-degenerate blue, degenerate pink) and sidebands ϕ_{-1} (non-degenerate orange) and ϕ_1 (non-degenerate green, degenerate pink) radiated by the dipole with capacitor antenna (circuit in Fig. 4.5, $C = 0.2C_m$, $\epsilon_1 = 0.166$) as a function of source phase δ_s .

5.7.3 Relative strength of the carrier and sidebands

The relative strength of the carrier and sidebands in the dipole antenna with capacitor is similar to the loop antenna, with the sidebands ω_{-1} (orange) and ω_1 (green) being significant and insignificant relative to the carrier ω_0 because they are in and outside the resonance frequency ω_{op} .

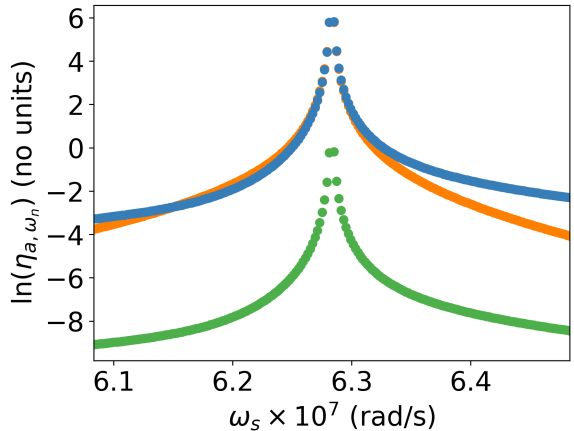


Figure 5.15: The relative strength of the carrier ω_0 (blue) and sidebands ω_{-1} (orange) and ω_1 (green) radiated for dipole antenna with capacitor across its feed given by numeric (crosses) and analytic (lines) method. The white point is the degenerate case where the analytic model is invalid.

5.8 Chapter Conclusion

In this chapter, we broke the condition of passivity in the generalised Wheeler-Chu limit (Eq. 3.3) in the loop, dipole, and dipole with capacitor antennas. We introduced parametric amplification by modulating a variable capacitor at approximately twice the antenna's source frequency, and through a toy model described how this introduces energy into the system and breaks passivity. To model this new modulation regime, we used the analytic method and modified the numerical method devised in chapter 4.

Using the electrically small loop antenna, we applied the analytic and numerical methods to study the system's stability, and gave a bound for the onset of instability within the system. Within the stable regime, we varied the loop antenna's matching network and imparted parametric amplification to simultaneously increase its efficiency and bandwidth. This work followed closely with [19]. Through comparison to the generalised Wheeler-Chu and modified Bode-Fano limits, the parametrically amplified electrically small loop antenna was found to have superior efficiency-bandwidth compared to all sim-

ilar traditional loop antennas; although, there may exist traditional ESAs that exceed its efficiency-bandwidth performance. If this technique is applied to an ESA of quality factor close to Chu's limit (Eq. 2.12) it will surpass the generalised Wheeler-Chu limit and have superior range and information rate compared to all traditional ESA.

Next, we studied how the phase of the capacitor's modulation effects the efficiency and bandwidth. We found that the efficiency and bandwidth depends on the phase of capacitance modulation for a single source-frequency. As such, we argued, similar to other authors [19], that for practical applications, the efficiency-bandwidth performance has no capacitor-modulation-phase-dependence. Next, we showed that changing the phase of the source does change the phase of the radiated signal and so the loop antenna can be used for phase-modulated communication; this was not studied previously by other authors.

In the degenerate case, we additionally found that phase of the radiation can only occupy two values and exhibits a source-phase discontinuity between them not studied by other authors [19, 20]. This degenerate case is of little practical importance however. Finally, we generalised the parametric amplification technique using a variable capacitor to the dipole antenna which is new. The resulting antenna showed a similar set of properties to the loop antenna. By extending this parametric amplification technique to the dipole, we showed that this technique can be applied to all ESAs. **Therefore, by introducing parametric amplification directly into a matching network or antenna, the bandwidth-efficiency limitations on LTIP ESAs connected to LTIP non-dissipative matching networks can be overcome.**

Thesis Conclusion

6.0.1 Conclusion

In this thesis, we studied surpassing fundamental and practically important limits on the efficiency and bandwidth of traditional Linear, Time-Invariant and passive (LTIP) electrically small antennas (ESAs) by breaking the LTIP conditions.

In the background chapter, we defined fundamental properties of antennas such as efficiency, bandwidth and quality factor and related them to practically important quantities such as antenna range and information rate. Through the early work of Wheeler [4], Chu [5], Bode [6] and Fano [7] on ESAs and matching, we discussed the fundamental bounds and ESAs, culminating in the Wheeler-Chu limit. The Wheeler-Chu limit says that an ESA can either have high efficiency (range) or high bandwidth (information rate); not both, and both are desirable. Then, we considered how ESAs are modelled using lumped element models and Kirchoff's laws. Within this framework, we discussed methods of realising and modelling variable capacitors and discussed how such devices can be used to break the conditions of time-invariance and passivity in an ESA to overcome the Wheeler-Chu limit.

In chapter 3, we developed a general bound between the bandwidth, efficiency and size for ESAs. We showed that this limit agrees with others and used it throughout chapter 5 to check if the techniques developed surpass the efficiency-bandwidth performance of **all** traditional ESAs.

In chapter 4, we broke the condition of time-invariance in the Wheeler-Chu limit by placing a modulated variable capacitor either within an ESA or its matching network. We applied this to loop and dipole ESAs, covering the two classes of ESA - capacitive and inductive. We then considered the case of *slow modulation* in which the variable capacitor

was modulated at well below the frequency of the antennas source. By developing a simplified frequency-domain analytic method and a more general time-domain method, we studied the effect of modulation and verified the time-domain numerical method. Using the numerical method and Bayesian optimisation, we maximised the efficiency-bandwidth of the loop and dipole antennas with respect to time-dependence. **We found no improvement to performance in the case of slow modulation - this was the main result of this chapter.**

In chapter 5, we broke the condition of passivity in the Wheeler-Chu limit. To do this, we used parametric amplification using a variable capacitor modulated at twice the antenna's source frequency. Following Mekway and Li [19], we applied this method to a loop antenna by placing the modulated capacitor in a matching network. We varied the matching network away from its optimal values and modulated the variable capacitor, giving the loop antenna simultaneously high efficiency and bandwidth. Through comparison to limits derived in chapter 3, we showed that the modulated matching circuit has superior efficiency-bandwidth performance to all traditional matching networks with a similar loop antenna - this has been claimed by others [19], but not shown directly. **As such, this technique can be used to overcome the Wheeler-Chu limit for inductive ESAs.** We additionally studied the systems stability, dependence on the phase of the capacitor's modulation and relation between radiated phase and source phase. These results showed the loop antenna can transmit phase-modulated information, and requires no synchronisation of the modulated capacitor with the signal the antenna is transmitting - the former was not studied by other authors [19]. Next, we extended this method to capacitive antennas. In the past, this has been achieved with variable inductors which are frequency limited [20, 45] - here we use a varactor-diode-aided variable capacitor which is capable of modulation at radio frequencies [19]. We showed similar to the loop antenna, that for capacitive antennas that this method can overcome the Wheeler-Chu limit, can be used to transmit a phase-modulated signal and does not require synchronisation between the variable capacitor's modulation and the source. **In summary then, in chapter 5, we extended the work of Mekway and Li [19, 20] to produce practical capacitive and inductive ESAs capable of bandwidth-efficiency performance outside of what is traditionally possible.**

6.0.2 Future work and Limitations

Throughout this thesis we focused on developing new methods for surpassing the limits on efficiency and bandwidth of traditional Linear, Time-Invariant and Passive (LTIP) Electrically Small Antennas (ESAs) through breaking assumptions in the Wheeler-Chu limit. However, as discussed throughout the thesis, there are several techniques for breaking such LTIP conditions, including a vast array of antenna keying techniques [3, 26, 27, 48, 54–57] and methods using negative impedance converters [18, 58]. Each of these techniques have their limitations due to noise, restrictions on current or voltage, stability, type of antenna used and requirements on prior knowledge of the signal. Nevertheless, a direct comparison between the performance of these techniques and those developed in chapter 5 would be useful - however, it is outside of the scope of this thesis.

Several assumptions in this thesis are also *highly* ideal. First, the assumption of an ideal variable capacitor is unrealistic. In reality, such variable capacitors will have non-linearity [46], which, as discussed, may explain the discrepancy in results between the work in chapter 4 and the work of [23]. Extensions to these non-ideal variable capacitor models are covered in section 2.5.2 and can be easily simulated by inputting the corresponding Kirchoff's laws into the numerical simulation. Second, we have ignored all losses in the antenna that are not radiation [1]. These can be modelled as an additional resistor in the lumped element antenna models. Lastly, in chapter 5 when we broke passivity, we did not include the additional energy provided to the circuit through the modulated capacitor in our calculations of efficiency. To account for this, we can define a new efficiency η_c , and compute the power introduced through modulation using equation 2.1.

Appendix

A.1 Source voltage used for time-domain method

$$V(t) = V_0 H\left(t - \frac{10\pi}{\omega_s}\right) \tanh\left(\frac{\omega_s}{10\pi}t - 1\right) \sin(\omega_s t) \quad (\text{A.1})$$

Here, $H(x)$ is the unit step function given by:

$$H(x) = \begin{cases} 0 & \text{if } x < 0 \\ 1 & \text{else} \end{cases} \quad (\text{A.2})$$

, $\tanh(x)$ is the hyperbolic tangent function, V_0 is the voltage source amplitude, t is time and ω_s is the frequency of the voltage source in rad/s. A plot showing $V(t)$'s behaviour is shown in figure A.1

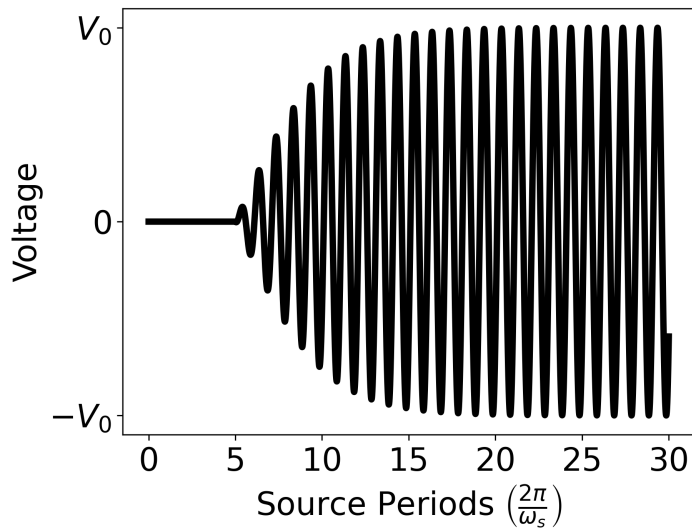


Figure A.1: Plot showing early voltage source dynamics. Voltage source given in equation A.1

A.2 The operator D in equation 4.13

$$\tilde{D} = \begin{pmatrix} i\omega_0 & 0 & 0 \\ 0 & i\omega_{-1} & 0 \\ 0 & 0 & i\omega_1 \end{pmatrix} \quad (\text{A.3})$$

Here, ω_0 and $\omega_{\pm 1}$ are the frequencies of the carrier and sidebands.

A.3 Dipole Antenna model values

Values for components in dipole antenna model used in figures 4.4 and 4.5 are given below.

$$C_{A1,d} = \frac{12.0674h}{\log\left(\frac{2h}{a}\right) - 0.7245} \times 10^{-12} \text{ Farads} \quad (\text{A.4})$$

$$C_{A2,d} = 2h \left(\frac{0.89075}{\left(\log\left(\frac{2h}{a}\right)\right)^{0.8006} - 0.861} - 0.02541 \right) \times 10^{-12} \text{ Farads} \quad (\text{A.5})$$

$$L_{A1,d} = 0.2h \left(\left(1.4813 \log\left(\frac{2h}{a}\right) \right)^{1.012} - 0.6188 \right) \times 10^{-12} \text{ Henries} \quad (\text{A.6})$$

$$R_{A1,d} = \left(0.41288 \left(\log\left(\frac{2h}{a}\right) \right)^2 + 7.40754 \left(\frac{2h}{a} \right)^{-0.02389} - 7.27408 \right) \times 10^3 \text{ Ohms} \quad (\text{A.7})$$

Here a is the wire radius of the antenna and h is the dipole antenna half-length. Equations are from [38].

A.4 Optimisation Bounds

$$\begin{aligned}
L &\in [2.65305 \times 10^{-5}, 2.70664 \times 10^{-5}] \text{ Henries}, \\
C_0 &\in [5.10645 \times 10^{-10}, 2.04258 \times 10^{-9}] \text{ Farads}, \\
\delta_1 &= 0 \text{ rads}, \\
\delta_2 &= [0, 2\pi] \text{ rads}, \\
\epsilon_1 &= [0, 0.80], \\
\epsilon_2 &= [0, 0.80], \\
\omega_c &\in [100000.0, 500000.0] \text{ rads/second}
\end{aligned} \tag{A.8}$$

$$\begin{aligned}
L &\in [9.39575 \times 10^{-8}, 5 \times 10^{-7}] \text{ Henries} \\
C_0 &\in [1.53078 \times 10^{-11}, 1.69192 \times 10^{-11}] \text{ Farads} \\
\delta_1 &= 0 \text{ rads}, \\
\delta_2 &= [0, 2\pi] \text{ rads}, \\
\epsilon_1 &\in [0, 0.02] \\
\epsilon_2 &\in [0, 0.02] \\
\omega_c &\in [100000.0, 500000.0] \text{ rads/second}
\end{aligned} \tag{A.9}$$

$$\begin{aligned}
L &\in [1.24903 \times 10^{-5}, 1.30001 \times 10^{-5}] \text{ Henries} \\
C_0 &\in [6.38306 \times 10^{-10}, 2.55322 \times 10^{-9}] \text{ Farads} \\
\delta_1 &= 0 \text{ rads}, \\
\delta_2 &= [0, 2\pi] \text{ rads}, \\
\epsilon_1 &\in [0, 0.05] \\
\epsilon_2 &\in [0, 0.05] \\
\omega_c &\in [100000.0, 500000.0] \text{ rads/second}
\end{aligned} \tag{A.10}$$

A.5 Test scoring function used for peak maximisation

$$s = \eta_{a,\omega_0}(\omega_s = \omega_{op}) \tag{A.11}$$

A.6 ODEs used for time-domain simulations of loop, dipole and dipole with varactor antenna

The following ODEs are for the loop A.12, dipole A.13 and dipole with varactor A.14 in figures 4.4, 4.2 and 4.5 respectively. The ODEs are derived from kirchoff's laws (see Sec. 2.4) using Mathematica's Eliminate function.

$$\begin{aligned} I'_{L,l}(t) &= \frac{V(t, \omega_s) - R_{int}I_{A,l}(t) - R_{int}I_{L,l}(t)}{L}, \\ V'_{C,l}(t) &= \frac{I_{A,l}(t) - C'(t)V_{C,l}(t)}{C(t)}, \\ I'_{A,l}(t) &= \frac{V(t, \omega_s) - R_{A1,l}I_{A,l}(t) - R_{int}I_{A1,l}(t) - V_{C,l}(t) - R_{int}I_{L,l}(t)}{L_{A1,l}}, \end{aligned} \quad (\text{A.12})$$

$$\begin{aligned} V'_{AP,d}(t) &= \frac{I_{A,d}(t)R_{A1,d} - R_{A1,d}I_{LA1,d}(t) - V_{AP,d}(t)}{R_{A1,d}C_{A2,d}}, \\ V'_{C,d}(t) &= \frac{-R_{int}V_{C,d}(t)C'(t) + V(t, \omega_s) - I_{A,d}(t)R_{int} - V_{C,d}(t)}{R_{int}C(t)}, \\ I'_{A,d}(t) &= \frac{-V_{AP,d}(t) + V_{C,d}(t) - V_{CA1,d}(t)}{L}, \\ I'_{LA1,d}(t) &= \frac{V_{AP,d}(t)}{L_{A1,d}}, \\ V'_{CA1,d}(t) &= \frac{I_{A,d}(t)}{C_{A1,d}} \end{aligned} \quad (\text{A.13})$$

$$\begin{aligned} V'_{AP,dv}(t) &= \frac{R_{A1,dv}I_{A,dv}(t) - V_{AP,dv}(t)}{C_{A2,dv}}, \\ I'_{A,dv}(t) &= \frac{-V_{AP,dv}(t) + V_{C,dv}(t) - V_{CA1,dv}(t)}{L}, \\ V'_{C,dv}(t) &= \frac{-R_{int}I_{A,dv}(t) + V(t, \omega_s) - V_{C,dv}(t)}{R_{int}C_{dv}}, \\ I'_{LA1,dv}(t) &= \frac{V_{AP,dv}(t)}{L_{A1,dv}}, \\ V'_{CA1,dv}(t) &= \frac{I_{A,dv}(t) - V_{CA1,dv}(t)C'_{A3,dv}(t)}{C_{A1,dv} + C_{A3,dv}(t)} \end{aligned} \quad (\text{A.14})$$

A.7 Square Wave function

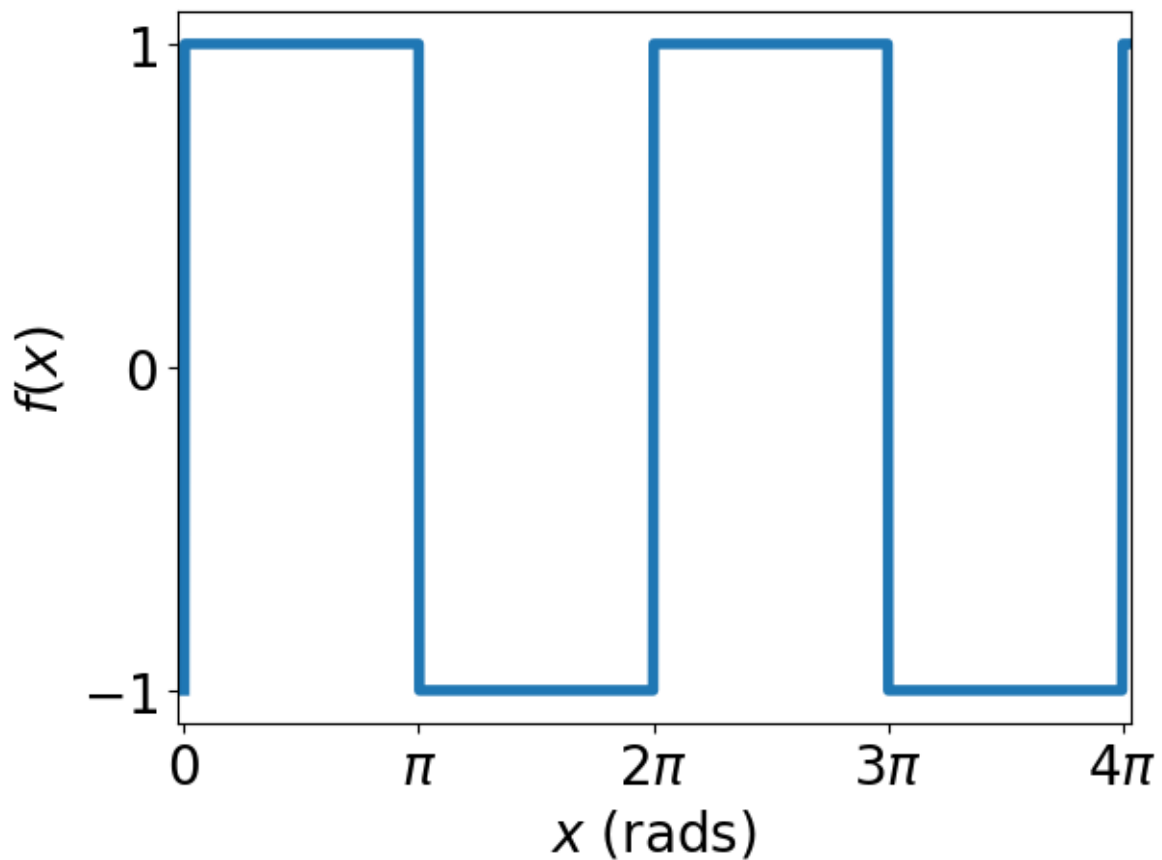


Figure A.2: Square wave function $f(x)$ with period 2π and amplitude 1.

Bibliography

- [1] Y. Huang. *Antennas: from theory to practice*. John Wiley & Sons, 2021.
- [2] C. G. Christodoulou and P. F. Wahid. “Fundamentals of antennas: concepts and applications”. 2001.
- [3] M. Manteghi. “Fundamental Limits, Bandwidth, and Information Rate of Electrically Small Antennas: Increasing the Throughput of an Antenna Without Violating the Thermodynamic Q-Factor”. *IEEE Antennas and Propagation Magazine*, 61(3):14–26, 2019.
- [4] H. A. Wheeler. “Fundamental limitations of small antennas”. *Proceedings of the IRE*, 35:1479–1484, 1947.
- [5] L. J. Chu. “Physical limitations of omni-directional antennas”. *Journal of applied physics*, 19(12):1163–1175, 1948.
- [6] H. Bode. *Network Analysis And Feedback Amplifier Design*. 1945.
- [7] R. Fano. “Theoretical limitations on the broadband matching of arbitrary impedances”. *Journal of the Franklin Institute*, 249(1):57–83, 1950.
- [8] R. E. Collin and S. Rothschild. “Evaluation of Antenna Q”. *IEEE Transactions on Antennas and Propagation*, 12:23–27, 1964.
- [9] R. C. Hansen. “Fundamental Limitations in Antennas”. *Proceedings of the IEEE*, 69:170–182, 1981.
- [10] J. S. Mclean. “A Re-Examination of the Fundamental Limits on the Radiation Q of Electrically Small Antennas”, 1996.
- [11] G. A. Vandenbosch. “Reactive energies, impedance, and Q factor of radiating structures”. *IEEE Transactions on Antennas and Propagation*, 58:1112–1127, 4 2010.

- [12] W. Geyi. “A method for the evaluation of small antenna Q”. *IEEE Transactions on Antennas and Propagation*, 51:2124–2129, 8 2003.
- [13] R. C. Hansen and R. E. Collin. “A new chu formula for Q”. *IEEE Antennas and Propagation Magazine*, 51:38–41, 10 2009.
- [14] R. L. Fante. “Quality Factor of General Ideal Antennas”. *IEEE Transactions on Antennas and Propagation*, 17:151–155, 1969.
- [15] A. Yaghjian and S. Best. “Impedance, bandwidth, and Q of antennas”. *IEEE Transactions on Antennas and Propagation*, 53(4):1298–1324, 2005.
- [16] D. F. Sievenpiper *et al.* “Experimental validation of performance limits and design guidelines for small antennas”. *IEEE Transactions on Antennas and Propagation*, 60:8–19, 1 2012.
- [17] M. Jacob and H. Brauch. “Keying VLF transmitters at high speed”. *Electronics*, 27(12):148–151, 1954.
- [18] S. E. Sussman-Fort and R. M. Rudish. “Non-Foster impedance matching of electrically-small antennas”. *IEEE Transactions on Antennas and Propagation*, 57(8):2230–2241, 2009.
- [19] A. Mekawy *et al.* “Parametric Enhancement of Radiation from Electrically Small Antennas”. *Physical Review Applied*, 15, 5 2021.
- [20] H. Li *et al.* “Beyond Chu’s Limit with Floquet Impedance Matching”. *Physical Review Letters*, 123, 10 2019.
- [21] P. Loghmannia and M. Manteghi. “Broadband Parametric Impedance Matching for Small Antennas Using the Bode-Fano Limit: Improving on Chu’s Limit for Loaded Small Antennas”. *IEEE Antennas and Propagation Magazine*, 2021.
- [22] M. Manteghi. “Antenna miniaturization beyond the fundamental limits using impedance modulation”. 2009.
- [23] M. Liu. private communication.

- [24] B. Shahriari *et al.* “Taking the human out of the loop: A review of Bayesian optimization”. *Proceedings of the IEEE*, 104(1):148–175, 2015.
- [25] C. Alexander and M. Sadiku. *Fundamentals of Electric Circuits*. 2003.
- [26] J. T. Merenda. “Digital Wideband Small Antenna Systems”, 2006.
- [27] J. T. Merenda. “Waveform-synthesis method that reduces battery power in an electrically small wideband radiating system”. *IET Microwaves, Antennas and Propagation*, 2:59–65, 2008.
- [28] A. Zangwill. *Modern electrodynamics*. Cambridge University Press, 2013.
- [29] H. Nyquist. “Certain factors affecting telegraph speed”. *Transactions of the American Institute of Electrical Engineers*, 43:412–422, 1924.
- [30] C. E. Shannon. “A mathematical theory of communication”. *The Bell system technical journal*, 27(3):379–423, 1948.
- [31] A. Bakshi. *Network Analysis*. Technical Publications, 2006.
- [32] E. I. Green. “The story of Q”. *American Scientist*, 43(4):584–594, 1955.
- [33] R. Collin and S. Rothschild. “Evaluation of antenna Q”. *IEEE Transactions on Antennas and Propagation*, 12(1):23–27, 1964.
- [34] C. Friedman. “Wide-band matching of a small disk-loaded monopole”. *IEEE Transactions on Antennas and Propagation*, 33(10):1142–1148, 1985.
- [35] F. B. Gross. *Frontiers in antennas: next generation design & engineering*. McGraw-Hill Education, 2011.
- [36] J. C. Maxwell. *A treatise on electricity and magnetism*, volume 1. Clarendon press, 1873.
- [37] P. Bevelacqua. “antenna theory”.

- [38] T. G. Tang *et al.* “Equivalent circuit of a dipole antenna using frequency-independent lumped elements”. *IEEE Transactions on Antennas and Propagation*, 41(1):100–103, 1993.
- [39] A. M. Niknejad. *Resonance and impedance matching*, page 168–200. Cambridge University Press, 2007.
- [40] G. Matthaei. “Microwave filters, impedance-matching networks and coupling structures”. *Artech House Book*, pages 1–15, 1980.
- [41] F. Miller *et al.* *Kirchhoff's Circuit Laws*. VDM Publishing, 2010.
- [42] C. Alexander and M. Sadiku. *Fundamentals of Electric Circuits*. 2003.
- [43] A. Yariv and J. E. Pearson. “Parametric processes”. *Progress in quantum electronics*, 1:2–49, 1969.
- [44] M. Liu *et al.* “Huygens' Metadevices for Parametric Waves”. *Physical Review X*, 8, 9 2018.
- [45] K. K. Chang and H. Hagger. “Parametric and Tunnel Diodes”. *Physics Today*, 18(1):71–75, 1965.
- [46] R. Cory and S. Solutions. “The nuts and bolts of tuning varactors”. *High Freq. Electron*, 8(2):42–51, 2009.
- [47] J. J. Carr. *Secrets of RF circuit design*. McGraw-Hill Education, 2001.
- [48] H. Wolff. “High-speed frequency-shift keying of LF and VLF radio circuits”. *IRE Transactions on Communications Systems*, 5(3):29–42, 1957.
- [49] J. Galejs. “Electronic broadbanding of high-Q tuned circuits or antennas”. *Arch. Elek. Übertragung*, 17(8):375–380, 1963.
- [50] F. Nogueira. “Bayesian Optimization: Open source constrained global optimization tool for Python”, 2014–.
- [51] R. E. Collin. *Foundations for microwave engineering*. John Wiley & Sons, 2007.

- [52] C. Hooge. “19.5 Capacitors and Dielectrics”. *BCIT Physics 0312 Textbook*, 2016.
- [53] *2018 International Conference on High Performance Computing Simulation, HPCS 2018, Orleans, France, July 16-20, 2018*. IEEE, 2018.
- [54] M. Manteghi. “An electrically small antenna concept design for transmitting a baseband signal”. In “2017 IEEE International Symposium on Antennas and Propagation & USNC/URSI National Radio Science Meeting”, pages 1481–1482. IEEE, 2017.
- [55] W. Yao and Y. Wang. “Direct antenna modulation-a promise for ultra-wideband (UWB) transmitting”. In “2004 IEEE MTT-S International Microwave Symposium Digest (IEEE Cat. No. 04CH37535)”, volume 2, pages 1273–1276. IEEE, 2004.
- [56] R. Zhu *et al.* “Frequency shift keying for direct antenna modulation (DAM) with electrically small antenna”. In “2017 IEEE International Symposium on Antennas and Propagation & USNC/URSI National Radio Science Meeting”, pages 1203–1204. IEEE, 2017.
- [57] S. D. Keller *et al.* “Electromagnetic modeling and simulation of a directly-modulated L-band microstrip patch antenna”. In “2007 IEEE Antennas and Propagation Society International Symposium”, pages 4489–4492. IEEE, 2007.
- [58] S. Almokdad *et al.* “Methodology for broadband matching of electrically small antenna using combined non-Foster and passive networks”. *Analog Integrated Circuits and Signal Processing*, 104(3):251–263, 2020.